



**APPLICATION OF FINITE ELEMENT TO EVALUATE MATERIAL WITH
SMALL MODULUS OF ELASTICITY**

THESIS

Boyce H. Dauby, Captain, USAF

AFIT-ENY-13-M-08

**DEPARTMENT OF THE AIR FORCE
AIR UNIVERSITY**

AIR FORCE INSTITUTE OF TECHNOLOGY

Wright-Patterson Air Force Base, Ohio

APPROVED FOR PUBLIC RELEASE; DISTRIBUTION UNLIMITED

The views expressed in this thesis are those of the author and do not reflect the official policy or position of the United States Air Force, Department of Defense, or the United States Government. This material is declared a work of the U.S. Government and is not subject to copyright protection in the United States.

AFIT-ENY-13-M-08

**APPLICATION OF FINITE ELEMENT TO EVALUATE MATERIAL WITH
SMALL MODULUS OF ELASTICITY**

THESIS

Presented to the Faculty

Department of Aeronautics and Astronautics

Graduate School of Engineering and Management

Air Force Institute of Technology

Air University

Air Education and Training Command

In Partial Fulfillment of the Requirements for the
Degree of Master of Science in Aeronautical Engineering

Boyce H. Dauby, BS

Captain, USAF

March 2013

APPROVED FOR PUBLIC RELEASE; DISTRIBUTION UNLIMITED

AFIT-ENY-13-M-08

**APPLICATION OF FINITE ELEMENT TO EVALUATE MATERIAL WITH
SMALL MODULUS OF ELASTICITY**

Boyce H. Dauby, BS

Captain, USAF

Approved:

Anthony Palazotto, PhD (Chairman)

Date

Marina Ruggles-Wrenn, PhD (Member)

Date

Lt Col Timothy Radsick, USAF (Member)

Date

Abstract

This thesis describes the development of a series of models utilizing the commercial finite element suite ABAQUS specifically to apply towards the study of biological tissue. The end goal is to be able to obtain the material properties of the *Manduca Sexta*, a biological inspiration for flapping wing micro-air vehicles.

Two finite element models were used to analyze the results of two prior studies of other researchers. A flat punch elastic model examined boundary effects and confirmed that the point of indentation was far enough removed from the boundary. The hyperelastic spherical indentation experiment examined the effects of coefficient of friction on the indentation. Another algorithm was reproduced to analyze the elastic, power law-hardening properties of a wide range of material properties.

A nanoindentation system was used to investigate the modulus of the *M. Sexta*. Due to instrument limitations, useful data was not able to be collected. An upper bound on the modulus was analytically established at approximately 3 MPa using the noise level of the equipment. A uniaxial tension test of the *M.Sexta* was used to obtain a reported initial modulus of elasticity values of 343 kPa.

Acknowledgments

I would like to express my sincere appreciation to my faculty advisor, Dr Anthony Palazotto, for his guidance and support throughout the course of this thesis effort. Much appreciation goes to Dr. Mark Willis and Jennifer Avondet at Case Western Reserve University for supplying many, many moths and Major Dave Sanders for assisting me in getting set up in the lab. I'd also like to thank Dr. Matthew Maschmann for his support using the nanoindenter and Dr. Heath Misak for his support using the microtensile machine. Lastly, I'd like to thank my coffee pot: the MVP of the Thesis Bowl.

Boyce H. Dauby

Table of Contents

	Page
Abstract.....	iv
List of Figures.....	viii
List of Tables	xiii
I. Introduction	1
1.1 Objective.....	1
1.2 Research focus.....	1
1.3 Methodology.....	2
1.4 Literature Review	3
1.5 Research Implications	19
1.6 Thesis Preview.....	20
II. Theory	21
2.1 Chapter Overview.....	21
2.2 FE Models Material Theory	22
2.3 Muscle Structure and Tensile Tests Theory	33
2.4 Summary.....	35
III. Finite Element Model Development.....	36
3.1 Chapter Overview.....	36
3.2 Finite Element Overview.....	36
3.3 Analysis Considerations	36
3.4 Models.....	37
3.7 Summary.....	42
IV. Experimentation Methodology	43
4.1 Chapter Overview.....	43

4.2 Nanoindentation Experimentation.....	43
4.3 Uniaxial Tensile Experimentation.....	48
V. Analysis and Results	51
5.1 Chapter Overview.....	51
5.3 Results of Finite Element Simulations	51
5.4 Results of Nanoindenter Experiment.....	73
5.5 Results of Tensile Experiment.....	77
5.6 Summary.....	84
VI. Conclusions and Recommendations	85
6.1 Chapter Overview.....	85
6.2 Conclusions of Research	85
6.3 Recommendations for Future Research.....	86
6.4 Summary.....	87
Appendix A: Finite Element ABAQUS Input Files	89
Appendix B: MATLAB Codes	98
Appendix C: Hawkmoth Rearing [21].....	105

List of Figures

	Page
Figure 1: (a) Simple Diagram of Indentation (b) Example Load-Displacement Plot for a Standard Instrumented Indentation.....	3
Figure 2: Cartoon Schematic of Common Indenter Geometries, (a) Cylindrical (b) Spherical, Indenting a Flat Half-space	5
Figure 3: Representative Location of 2 Points Required for the Elastic-Plastic Spherical Model Shown on a Generic Loading and Unloading Diagram.....	6
Figure 4: Experimental Setup for Porcine Sclera Indentation Experiment From Nayer <i>et al.</i> [13].....	10
Figure 5: Muscle 3D-reconstruction and mesh. (A) Example of a 3D reconstruction. (B) Its associated finite-element model. (C) Superposition of the 3D reconstruction and the finite- element model.	11
Figure 6: Rat Muscle Sample with Sandpaper Grips from Calvo, <i>et al.</i>	12
Figure 7: A Natural Flapping-wing MAV, <i>Manduca Sexta</i>	14
Figure 8: Cross-sectional diagram of thorax highlighting the various muscle groups in the Hawkmoth and the interaction with Exoskeleton	15
Figure 9: 3D Diagram of Thorax and Flight Muscles.....	16
Figure 10: Diagram of Flight Mechanics of Hawkmoth: (A) DVM Contraction/Upstroke; (B) DLM Contraction/Downstroke [23]	17
Figure 11: Diagram of the basic functional unit of Muscle Tissue (Sarcomere) made up of Interlocking Actin and Myosin Filaments.....	18

Figure 12: Side View Schematic (Left) and CT scan (Right) of <i>M. Sexta</i> Primary Flight Muscles	19
Figure 13: Elastic Spherical Indentation.....	24
Figure 14: Cylindrical Flat Punch Indentation.....	25
Figure 15: Elastic-plastic Power- Hardening Stress Strain Curve	28
Figure 16: Standard Indentation Curve.....	29
Figure 17: Geometry of a common Indenter head: Berkovich Pyramid.....	30
Figure 18: Force-Length Example Diagram for Muscles showing the Total force-length response is a sum of the Active and Passive Properties of the muscle	34
Figure 19: Model Boundary Conditions: Y-axis Symmetry (Left side) and Fixed (Bottom).....	38
Figure 20: Diagram of simplification made by assuming no variation in the angular direction for the CAX4R and CAX4RH elements.....	39
Figure 21: ABAQUS Axisymmetric Model of Cylindrical Flat Punch indenting a sample with partition lines to divide sample in order to refine the mesh. Inset: axisymmetric assumption diagram	40
Figure 22: ABAQUS Axisymmetric Model of Sphere indenting a sample with partition lines to divide sample in order to refine the mesh. Inset: axisymmetric assumption diagram.....	41
Figure 23: Close up View of 3D revolution of Axisymmetric Models:	41
Figure 24: Example mesh of a sample as a whole (left) and close up showing the refined area underneath the indenter (right)	42

Figure 25: Sample Puck for indentation experiment with rubber ring attached to glass slide to hold saline solution.....	44
Figure 26: Partially Dissected Moth highlighting the point of incision of the exoskeleton (wings are removed).....	45
Figure 27: Isolated Individual muscle units of the Hawkmoth DLMs	46
Figure 28: (left) Cartoon showing sample/adhesive interaction and (right) muscle sample in solution adhered to slide with glass block flush with its right edge.	47
Figure 29: (a) Agilent G200 Nanoindenter (b) Sample Puck in Test Rack of Indenter ...	47
Figure 30: Agilent T150 UTM and Specifications	49
Figure 31: Template card technique showing Sample in Testing Machine. Edges of card have been cut, allowing the sample to be stretched.	50
Figure 32: Spherical Elastic Maximum Indentation, 2D (left) and 3D (right). Colors indicate stress in the vertical direction (MPa).....	53
Figure 33: Mesh Resolution Comparison, F-d Elastic Spherical.....	53
Figure 34: Mesh Resolution Comparison, F-d Elastic Spherical.....	54
Figure 35: Spherical Plastic Maximum Indentation, 2D (left) and 3D (right).....	55
Figure 36: Spherical Plastic Residual Indentation, 2D (left) and 3D (right)	55
Figure 37: Force Displacement Curve for Forward Analysis (R=788 μ m).....	56
Figure 38: Flow Chart for Determining Material Properties	57
Figure 39: Comparison of Force Indentation for Forward and Reverse Analysis	58
Figure 40: Mesh Refinement for Flat Punch using Force-Displacement Relation.....	61
Figure 41: Mesh Refinement for Flat Punch using Stress-Radius Relation	61

Figure 42: Model Boundary Conditions: Y-axis Symmetry (Left side, Right side) and Fixed (bottom).....	62
Figure 43: Comparison of the stress along the bottom of a flat punch indenting several sample sizes.....	63
Figure 44: Comparison of the force-displacement relationship for a flat punch indenting several sample sizes with varying horizontal distance (W)	64
Figure 45: Comparison of the stress along the bottom of a flat punch indenting several sample sizes.....	64
Figure 46: Comparison of the force-displacement relationship for a flat punch indenting several sample sizes with varying vertical distance (L).....	65
Figure 47: Stress Field for Hyperelastic Material.....	67
Figure 48: Friction Comparison Force Indentation Curve ($h=1\mu\text{m}$)	68
Figure 49: Friction Comparison Contact Radius ($h=1\mu\text{m}$).....	69
Figure 50: Friction Comparison Force Indentation ($h=4\mu\text{m}$).....	70
Figure 51: Friction Comparison Contact Radius ($h=4\mu\text{m}$).....	70
Figure 52: Representative stress and strain from a spherical indenter into a hyperelastic medium simulation compared against an elastic medium.....	71
Figure 53: Representative stress and strain from a spherical indenter into a hyperelastic medium simulation with a curve fit to extract Ogden parameters	72
Figure 54; Comparison of the simulation results from initial material parameters and material parameters from a curve fit	73
Figure 55: Noise from Load vs Displacement Channel for G200 during Surface Find ...	74

Figure 56: Load/Displacement Slope vs. Elastic Modulus for Varied Indenter Radius with noise level shown as black horizontal line..... 75

Figure 57: Force-displacement relationship for spherical indenting a hyperelastic medium with 1st order Ogden potential parameters $\mu_0=7.97\text{kPa}$ and $\alpha=20$ 76

Figure 58: Stress-Strain Diagram for all 4 tests of Hawkmoth DLM motor unit and their individual linear regression fits and the overall regression fit. 78

Figure 59: Hawkmoth DLM Stress-strain curve with Outlier Removed..... 79

Figure 60: Chart of desiccation of Hawkmoth muscle over time while exposed to air.... 81

Figure 61: Boundary Conditions (left) and Mesh (right) for Uniaxial Tension Model (2mm gauge length shown)..... 83

Figure 62: Stress cross sections for all tests to 50% strain. (Clockwise from bottom left: 2mm gauge length, 4 mm gauge length, 7 mm gauge length, and 10 mm gauge length.) 84

Figure 63: Typical *M. sexta* pupa and diagram of individual parts..... 105

Figure 64: Two freshly-enclosed *M. sexta* specimens. One is only 10 minutes old and has not inflated its wings. 106

Figure 65: Enclosure for the pupae: (Left) Closed box creates day/night conditions with a timer controlling the LED lights, shown in part (Right)..... 107

List of Tables

	Page
Table 1: Measured Values from Force Indentation Curve.....	56
Table 2: Input Values to Zhao Algorithm.....	56
Table 3: Zhao Algorithm Output Comparison with Symbolic Solver.....	58
Table 4: Zhao Algorithm Output Comparison with Numerical Solver	59
Table 5: Summary of effects of E from the smallest sample boundary length compared to Hertzian analytic solution and a large sample.....	66
Table 6: Results for 4 Tests of Initial Modulus Elastic for Hawkmoth Muscle	77
Table 7: Summary Statistics of the 4 Uniaxial Tension Tests	79
Table 8: Summary Comparison with prior Muscle Tensile Experiments.....	82

APPLICATION OF FINITE ELEMENT TO EVALUATE MATERIAL WITH SMALL MODULUS OF ELASTICITY

I. Introduction

1.1 Objective

This study describe a series of models utilizing the commercial finite element suite ABAQUS which allow hyperelastic materials to be considered for an application towards soft biological tissue. Specifically, this present study attempts to apply the models developed within this study to evaluate the material properties of the muscles of the *Manduca Sexta*. This insect, known as the hawkmoth, is of interest for study as a biological inspiration for flapping wing micro-air vehicles [1]. Attempts to model the entire moth have been made by Demasi [2]; however, deficiencies remain in the accuracy of the input material to that model. The present study attempted to correct that deficiency through finite element modeling and experimentation with nanoindentation, along with a uniaxial tensile test. As part of the study, the structure of the muscle and information on the mechanics of insect flight are discussed. Also, to ensure full understanding of the process on nanoindentation, models using standard engineering materials such as aluminum are examined as these materials have better-characterized properties than hyperelastic materials.

1.2 Research focus

Nanoindentation is a technique that can be used to analyze problems on a small length scale problems. It is a popular method for evaluating the mechanical properties of materials and structures, including elastic modulus, yield strength, hardening coefficient,

residual stress, fracture toughness, and viscoelastic behavior. In addition to its usefulness in examining problems on a small length scale, the preparation required for these tests can be less intensive than traditional tests, such as uniaxial or biaxial tests.

Typically, commercial indenters are set up as “black-box” instruments that automatically calculate the elastic-plastic properties of the material. However, many materials do not conform to the elastic-plastic theories and additional analysis of the force-indentation data is required. Finite element (FE) modeling can aid in this additional analysis by correlating the shape of the indentation curve with the desired properties.

The hawkmoth muscles, called the dorsal longitudinal muscles (DLMs) and dorsal ventral muscles (DVMs), can be described as behaving as an orthotropic, viscoelastic material. Spherical indentation experiments (utilizing the developed finite element model) were attempted to examine the transverse elastic properties and the finite element models were used to show why they failed. Uniaxial tension tests were used to attempt to obtain the longitudinal properties of the specimen.

1.3 Methodology

All finite element modeling was accomplished using the ABAQUS finite element program from Dassault Systems. FE models were developed then validated with experimental data and closed form analytic solutions, when available. Experiments involving nanoindentation were attempted using the MTS Nanoindenter XP. This equipment was used with the permission of the Air Force Research Laboratories (AFRL) Materials and Manufacturing Directorate. All uniaxial tensile tests were performed using the MTS Nano Universal Testing Machine. Moth specimens used to obtain the muscle

samples were provided by Case Western University. More information on the equipment used in this study and instructions for raising the moths can be found in the Appendix.

1.4 Literature Review

1.4.1 Indentation Testing Introduction

In this section, a brief overview of nanoindentation is given to introduce what it is and what a typical experiment involves.

In nanoindentation testing, a probe is pressed into a material surface under either load- or displacement-control. The load and displacement data can be used to determine various material properties of the sample. Useful results from nanoindentation experiments require measurement of extremely small forces and displacements with great accuracy and sensitivity. A simple indentation diagram (a) and a typical load-displacement curve (b) can be seen in Figure 1.

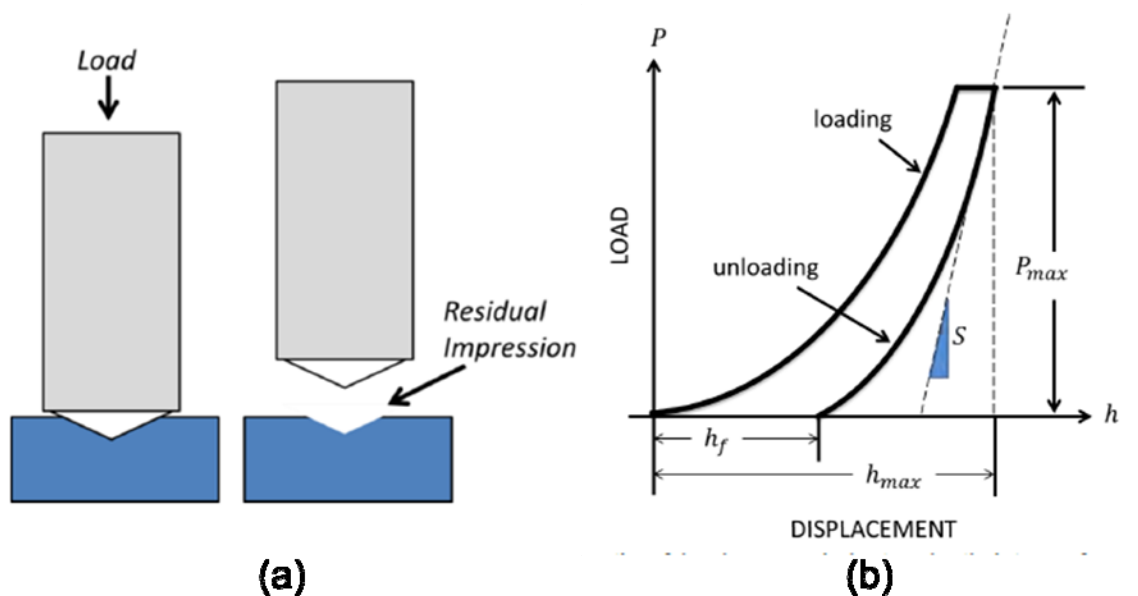


Figure 1: (a) Simple Diagram of Indentation (b) Example Load-Displacement Plot for a Standard Instrumented Indentation

Oliver and Pharr pioneered the effective use of a small-scale version of the standard indentation test for an elastic-plastic material [3]. Nanoindentation had been around for a decade at that point, but the results had not been as precise or repeatable as other, more established methods for testing material properties. One of the most significant contributions of their work was the realization that the unloading curve of the load-displacement plot was not linear, as had previously been assumed. The mathematical relationships used to determine the properties are discussed in depth in Chapter 2.

As mentioned, two types of indenters were examined in this study: cylindrical and spherical (Figure 2). The geometry of the probe is important because the shape determines the deformation profiles obtained during the test. The cylindrical, flat-tips are convenient because they have a constant contact area with the sample. This simplifies much of the analysis, however, for small-scale tests it can be difficult to align the probe surface with the surface of the sample. Spherical tips are advantageous in that they delay the immediate onset of plastic deformation. This is one of the reasons this indenter tip is popular with evaluation of biological tissues.

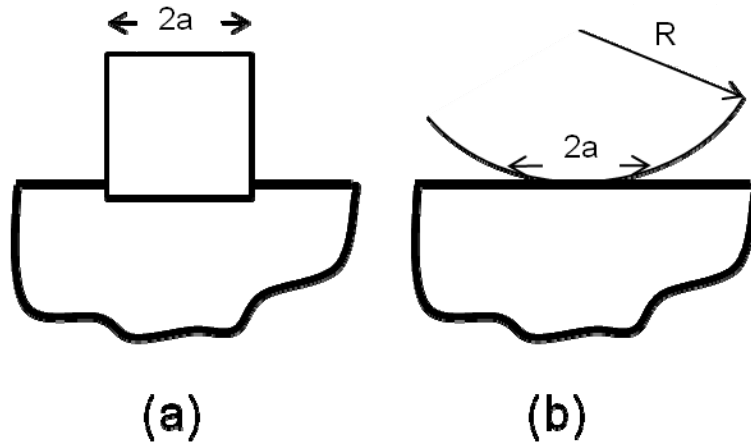


Figure 2: Cartoon Schematic of Common Indenter Geometries, (a) Cylindrical (b) Spherical, Indenting a Flat Half-space

1.4.2 Elastic-Plastic Spherical Finite Element Model

A single sharp indentation cannot yield a unique solution [4] through the standard indentation technique. For a power-law hardening material with properties σ_y (yield strength), E , ν , and n (work-hardening coefficient), only 2 of the properties can be determined while the other 2 have to be known *a priori*. However, researchers have been able to take advantage of a concept called representative strain to simplify the problem using finite element analysis. [5] Zhao, *et al.* used spherical indentation along with representative strain to determine the unique properties from one indentation. From that one indentation they selected two points on the force-displacement loading curve and the contact stiffness (slope of the unloading curve) to produce 3 equations to be able to solve for σ_y , E , and n (ν was found to vary little for the analysis and was assumed to be 0.3).

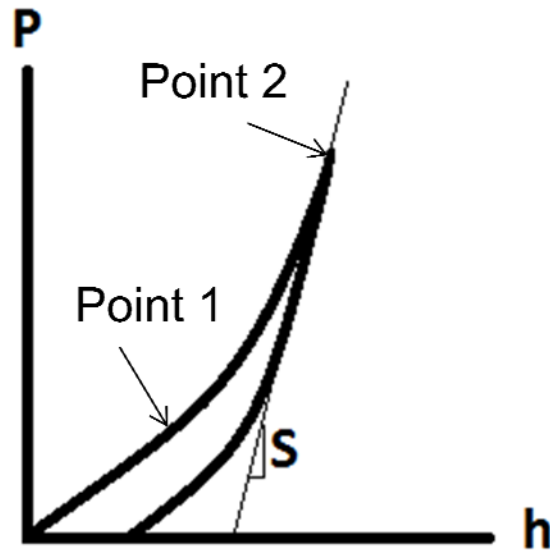


Figure 3: Representative Location of 2 Points Required for the Elastic-Plastic Spherical Model Shown on a Generic Loading and Unloading Diagram

The goal of this study was to utilize the algorithm developed by Zhao for a wide range of materials. Possible applications to the exoskeleton of the hawkmoth are examined. The formulation of these equations is discussed in Chapter 2 and the finite element model is reproduced in Chapter 3.

1.4.3 Biomechanics Introduction

Experiments to determine the material properties of muscles and other soft tissues have been documented for centuries. Many of the famous physical relationships that are used in engineering today had their origins in scientists investigating biomechanics. Leonhard Euler was the first to examine propagation of pulse waves in arteries. Thomas Young (of Young's Modulus fame) studied the formation of human voice and connected it with the elasticity of the vocal cords. Poiseuille studied the pressure in the aortas of dogs which led to the establishment of the no-slip condition in pipe flow. [6]

The determination of mechanical properties of soft tissues in biomechanics is often challenging. Isolating the tissue from the subject for testing is often very difficult. The small size of the samples and the need to maintain hydration and in normal living conditions can cause complications as well. In addition, biological tissues are often nonlinear and dependent on the history of the loading and unloading cycle. More of these characteristics are discussed in Chapter 2.

Uniaxial, along with biaxial (longitudinal and transverse direction), tension tests are some of the more common methods to characterize the properties of soft tissues. The tension test is often used as baseline from which other experiments branch off. Early experiments by Wertheim (1847) showed the elastic nature of soft tissue. Hill (1938) applied data from uniaxial tests for his first models of the contraction of muscles [5]. Other tests of note: Moss and Halpern (1977) [7] determined the viscous and elastic properties of resting frog muscle; Van Locke *et al.*, (2006) [8] examined the compressive behavior of muscle; and Lally *et al.*, (2004) [9] studied the effects of biaxial and uniaxial tension on pig artery

The popularity of indentation tests for biological materials has grown quickly in the last decade as the machinery and techniques required for the tests has advanced. In the following few sections, several different indentation and uniaxial experiments with soft tissues are reviewed. The techniques used in these examples were the basis for the finite element models and the attempted experiments in this present study are described in more detail in Chapters 2 and 3.

1.4.4 Soft Tissue Indentation FE and Experimentation

Conducting a nanoindentation experiment with a biological tissue sample is a very challenging task. There are many factors that can influence the experiment. The factors influencing sample preparation and tip preparation described in this section are selected from the *Handbook of Nanoindentation with Biological Applications* [10], [11].

One of the most influential factors in indenting biological tissue is maintaining its hydration. Soft tissues are made up of mainly water and exposure to air results in tissue desiccation. This desiccation can change the material properties of the sample.

Biological tissue samples also have a surface roughness that would otherwise be removed through a polishing process for indentation of a standard engineering material. This technique is not available when testing soft tissues as their microstructures could be substantially disrupted. This roughness influences the tip selection. The low modulus of the tissue normally requires the use of cylindrical flat punch or spherical tips. However, the spherical tip allows for some inaccuracy in the approach to the sample and is therefore often used for testing soft tissues with irregular surfaces.

Also, many soft tissues are not isotropic. The anisotropic nature doesn't meet many of the assumptions for standard indentation theory. Since the muscle sample has properties that are transversely orthotropic, the results of this test would produce an indentation elastic modulus that is a function of the transverse and longitudinal moduli, weighted in the direction of the indentation, the transverse direction. The materials also have large displacements for a given load due to their hyperelastic nature.

Instrumentation also presents limitations on testing soft tissues. Most commercial instrumented nanoindentation devices are calibrated for testing materials with a modulus

in the GPa or MPa range. Most biological soft materials have elastic moduli in the range of tens to hundreds of kPa's and can present problems with finding the surface of the material. As is discussed in Chapter 5, the resolution of the chosen instrumentation proved to be the source of the difficulty in completing this experiment.

To aid in the development of the procedures for the experiment, several previously-conducted experiments and their associated finite element models (if used) were examined. The first indentation test described in this section comes from a group at the National Institute of Health who investigated the spherical indentation of soft matter in the hyperelastic regime. [12] Researchers conducting spherical nanoindentation experiments for Hookean elastic materials compare their results to the classical Hertz solution for a sphere impacting a flat plane. This study focuses on developing a relationship for hyperelastic materials through finite element modeling with several different hyperelastic strain energy potential functions. Lin, *et al.* compared the resulting functions to synthetic gels and mouse cartilage. The mouse cartilage test yielded a shear modulus of 14.3 kPa (μ) and a fitting parameter (α) of 7.3. The derivations of Hertzian contact and the hyperelastic relations are discussed in Chapter 2. The hyperelastic finite element model used in this study was based on the Lin paper.

Another indentation test that was examined was one by V.T. Nayar *et al.* [13] and examined porcine sclera (the white of the pig's eye). The results from this study are not useful for comparison to the muscles of the hawkmoth as the sclera has a planar isotropic structure. However, the methods used in this study were helpful. The sclera (approximately 1–1.2 mm thick) was removed from the pig in approximately 1 cm squares and secured to a glass slide with cyanoacrylate (superglue). A shallow well was

built up around the outside of the sample to form a ring. This ring (shown in Figure 4) was then filled with saline solution to maintain hydration of the sample. Testing was accomplished with an 80 μm cylindrical punch. Load controlled indentations were conducted to 375, 750, and 1500 μN . Shear modulus reported was approximately 30 kPa.

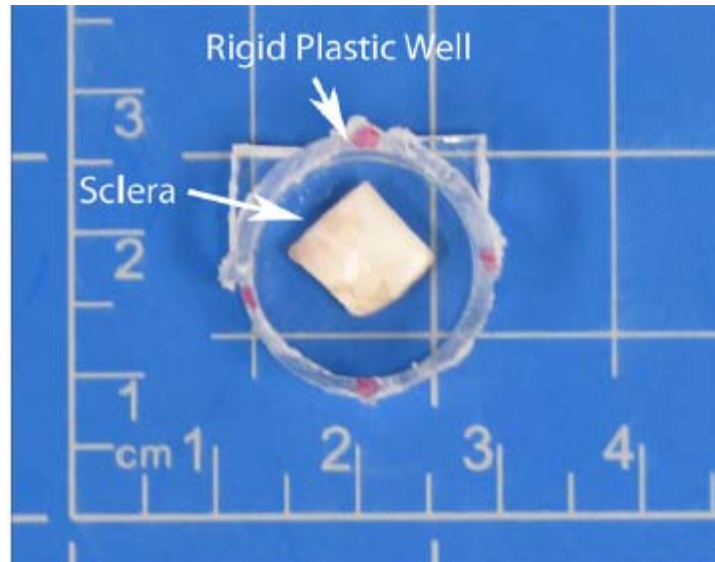


Figure 4: Experimental Setup for Porcine Sclera Indentation Experiment From Nayer *et al.* [13]

A third indentation test was accomplished with the skinned cardiac muscle fibers of a cow. The cardiac muscles were isolated from the adult cow, rinsed thoroughly, and secured in a mica sheet. This experiment used atomic force microscopy (AFM) so the experimental protocols would not be comparable. Their results from this technique were on the order of 20 kPa for the shear modulus. [14]

1.4.5 Soft Tissue Uniaxial Experimentation

The first uniaxial tension study discussed in depth here from Laure-Lise Gras, *et al.* [16], examined the passive response of human sternocleidomastoideus muscle (located in the neck) to tension. Their study was performed *in vitro* therefore the muscle samples were removed from cadavers and placed into a uniaxial testing machine. Boundary conditions were maintained by removing portions of the jaw and allowing the entire muscle to be tested. Typical specimens were 134 mm long with a cross-sectional area of 300 mm². 3D reconstructions can be seen in Figure 5.

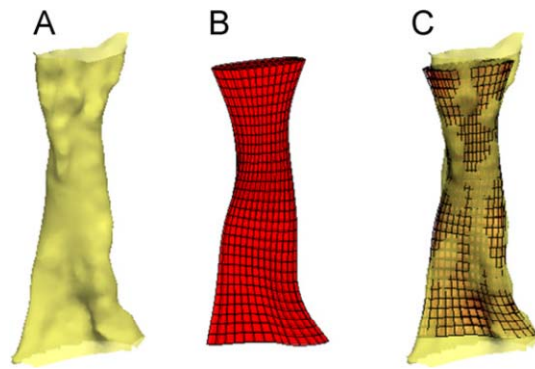


Figure 5: Muscle 3D-reconstruction and mesh. (A) Example of a 3D reconstruction. (B) Its associated finite-element model. (C) Superposition of the 3D reconstruction and the finite- element model.

In order to prevent the specimen from desiccating, Laure-Lise Gras, *et al.* would moisten the surface of the muscles regularly with a saline solution. After preconditioning, the specimens were subjected to a maximum deformation of 15% at a strain rate of 0.00125s⁻¹. After assuming an incompressible ($\nu = 0.5$) and isochoric material, results were fitted to an exponential hyperelastic form from Stern-Knudsen and also to the Ogden hyperelastic constitutive law. These results were compared to finite

element models obtained by iterating the parameters of the function. For their results, they were able to obtain a value for shear modulus of 37 kPa.

Another uniaxial tension test was accomplished by Calvo, *et al.* [17] only their specimen of interest was rat muscle (Figure 6). The tendons of the rat were also examined by Calvo, *et al.* but this is not discussed here. The samples studied by Calvo, *et al.* were much closer to the size of the muscle samples of the hawkmoth. Specimens averaged a length of 6.6 mm and a cross sectional area of 1.8 mm². The samples were glued to pieces of sandpaper to be placed into the grips of a displacement controlled microtester. A testing velocity of $0.2 \cdot L / 100 \text{ mm min}^{-1}$ was used, which for the average muscle length corresponded to $3.3 \cdot 10^{-5} \text{ s}^{-1}$ strain rate, which is slower than the previous study. Sample hydration was maintained through a cooled ultrasonic humidifier. The Calvo study used a modified form of the Weiss strain-energy density function to fit the experimental data. Again, isochoric and incompressible assumptions were made. One thing that stands out in their test is that they make no mention of preconditioning the sample prior to testing. This differs from standard practice outlined and could be a source of variability in their data due to viscoelastic effects. [5]

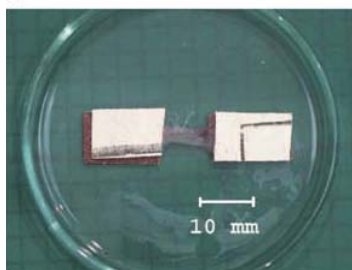


Figure 6: Rat Muscle Sample with Sandpaper Grips from Calvo, *et al.*

A third uniaxial tensile actually uses *M. Sexta* as a subject, only with a very important distinction. The group from Tufts University [18] studied the muscle of the species when it was in its caterpillar state prior to its metamorphosis. An initial thought would be that a direct comparison could be made between this muscle and the muscle of the flying insect. However, these muscles are used for entirely different tasks. The muscle of the caterpillar undergoes strains of 30% in approximately 1 second. This differs greatly from that on the moth where strains of 7% in around 0.018 s are the norm. The techniques used in the Tufts study, however, are useful for application to the current study. Both passive and active muscles were studied which provides a useful comparison between the two states.

Muscle samples from the caterpillars in the Tufts study were approximately 4-5 mm long. Cross sectional area was not reported. Muscles were pinned by the attached cuticle at each end in a horizontal bath of saline to prevent dehydration. One end of the muscle was secured by a hook to a displacement controlled testing machine. The samples were preconditioned for between 6-10 cycles to remove the hysteresis. The Dorfman model applied a modified pseudo-elastic model from Dorfmann and Ogden (2003). Shear modulus reported in the 0.78 kPa range was much lower than the other experiments.

1.4.6 Biological Specimen

In order to understand the reason for investigating the hawkmoth muscle, it is useful to know more about the species and how the muscles induce flight. This is described in this section.

The biological species chosen to be studied for the experimentation portion of this study is the *Manduca Sexta*. The species, which will be referred to as the hawkmoth for the remainder of the study, is shown in Figure 7. The size, weight, and flight performance characteristics of the hawkmoth made it an ideal candidate of study as a natural MAV. The hawkmoth weighs approximately 1.5 to 2 g and has a wingspan between 9.5 and 12 cm. [19] As such, it is one of the larger flying insects in nature.

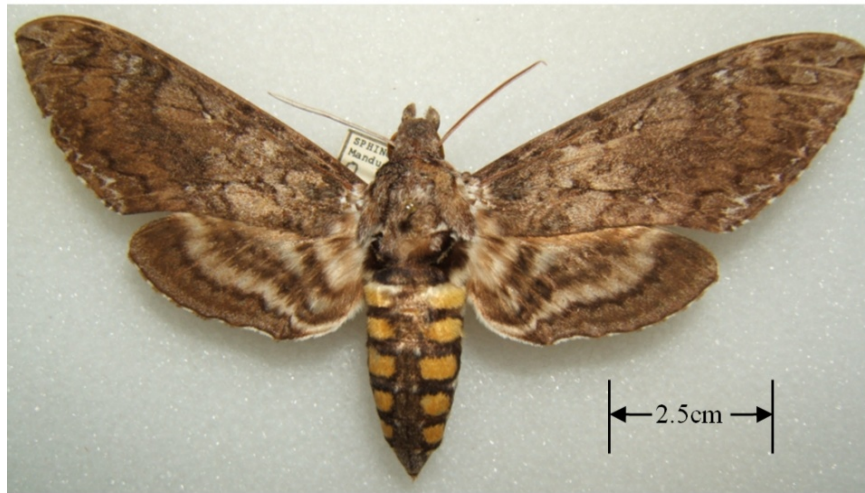


Figure 7: A Natural Flapping-wing MAV, *Manduca Sexta*

The hawkmoth anatomy can be divided into 4 main parts: head, wings, thorax and abdomen. The head contains the primary nervous system control organ, two eyes and antennae, and a coiled proboscis for feeding on plant nectar. The abdomen contains many of the body's organs for digestion and reproduction. [20] Two sets of wings, the forewings (larger and towards head) and hind wings (smaller and closer to abdomen), consist of a thin, flexible membrane overlaying a network of rigid veins. The wing's membrane is covered with scales that are used for camouflage and possibly influence flow patterns during flapping [20]. The thorax is located at the intersection of the other

main parts and contains the mechanism to generate and control flight. A cross-sectional diagram of the thorax can be seen in Figure 8. Within the exoskeleton of the thorax are the DVMs and DLMs as well as a bundle of nerves called the ganglia that act as a secondary brain to control the movement of the muscles. On top of the thorax is a much thicker and more rigid section called the tergal plate. The interaction of the tergal plate and the flight muscles results in the wings flapping as is shown in the next section. A simplified, 3-dimensional diagram of the thorax and the flight muscles can be seen in Figure 9.

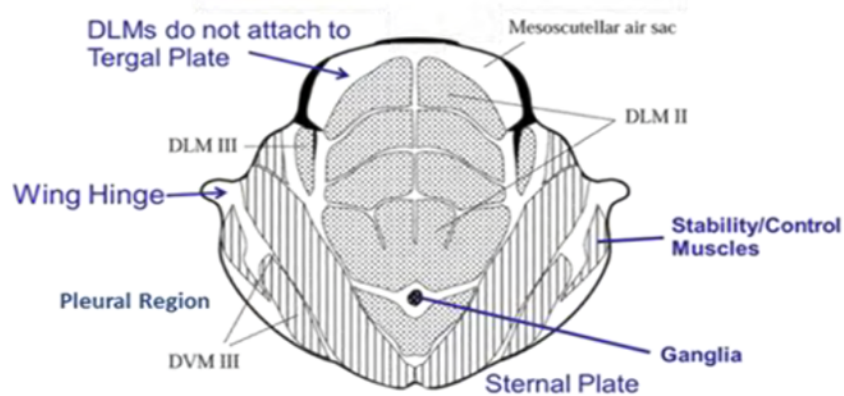


Figure 8: Cross-sectional diagram of thorax highlighting the various muscle groups in the Hawkmoth and the interaction with Exoskeleton

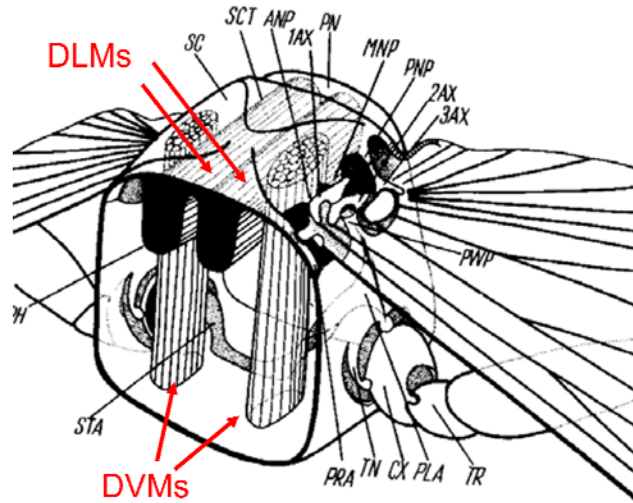


Figure 9: 3D Diagram of Thorax and Flight Muscles

The hawkmoth is known for its impressive ability to hover. Its rapid wingbeat has often led to it being misidentified as a hummingbird. The hawkmoth accomplishes its hover through what is known as synchronous, indirect flight. During synchronous flight, for every pulse from a neuron there is a contraction of the muscles and one corresponding flapping motion of the wings. Asynchronous flight differs from synchronous flight in that one neuron pulse will cause multiple contractions of the muscles which will produce multiple cycles of flapping. Synchronous flight is common in insects with flapping frequency below 100 Hz. An indirect flapping mechanism is one in which the muscles do not directly attach to the wings. They pull on the exoskeleton which then translates that motion into flapping via a hinge. Direct flight is produced by the flight muscles attaching directly to the wing.

The indirect flight of the hawkmoth begins with the DVMs. The DVMs (shown in Figure 10 in the brown) are oriented vertically and at an angle. These muscles contract and compress the exoskeleton. The compression causes the inner portion of the wing

hinge to drop and the wing to rise. To produce the downstroke, the DLMs (shown in pink) contract and cause the exoskeleton to bow upward. The bowed exoskeleton raises the hinge and lowers the wings. The DLMs are the much larger, and therefore more powerful, of the two sets. The DLMs relatively powerful downstroke produces the majority of the lift. It has been shown in several studies of the moth that both the upstroke and downstroke will produce lift via changing the camber of the wing. The change in camber is passive; the moth does not directly control it. A typical hawkmoth will flap its wings at a frequency around 20 or 25 Hz.

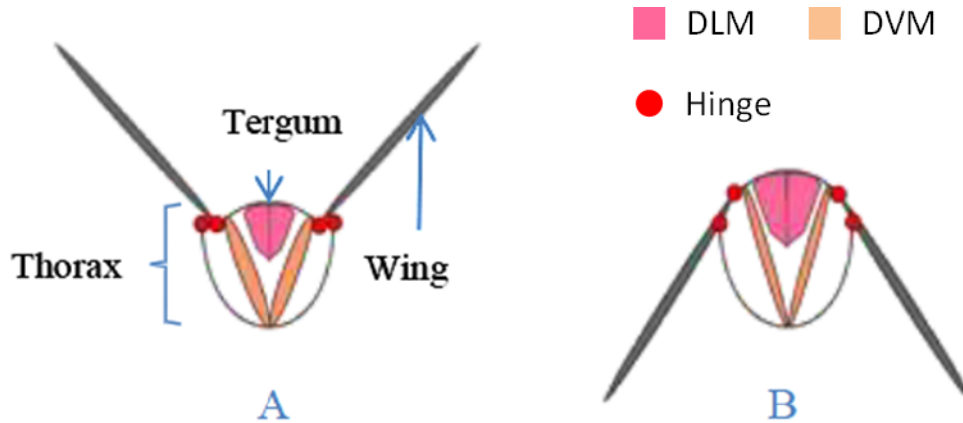


Figure 10: Diagram of Flight Mechanics of Hawkmoth: (A) DVM Contraction/Upstroke; (B) DLM Contraction/Downstroke [23]

The most basic contractile unit of the muscle is the sarcomere. The sarcomere is a region of interaction of two myofilaments, one thick and one thin. The thick filaments are myosin molecules, while the thin ones are actin molecules. (Diagram shown in Figure 11) The sarcomere is approximately $2.5 \mu\text{m}$ long, with the exact length dependent on the force acting in the muscle and the state of excitation. [6] When the muscle receives a signal from the motoneuron, the molecules attached to the myosin filaments extend out,

pulling on the actin filaments. This causes the two filaments to slide past each other and contract the muscle. Neither the myosin or actin filament shortens during the contraction.

[6]

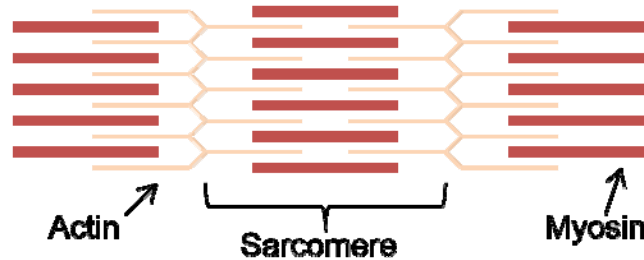


Figure 11: Diagram of the basic functional unit of Muscle Tissue (Sarcomere) made up of Interlocking Actin and Myosin Filaments.

The rest of the structural arrangement on the muscle can be analogous to a Russian nesting doll. The myofilaments are bound into groups of called muscle fibrils. Muscle fibers contain groups of these fibrils. All of the muscle fibers that are innervated from a single motoneuron are called muscle motor units. The complete muscle (the outermost doll) is made up of all the motor units. As mentioned earlier, in the hawkmoth there are two sets of flight muscles: the DVMs and DLMs. Each DLM is composed of 5 motor units, numbered 1 through five on the right hand side of Figure 12. The DVMs contain 6 motor units each; however, they are less massive than the powerful DLMs.

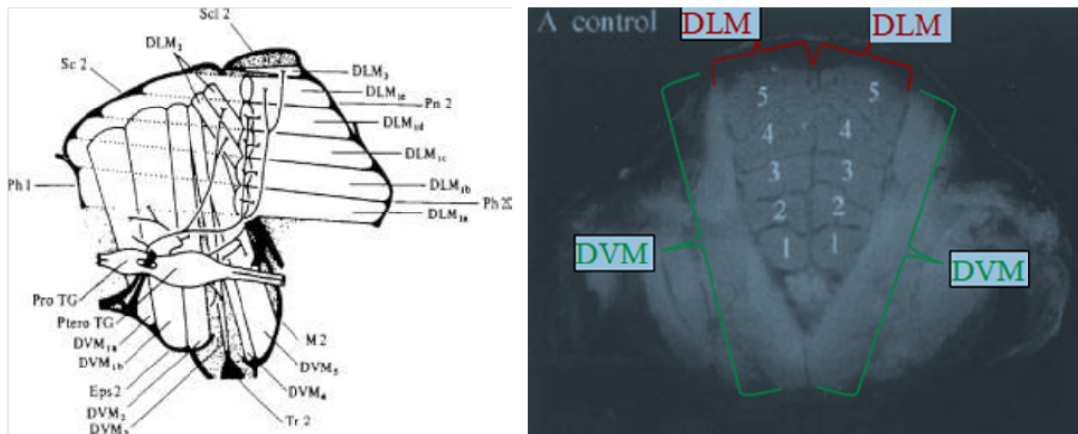


Figure 12: Side View Schematic (Left) and CT scan (Right) of *M. Sexta* Primary Flight Muscles

Other members of the research team here at AFIT have analyzed different aspects of this species physiology to investigate these flight mechanics. Most recently Major Ryan O’Hara researched the material properties and structural dynamics of the forewing. [20] Lt Alex Hollenbeck [21] and Brian Cranston [22] investigated the exoskeleton of the thorax material properties and how compression in the vertical and longitudinal directions affected the flapping motion of the wings and related it to power output from the muscles. Also, Captain Travis Tubbs explored the timing of the muscle neurons through electromyography. [23] This study is the first here at AFIT to attempt to directly look at the material properties of the muscles.

1.5 Research Implications

The finite element models developed during this study are valuable to other researchers here at AFIT. The finite element models have been validated using experimental data and analytic equations so there will be considerable time savings for another student and aid them in their research.

One possible application of the insight gained from the experimental portion of this study could be to develop artificial muscles that could power an artificial flapping-wing MAV. Muscles have been used for inspiration in design since the 1950s and 60s. The McKibben pneumatic artificial muscles, developed by the Bridgestone Rubber Company of Japan, were an early example. [24] These devices pumped pressurized air into a rubber bladders enclosed in a mesh shell to mimic a muscle contraction. These devices produced narrower dynamic range, but higher force intensity than natural muscles. Applications for MAV development would not be very practical due to the size and power constraints of the devices.

More recently, new electroactive polymers (EAPs) have been developed that have the properties required to simulate the contraction of muscles [25], [26]. EAPs are materials which can change shape in response to an electrical stimulus. Since the 1990s, the strains capable of being produced by these materials have increased thereby expanding their usefulness. Two of the latest advances in EAP technology within the last year involve carbon nanotube aerogels [27] and telescopic polymer chains [28].

1.6 Thesis Preview

In Chapter 2, the theory behind nanoindentation is outlined. The analytic solutions for indentations into an elastic material are outlined. These equations are used to compare against the finite element models in Chapter 3. Additionally the constitutive equations for the elastic, hyperelastic, and elastic-plastic material properties are described as well as the material structure of the hawkmoth muscle.

In Chapter 3, the development of the finite element models is described. The boundary conditions, element types, and the model type are discussed for each of the 2 types of indenters (spherical and cylindrical flat punch).

In Chapter, 4 the hawkmoth muscle experimentation methodology is discussed for the nanoindenter and the uniaxial tensile experimentation. The process of dissection for the moths is also outlined.

In Chapter 5, the 3 models are used in scenarios with applications to testing biological tissues. Additionally, problems with the nanoindentation experiment are attempted to be explained. Lastly, the uniaxial tension test results is reported and discussed. Chapter 6 summarizes the results of this study and gives recommendations for future research.

II. Theory

2.1 Chapter Overview

The purpose of this Chapter is to outline the analytic solutions of the interaction between the indenter geometry and the materials in the models developed. These theories are the foundation for the models of nanoindentation developed in Chapter 3. The first section describes a fully elastic material indented by a probe with 2 different shapes (spherical and cylindrical flat punch). In the second section, the elastic material model material properties of the sample are changed to a hyperelastic material. This indenter model is compared to equations derived from Lin *et al* [12]. The third and fourth sections are models of indentation into elastic-plastic materials by a sharp and spherical

indenter, respectively. The spherical indenter model was developed to obtain the entire stress-strain curve from a single indentation.

Additionally, as mentioned in the objective, an overview of the muscle material of the hawkmoth is laid out. That final section outlines the models of the tissue structure. The equations used in a uniaxial tensile test are also described.

2.2 FE Models Material Theory

2.2.1 Elastic Indentation Theory

The first finite element model described in this research study is a linear elastic, isotropic material that behaves according to the following:

$$(2.1) \quad \begin{bmatrix} \varepsilon_{11} \\ \varepsilon_{22} \\ \varepsilon_{33} \\ 2\varepsilon_{23} \\ 2\varepsilon_{13} \\ 2\varepsilon_{12} \end{bmatrix} = \frac{1}{E} \begin{bmatrix} 1 & -\nu & -\nu & 0 & 0 & 0 \\ -\nu & 1 & -\nu & 0 & 0 & 0 \\ -\nu & -\nu & 1 & 0 & 0 & 0 \\ 0 & 0 & 0 & 2(1+\nu) & 0 & 0 \\ 0 & 0 & 0 & 0 & 2(1+\nu) & 0 \\ 0 & 0 & 0 & 0 & 0 & 2(1+\nu) \end{bmatrix} \begin{bmatrix} \sigma_{11} \\ \sigma_{22} \\ \sigma_{33} \\ \sigma_{23} \\ \sigma_{13} \\ \sigma_{12} \end{bmatrix}$$

where, ε_{ij} and σ_{ij} are the strains and stresses of the material, and E and ν are the elastic modulus and Poisson's ratio.

The analytic solutions to be used to compare against the elastic finite element model can be modeled as contact between two elastic bodies. These solutions, which can serve as a reference point for the interaction, were first studied by Hertz in 1881.

Equations given in this section are derived from Fischer-Cripps Introduction to Contact Mechanics [29]. For his formulations Hertz assumed:

- i. The displacements and stresses must satisfy the differential equations of equilibrium for elastic bodies and the stresses must vanish at a great distance from the contact surface.
- ii. The bodies are in frictionless contact.
- iii. At the surface of the bodies, the normal pressure is zero outside and equal and opposite inside the circle of contact.
- iv. The distance between the surfaces of the two bodies is zero inside and greater than zero outside the circle of contact.
- v. The integral of the pressure distribution within the circle of contact with respect to the area of the circle of contact gives the force acting between the two bodies.

The elastic modulus of the contact can be expressed as a sum of the two bodies by the following relation:

$$(2.2) \quad \frac{1}{E_R} = \frac{1-\nu_i^2}{E_i} + \frac{1-\nu_s^2}{E_s}$$

where E_R is the reduced modulus, E_i and E_s are the elastic moduli of the indenter and sample, respectively, and ν_i and ν_s are Poisson's ratios of the indenter and sample, respectively. If the indenter is assumed to have a much larger modulus than the sample, the equation simplifies to:

$$(2.3) \quad E_R = \frac{E_s}{1-\nu_s^2}$$

For a spherical indenter as shown in Figure 13, the force-displacement relationship is:

$$(2.4) \quad P = \frac{4}{3} E_R \frac{a^3}{R}$$

where P is the force applied, R is the sphere radius, and a is the contact radius. For a sphere, the contact radius can be expressed as $a = \sqrt{Rh}$, where h is the indentation depth.

Substituting this into (2.4) gives:

$$(2.5) \quad P = \frac{4}{3} E_R R^{\frac{1}{2}} h^{\frac{3}{2}}$$

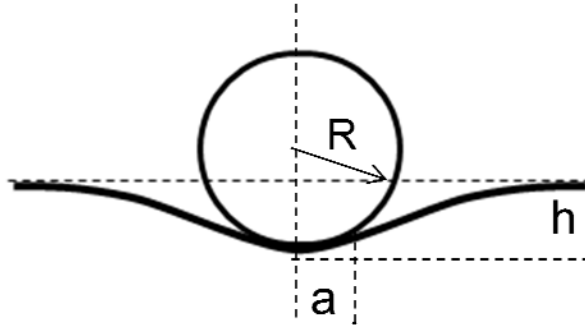


Figure 13: Elastic Spherical Indentation

In addition to force-displacement relationship, Hertz also developed equations for the stresses from the indentation. In the following equation, r is defined as a point along the contact between the two bodies that originates from the centerline (i.e. $r=0$ at centerline).

$$(2.6) \quad \sigma_z = \frac{-P}{\pi a^2} \frac{3}{2} \sqrt{1 - \frac{r^2}{a^2}} \quad , \quad r \leq a$$

For the spherical indenter geometry presented here, the indentation stress (or mean pressure, σ^*) and strain (ϵ^*) are given by

$$(2.7) \quad \sigma^* = \frac{P}{\pi a^2}$$

$$\epsilon^* = 0.2 \frac{a}{R}$$

where 0.2 is an empirically determined constant by Tabor (1951). [12] This constant has been verified by other investigations as well. Substituting the force-displacement into (2.7) yields:

$$(2.8) \quad \sigma^* = \frac{20}{3\pi} E_R \varepsilon^*$$

This is the stress strain curve for a linear elastic solid indented by a rigid sphere.

For a cylindrical, flat punch as shown in Figure 14, the force-displacement relationship and the stress field equation are:

$$(2.9) \quad P = 2aE_R h$$

$$(2.10) \quad \sigma_z = \frac{-P}{\pi a^2} \frac{1}{2} \sqrt{1 - \frac{r^2}{a^2}}, \quad r \leq a$$

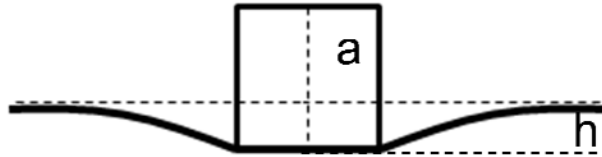


Figure 14: Cylindrical Flat Punch Indentation

For the cylindrical indenter geometry presented here, the indentation stress (or mean pressure, σ^*) and strain (ε^*) are given by

$$(2.11) \quad \sigma^* = \frac{P}{\pi a^2}$$

$$\varepsilon^* = \frac{h}{a}$$

These equations for the P and σ_z are used to find the force required for the depth of the indenter at the centerline and the stress along the bottom edge of the indenter, respectively.

2.2.2 Nonlinear Spherical Elastic Indentation Theory

As mentioned in Chapter 1, Lin *et al.* [12] developed a finite element model in order to derive force-displacement relations for spherical indentation of soft modulus materials for several hyperelastic functions. For the present study, the single-term Ogden function Lin used in his derivation is the primary focus. The single-term Ogden has an energy function (W) of form:

$$(2.12) \quad W = \frac{2\mu_0}{\alpha^2} (\lambda_x^\alpha + \lambda_y^\alpha + \lambda_z^\alpha - 3)$$

$$(2.13) \quad \sigma = \frac{2\mu_0}{\alpha} (\lambda^{\alpha-1} + \lambda^{-\alpha/2-1})$$

where μ_0 and α are fitting parameters and $\lambda = \lambda_y = \lambda_z = \lambda_x$ are the stretch ratios. μ_0 also has the physical meaning of the initial shear modulus. The stretch ratio is related to the strain by the equation: $\lambda = 1 + \varepsilon$. Taking these functions, Lin implemented the following approach:

1. Assumed stress of form

$$(2.14) \quad \sigma = f(C, \lambda)$$

2. Resolved the sign differences between standard engineering and common indentation notation by redefining

$$(2.15) \quad \begin{aligned} \lambda &= 1 - \varepsilon^* \\ \sigma^* &= -f(B, 1 - \varepsilon^*) \end{aligned}$$

3. Divide (2.15) by ε^* to obtain

$$(2.16) \quad \frac{\sigma^*}{\varepsilon^*} = -\frac{f(B, 1 - \varepsilon^*)}{\varepsilon^*}$$

4. For incompressible materials G_0 is equal to $E_0/3$ and taking ε^* to 0 and comparing that to (2.8) gives

$$(2.17) \quad \frac{20E_0}{3\pi(1-\nu^2)} = B\beta$$

5. Applying the (2.7) yields

$$(2.18) \quad \frac{P}{\pi a^2} = -f\left(B, 1 - 0.2 \frac{a}{R}\right)$$

6. Finally, the contact radius no longer maintains the relationship $a = \sqrt{Rh}$ for hyperelastic functions, therefore a new relation is assumed

$$(2.19) \quad a = R^{x-hy} h^z$$

where x , y , and z are constants. This relationship was formed by performing finite element analysis of the scenario. These models were studied for insight to be used in developing the models in this present study.

From these steps, a new force-displacement function was developed as described in Lin, *et al.*'s paper;

$$(2.20) \quad P = \frac{B\pi a^2}{\alpha} \left[\left(1 - 0.2 \frac{a}{R}\right)^{-\alpha/2-1} - \left(1 - 0.2 \frac{a}{R}\right)^{\alpha-1} \right]$$

$$(2.21) \quad B = \frac{40E_R}{9\pi}$$

This force-displacement equation is compared against the output from the nonlinear elastic finite element models.

2.2.3 Standard Sharp Indentation Theory

In order to fully understand the indentation process, the theory and application to the elastic-plastic materials was investigated. The finite element model is a power-law hardening, isotropic material that behaves according to the following equation:

$$(2.22) \quad \sigma = \begin{cases} E_R \varepsilon & , \varepsilon \leq \frac{\sigma_y}{E_R} \\ \sigma_y \left(\frac{E_R}{\sigma_y} \right)^n \varepsilon^n & , \varepsilon \geq \frac{\sigma_y}{E_R} \end{cases}$$

Where: ε is the total strain, σ_y is the yield stress of the material, and n is a work hardening exponent.

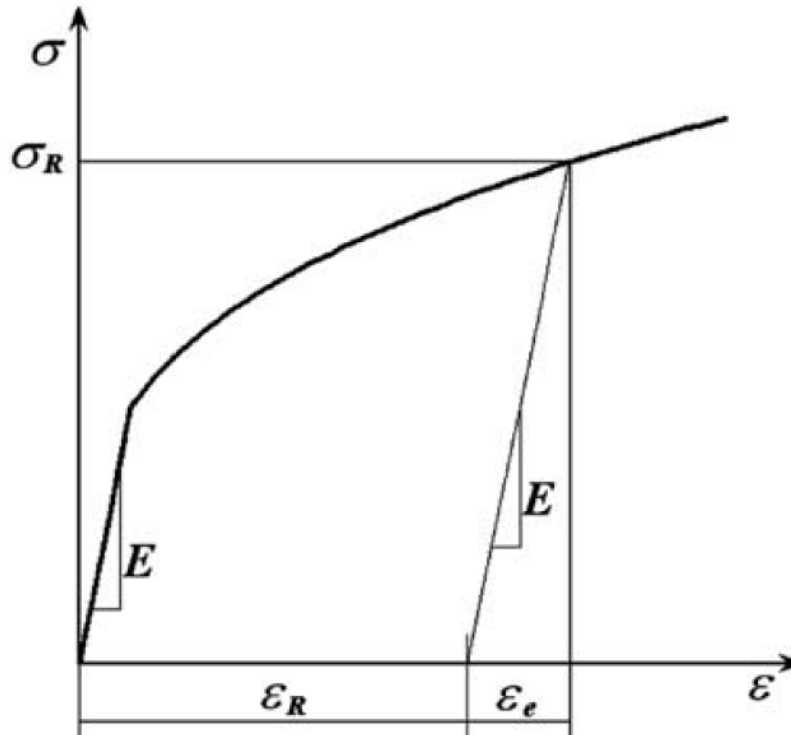


Figure 15: Elastic-plastic Power- Hardening Stress Strain Curve

In the present research, a total of 2200 points are used to describe the relationship between the flow stresses and the plastic strains with the plastic strains within the range of $0 \leq \epsilon_p < 200\%$. According to Y. Cao *et al.*, [30] this amount of the points is sufficient to well determine the plastic behavior of power law materials.

The standard method of using instrumented indentation was developed by Oliver and Pharr [3]. The load displacement curve shown in Chapter 1 is reprinted here for convenience in Figure 16.

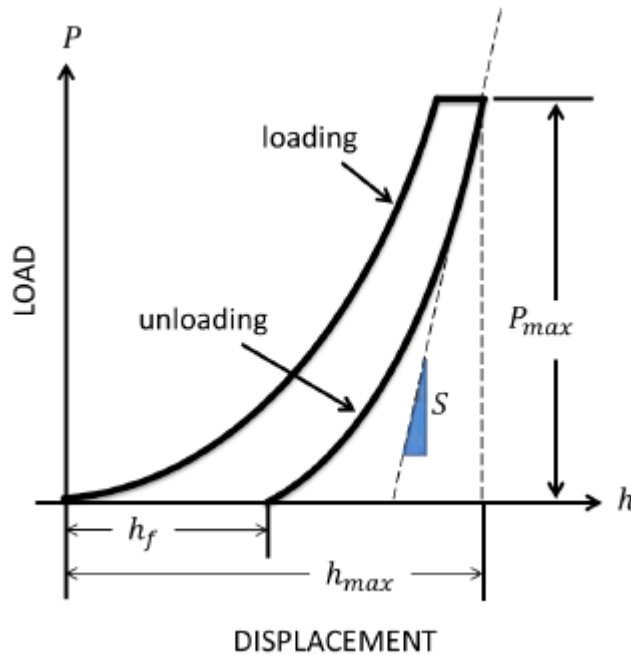


Figure 16: Standard Indentation Curve

One of the most common indenter geometries is the Berkovich Pyramid, shown in Figure 17. It is a three-sided pyramid with. Many indentation experiments are carried out with a Berkovich indenter made of diamond, which is the most common material for an indenter tip due to its high modulus (1170 GPa) and low Poisson ratio (0.07). In order to simplify the analysis, the Berkovich indenter head can be modeled as an analytically rigid cone

with a half apex angle of 70.3 degrees so that the cross sectional contact area is the same for a given depth.

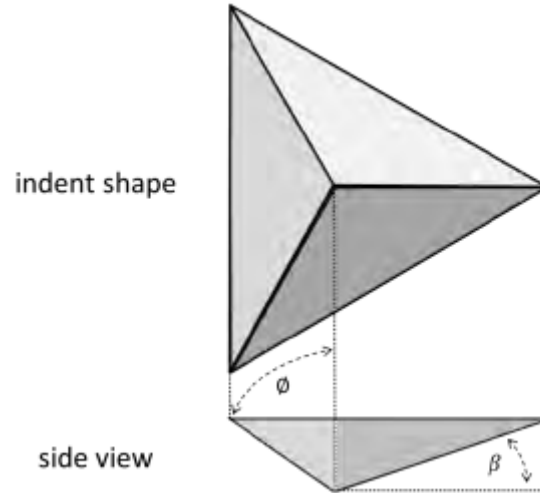


Figure 17: Geometry of a common Indenter head: Berkovich Pyramid

The data from the load-displacement curve is used to calculate the material properties of the specimen. This section begins with the equations for the desired properties (hardness H and elastic modulus E) and then presents the supporting calculations for those equations. Hardness is found by:

$$(2.23) \quad H = \frac{P}{A}$$

where P is the applied force and A is the projected contact area (defined in Eqn. 11). The Young's modulus (the modulus of elasticity, E) of the specimen is calculated from the reduced modulus E_R by rearranging equation (2.2) to the following:

$$(2.24) \quad E_s = (1 - \nu_s^2) \left[\frac{1}{E_R} - \frac{(1 - \nu_i^2)}{E_i} \right]^{-1}$$

The reduced modulus can be found using the relationship developed by Oliver and Pharr:

$$(2.25) \quad E_R = \frac{\sqrt{\pi} S}{2\beta\sqrt{A}}$$

where S is the initial slope of the unloading curve, also referred to as the contact stiffness, and β is the slope of the indenter tip.

2.2.4 Elastic-Plastic Spherical Theory

Furthering the investigation into standard engineering materials, another algorithm was studied and reproduced. This finite element model and accompanying coding analysis is based on a system developed by the civil engineering department at Columbia University. [5] For other similar processes using a sharp indenter, in order to find the complete range of the stress strain curve (to include the plastic regime) several indentations must be made with various indenter angles. This is because different materials can produce the same indentation curve. These are known as meta-materials. This can be very cumbersome and time consuming. This study used the mathematical method of representative stress and strain to find a unique solution for the stress-strain curve with a single, deep indentation. The authors, Zhao, *et al.* defined the representative strain to be the plastic strain, ε_p .

$$(2.26) \quad \varepsilon = \varepsilon_e + \varepsilon_p \equiv \varepsilon_e + \varepsilon_R \quad (\varepsilon_e \text{ is the elastic strain})$$

Correspondingly, the representative stress is:

$$(2.27) \quad \sigma_R \langle \varepsilon_R \rangle = \sigma_y \left[\frac{E_R}{\sigma_y} \left(\frac{\sigma_R \langle \varepsilon_R \rangle}{E_R} + \varepsilon_R \right) \right]^n$$

The representative stress is shown in Figure 15 in the previous as σ_R and there are two selections of σ_R in the analysis. For spherical indentation, dimensional analysis leads to

$$(2.28) \quad \frac{C}{\sigma_R \langle \varepsilon_R \rangle} = f\left(\frac{h}{R}, \frac{E_R}{\sigma_R \langle \varepsilon_R \rangle}, n\right)$$

and

$$(2.29) \quad \frac{S}{hE_R} = g\left(\frac{h}{R}, \frac{E_R}{\sigma_R \langle \varepsilon_R \rangle}, n\right)$$

From equations (2.28) and (2.29), Zhao *et al.* were able to produce the constants required to model the stress-strain curve for a material up to the ultimate yield point. They used extensive finite element analysis to find equations for the f and g. Two points were chosen from the loading portion of the force-indentation curve: one at $h_1 = 0.13 \cdot h/R$ and one at $h_2 = 0.3 \cdot h/R$. The point h_2 also corresponded to the maximum indentation depth. Figure 3 shows a rough approximation of their locations. These 2 points were substituted into equation (2.28) to produce, along with (2.29), the 3 surfaces required to find the solution for E_R , n , and σ_y .

$$(2.30) \quad \frac{C_1}{\sigma_R^1 \langle \varepsilon_R^1 \rangle} \equiv \frac{P_1}{h_1^2 \sigma_R^1 \langle \varepsilon_R^1 \rangle} = f_1\left(\frac{E_R}{\sigma_R^1 \langle \varepsilon_R^1 \rangle}, n\right)$$

$$(2.31) \quad \frac{C_2}{\sigma_R^2 \langle \varepsilon_R^2 \rangle} \equiv \frac{P_2}{h_2^2 \sigma_R^2 \langle \varepsilon_R^2 \rangle} = f_2\left(\frac{E_R}{\sigma_R^2 \langle \varepsilon_R^2 \rangle}, n\right)$$

$$(2.32) \quad \frac{S}{h_2 E_R} = g\left(\frac{E_R}{\sigma_R^2 \langle \varepsilon_R^2 \rangle}, n\right)$$

The forward analysis used by Zhao, *et al.*, produced fittings for the values of f_1 , f_2 , and g . They are:

$$(2.33) \quad f_1(m_1, n) = h_1(m_1) \times k_1(n)$$

$$(2.34) \quad f_2(m_2, n) = h_2(m_2) \times k_2(n)$$

$$(2.35) \quad g(m_2, n) = A_2(n) + \frac{A_1(n) - A_2(n)}{1 + [m_2 / q(n)]^{p(n)}}$$

$$\text{Where } m_1 = \frac{E_R}{\sigma_R^1 \langle \varepsilon_R^1 \rangle} \text{ and } m_2 = \frac{E_R}{\sigma_R^2 \langle \varepsilon_R^2 \rangle}$$

$$(2.36) \quad h_1(m_1) = 32.77 - 52.59 \ln(m_1) + 33.46(\ln(m_1))^2 - 4.800(\ln(m_1))^3 + 0.2147(\ln(m_1))^4$$

$$(2.37) \quad h_2(m_2) = 3.817 - 12.73 \ln(m_2) + 11.99(\ln(m_2))^2 - 2.032(\ln(m_2))^3 + 0.1049(\ln(m_2))^4$$

$$(2.38) \quad k_1(n) = 1.001 - 0.2610n - 0.5217n^2 + 0.1547n^3$$

$$(2.39) \quad k_2(n) = 1.002 - 0.7637n - 1.920n^2 + 1.255n^3$$

$$(2.40) \quad A_1(n) = 3.66556 + 0.0244179n$$

$$(2.41) \quad A_2(n) = 6.06122 - 2.15891n$$

$$(2.42) \quad q(n) = 29.0856 - 24.3547n$$

$$(2.43) \quad p(n) = 1.31861 - 0.154675n$$

For this present study the reverse analysis Zhao, *et al.* developed using these set of equations, (2.30) - (2.43), is investigated. This is discussed further in Chapter 5.

2.3 Muscle Structure and Tensile Tests Theory

In order to understand the strength of a muscle, it is important to understand how it works. The force required to stretch a muscle to a given length can be divided into two components: active and passive. The passive component is the contribution from the

material structure and the properties of the myofilaments. The active force component is the contribution from the contraction of the myofilaments. An example force-length curve is shown in Figure 18. The active component cannot be measured directly. The passive and total forces of the muscle are measured separately and the difference between the two represents the contribution of the active state. For the purposes of this study, the properties of the individual muscle motor units are examined in the passive state (i.e. no electrically stimulated contraction of the muscles).

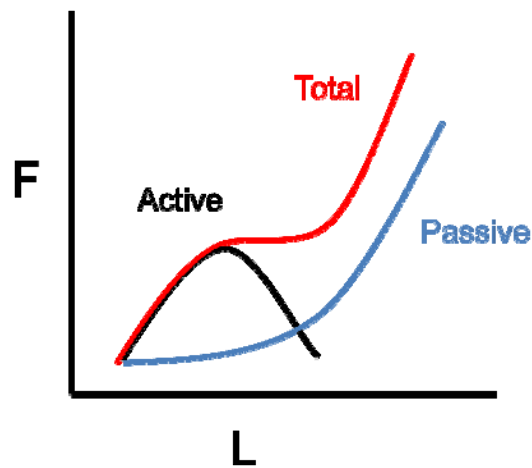


Figure 18: Force-Length Example Diagram for Muscles showing the Total force-length response is a sum of the Active and Passive Properties of the muscle

Passive muscle tissue is a viscoelastic, hyperelastic, anisotropic material. However, after preconditioning, the viscoelastic nature of the material becomes minimal and the material is then regarded as pseudo-elastic. Pseudo-elastic materials behave as one elastic material during loading and another one during unloading. [5] Additionally, the organization of the muscle fibers simplifies the material to a transversely isotropic material and is assumed to be incompressible.

In addition to the indentation tests, the theory of which has already been discussed at length, uniaxial tensile tests were also attempted on the muscle samples. Tensile tests involve applying a force to a sample in one direction and observing the change in its length. It is one of the fundamental tests of materials strength. For a uniaxial load the material described in equation (2.1) simplifies the engineering stress and engineering strain described by:

$$(2.44) \quad \sigma = E\varepsilon$$

where $\varepsilon = \frac{\Delta L}{L_0}$ and $\sigma = \frac{P}{A_0}$. L_0 and A_0 are the initial length and area of the specimen being tested [31].

2.4 Summary

In this Chapter the mathematical formulations for the finite element model materials were outlined. The derivations of the nonlinear elastic and the elastic-plastic models were discussed. These equations and the Hertzian linear elastic equations are used to verify the models developed in Chapter 3.

In addition to the mathematical formulas for indentation, the structure of the hawkmoth muscle was explained. The flight mechanics of the moth and how the muscles drive that motion were diagramed. This information is used to analyze the experimental data.

III. Finite Element Model Development

3.1 Chapter Overview

In this chapter the development and validation of the FE models are discussed. Issues such as element type and number, boundary conditions, analysis techniques, and contact type are analyzed. The mesh resolution of the sample and the given indenter for the elastic sample will be compared to Hertz contact equations from Chapter 2 to show convergence.

3.2 Finite Element Overview

In this section the finite element models of the three indenter head geometries probing into an elastic half-space is explained. The factors going into the mesh are explored and the results are validated against the analytic Hertzian solutions to ensure mesh refinement so that the models may be used in the analysis section in Chapter 5.

The commercial finite element analysis software package ABAQUS, version 6.10 is used in the indentation simulation. Information in this section about the finite element model comes from the ABAQUS Users Manual [32]. ABAQUS is a suite of powerful engineering simulation programs, based on the finite element method, which can solve problems ranging from relatively simple linear analysis to the most challenging nonlinear simulations.

3.3 Analysis Considerations

ABAQUS consists of two main analysis modules: ABAQUS/Standard and ABAQUS/Explicit. ABAQUS/Standard is a general-purpose analysis module that can solve a wide range of linear and nonlinear problems efficiently, accurately and reliably.

ABAQUS/Explicit is a special-purpose analysis module that uses an explicit dynamic finite element formulation. It is suitable for short, transient dynamic events. The indentation procedure is assumed to be quasi-static problem, in which no rate effect is considered, therefore ABAQUS/Standard is employed in this work.

In the indentation simulation, there are two sources of nonlinearity: material nonlinearity and geometric nonlinearity. The indentation procedure can produce large deformation in the solids underneath and near the indenter. The magnitude of displacement can affect the response of the structure (geometry nonlinearity). ABAQUS uses the modified Newton-Raphson method to obtain solutions for nonlinear problems in the Standard module.

3.4 Models

For all of the simulations in this study the indenter head is much stiffer than the medium being indented. This allows the indenter head to be modeled as an analytically rigid solid. The rigid surface is associated with a rigid body reference node, whose motion governs the motion of the surface. Since only one node is computed, this saves computer resources and simplifies analysis.

Both the indenter and half space are modeled as axisymmetric geometry. The bottom of the model is fixed and the remaining two sides are free as shown in Figure 19. Four-node axisymmetric linear quadrilateral elements are utilized for the half-space. Reduced integration is employed to spare calculation time. The element type for the elastic and elastic-plastic materials used in ABAQUS is 'CAX4R', in which the letter or number indicates the element is continuum, axisymmetric, 4-node bilinear, reduced integration

with hourglass control respectively. This element is not able to be used for hyperelastic material problems. The hybrid version of the CAX4R is used in this case called CAX4RH. The axisymmetric elements are shown in Figure 20.

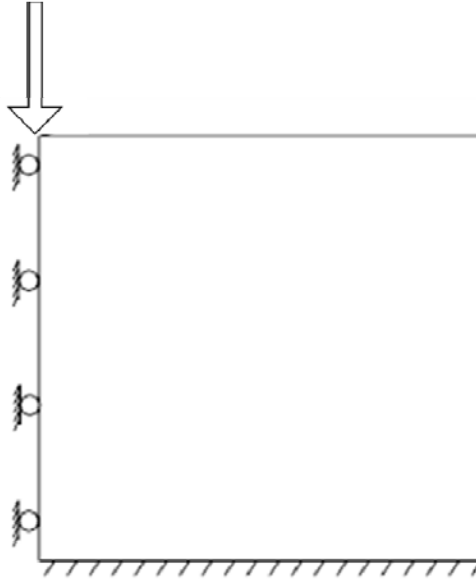


Figure 19: Model Boundary Conditions: Y-axis Symmetry (Left side) and Fixed (Bottom)

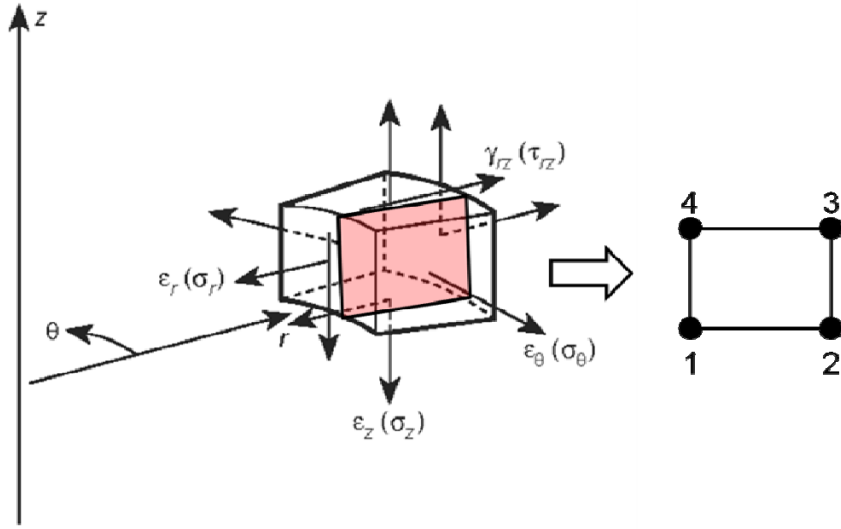


Figure 20: Diagram of simplification made by assuming no variation in the angular direction for the CAX4R and CAX4RH elements

The mesh is designed so that the meshing is refined near the indenter (in order to resolve the contact conditions and allow for accurate contact area determination), but also is sufficiently large so that it approximates a semi-infinite solid. Accordingly, the mesh is chosen large enough for each calculation so that the results obtained are insensitive to the movement of the outer boundaries of the mesh. For all three models, a structured grid is used in order to decrease computational time and to resolve the fine mesh required at the point of indentation. The grid can be seen in Figure 21 and Figure 22 for the flat punch and sphere, respectively. Size of the sample half space (LxW) in the figures) is determined for each scenario due to varying indentation depths and material effects.

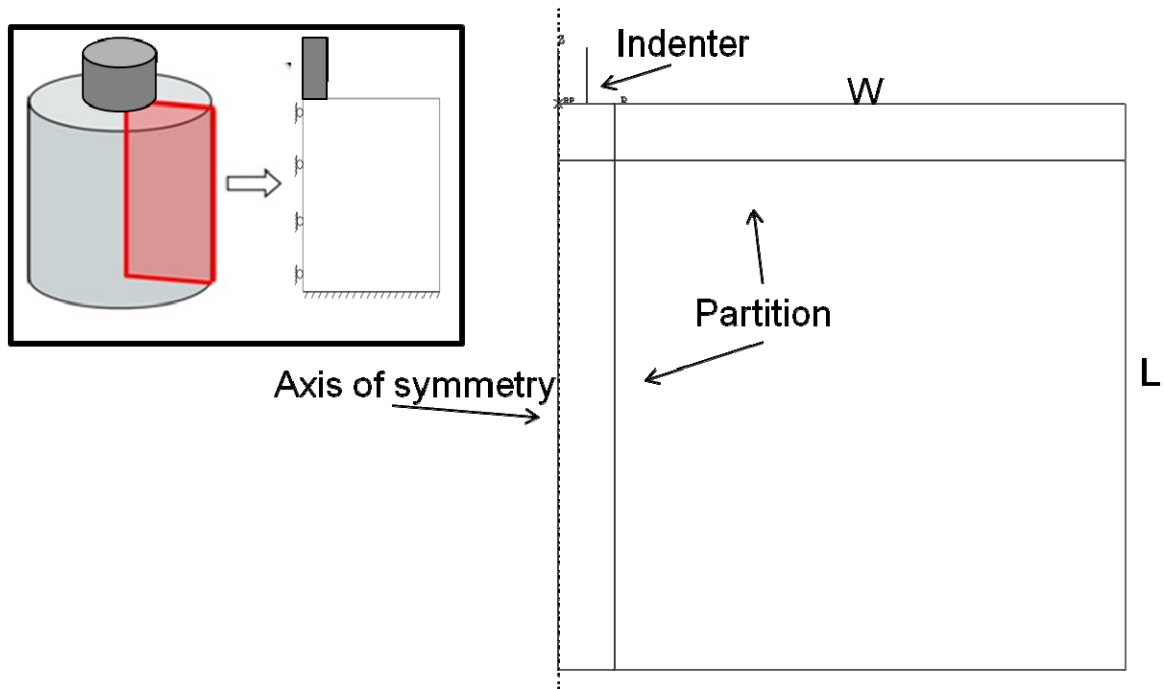


Figure 21: ABAQUS Axisymmetric Model of Cylindrical Flat Punch indenting a sample with partition lines to divide sample in order to refine the mesh. Inset: axisymmetric assumption diagram

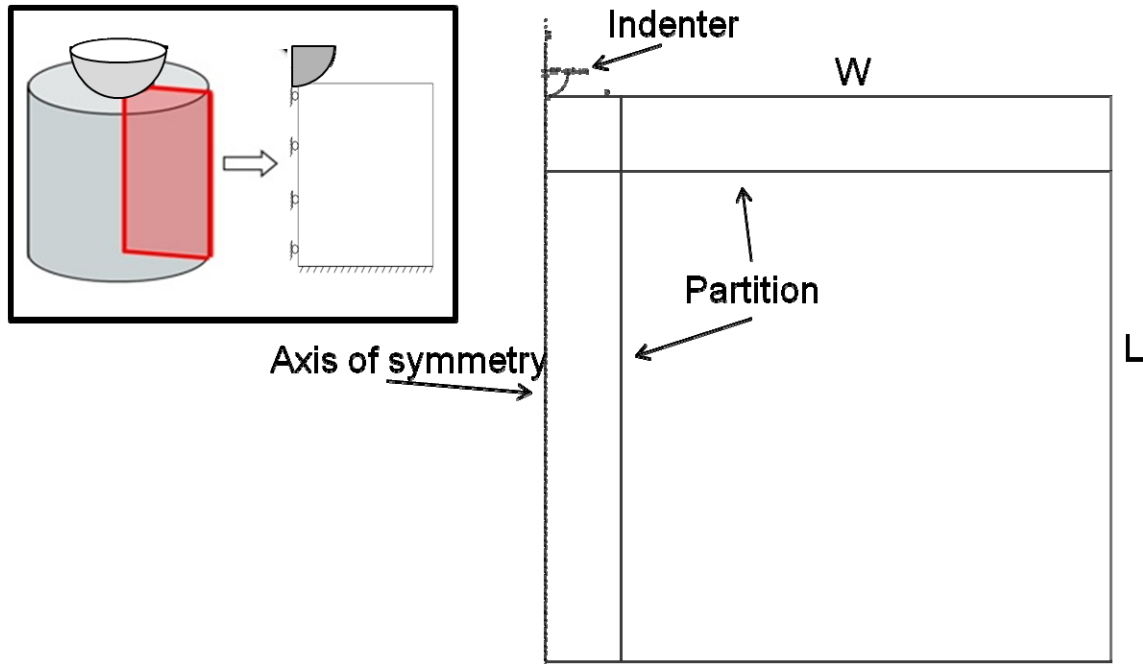


Figure 22: ABAQUS Axisymmetric Model of Sphere indenting a sample with partition lines to divide sample in order to refine the mesh. Inset: axisymmetric assumption diagram

A 3D representation of the 2 types of models can be seen in Figure 23. An example mesh can be seen in Figure 24 with note of the additional refinement of the mesh on the right-hand side of the figure.

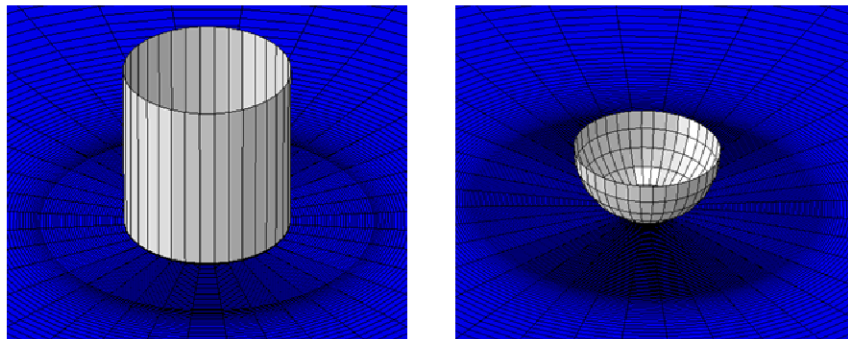


Figure 23: Close up View of 3D revolution of Axisymmetric Models:

Flat Punch (Left) & Spherical (Right)

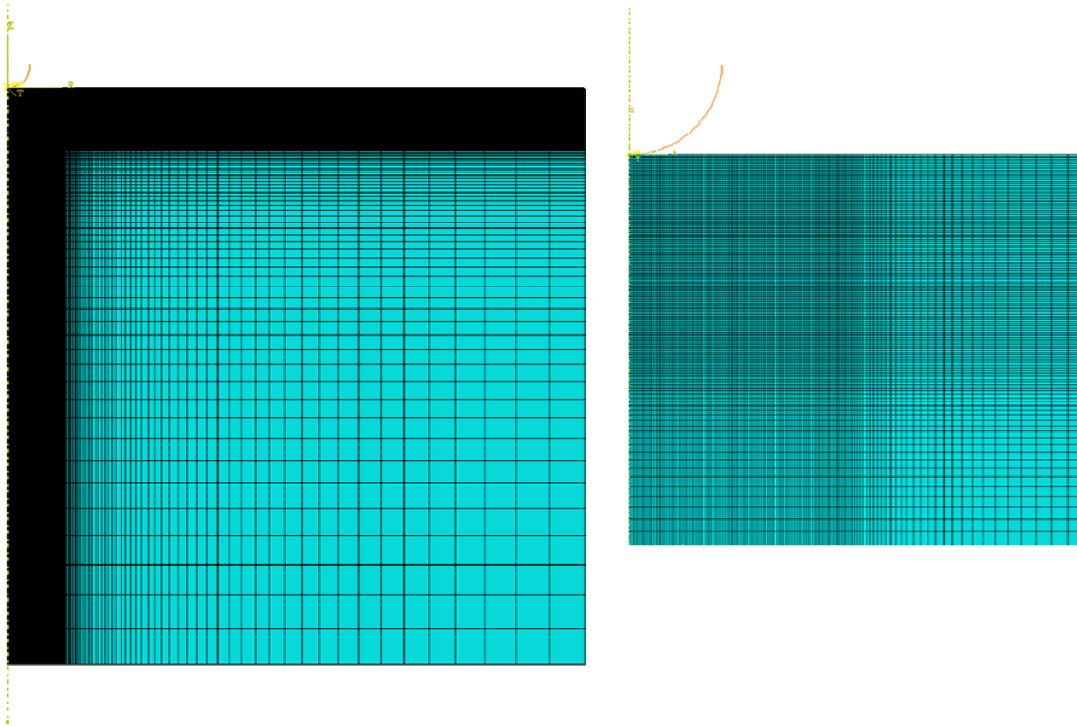


Figure 24: Example mesh of a sample as a whole (left) and close up showing the refined area underneath the indenter (right)

3.7 Summary

In summary, for a given scenario, an axisymmetric model is used with either a spherical or cylindrical flat punch indenter. The scenarios are considered to be quasi-static to simulate the rate-independent nature of preconditioned biological tissues. The mesh and dimensions of the models are varied according to the experiment to be evaluated.

IV. Experimentation Methodology

4.1 Chapter Overview

In this Chapter the methodology for the attempted experiments is outlined. The thought behind this methodology is explained and the assumptions for the data gathered are discussed.

4.2 Nanoindentation Experimentation

Hawkmoth pupae were maintained in a temperature controlled room with a 14 hour on/ 10 hour off light/dark cycle until they hatched. More information of the raising of the hawkmoth can be found in the appendix. Once the moths hatched, they were moved to a secondary cage until they were needed. The moths could last up to approximately a week in this cage before they died.

Prior to the dissection, a glass slide was attached to a metal puck with Crystalbond™ (Crystalbond, AREMCO, Valley Cottage, NY). (Figure 25) Crystalbond™ is a heat-activated adhesive material. A thin ring was attached to the glass slide with cyanoacrylate adhesive (super glue). This ring contains the saline solution so that the sample will not desiccate during the experiment. Small pieces of glass are also adhered to glass slide. These are approximately the same height as the tissue sample. It was hoped that these glass blocks could be used as a guide for the nanoindenter to gauge the distance to the surface.

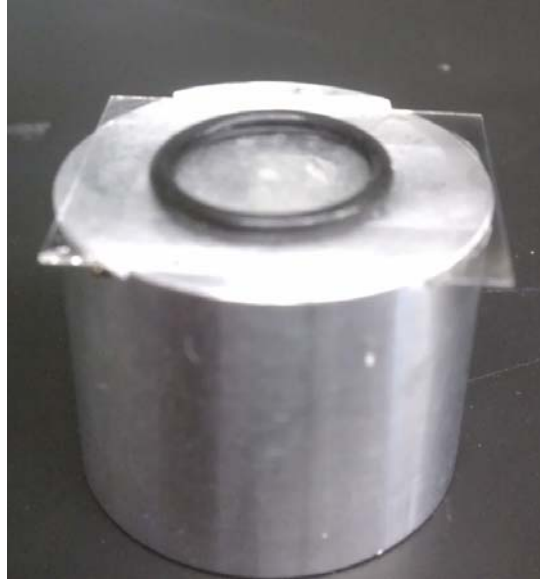


Figure 25: Sample Puck for indentation experiment with rubber ring attached to glass slide to hold saline solution

The moths were taken out of their cage approximately 1 hour before the test was conducted and asphyxiated using a paper towel dipped in acetone in a small closed off container. This was to maintain the freshness of the sample and an attempt to prevent decomposition as much as possible.

Once the insects were dead, the wings, head, abdomen, and legs were all removed using small scissors. This left only the thorax remaining. The thorax was held under a slow stream of running water and scrubbed with a toothbrush to remove the small scales. This allowed the exoskeleton to be clearly visible to aid in the dissection. The scissors were again used to clip the thorax along the dashed line shown in Figure 26.

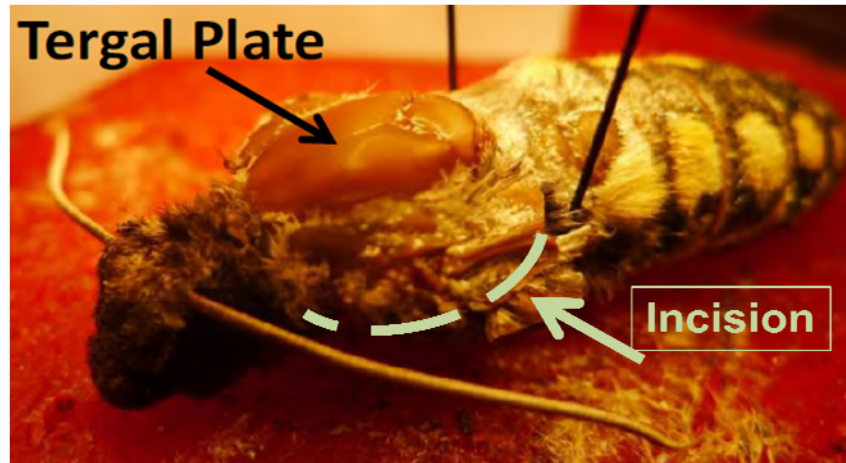


Figure 26: Partially Dissected Moth highlighting the point of incision of the exoskeleton (wings are removed)

The bottom of the exoskeleton was removed, leaving the top of the exoskeleton and exposed muscles. A cut was made at the front and rear of the thorax, slicing through the DLMs. As the DLMs are not attached to the top of the thorax, this allowed the bundle to be removed with tweezers. Care was taken to cut the muscles as close to the exoskeleton as possible to remove the largest amount of tissue. Isolated muscle tissue can be seen in Figure 27. Drops of saline solution were applied to the tissue samples to maintain moisture until they were ready.



Figure 27: Isolated Individual muscle units of the Hawkmoth DLMs

When ready to test, the muscle sample was patted dry to remove excess moisture and weighed to the nearest 0.001 g. A small bit of cyanoacrylate was placed on the glass slide next to glass surface find aide. The muscle sample was placed on top of the adhesive as shown in Figure 28. The sample was covered with a moist paper towel and allowed to sit for several minutes. This allowed the adhesive to dry while maintaining the moisture of the muscle. Once dry, the ring was filled with saline. This setup is much like that used by V.T. Nayar *et al.* [13] indentation of porcine sclera mentioned in Chapter 1.

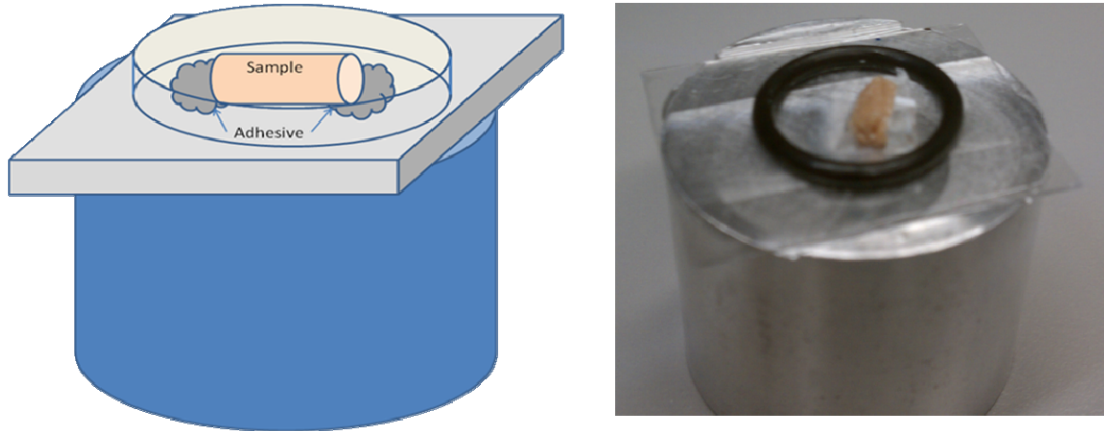


Figure 28: (left) Cartoon showing sample/adhesive interaction and (right) muscle sample in solution adhered to slide with glass block flush with its right edge.

The puck as a whole was weighed in order to be weighed again following the test to determine if there was any water lost from the sample. The sample puck was then placed in the Nanoindenter G200 test rack as shown in Figure 22.

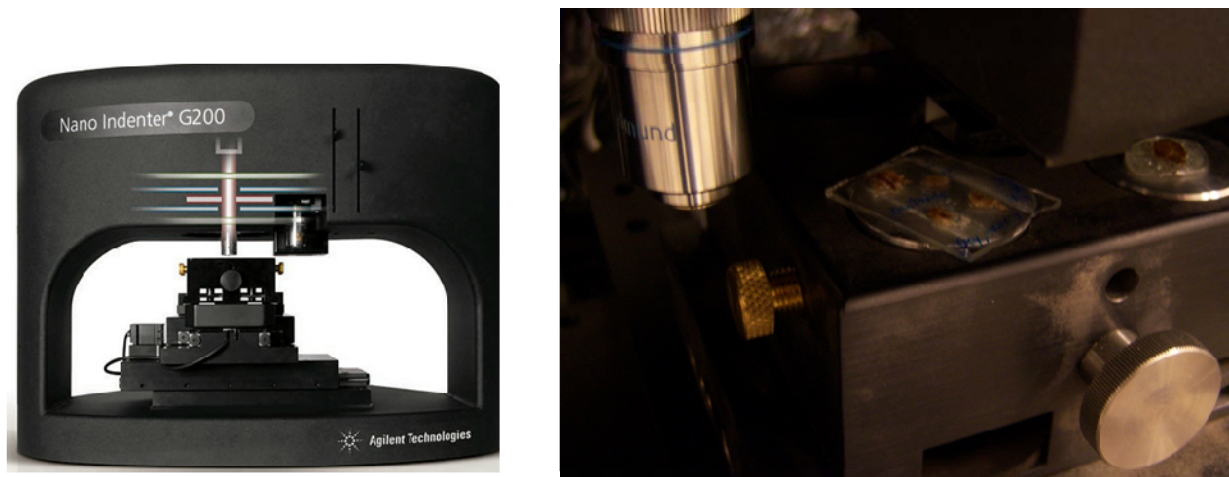


Figure 29: (a) Agilent G200 Nanoindenter (b) Sample Puck in Test Rack of Indenter

Two indenter heads were used: 120 μ m and 300 μ m radius spherical head. The Standard XP Indentation Head was used. The surface sensitivity was set at “very fine” with an approach distance of 1 mm. Through the nanovideo camera microscope, locations on the sample and on the glass near the sample were chosen. The indenter was programmed to indent the glass and then use the height location to zero in on the surface of the sample. It was unable to find the surface of the muscle for either the 120 μ m or 300 μ m indenter head. Discussion of this outcome is in Chapter 5.

4.3 Uniaxial Tensile Experimentation

The second experiment with the hawkmoth muscle fiber examined the tensile properties of the specimen. Dissection and isolation of the muscle units occurred as in section 3.3.1. Each sample was weighed and measured. Length and the width at three discrete points were measured using a digital microscope. The three widths were averaged and treated as approximately the diameter muscle. This diameter was used to find the cross sectional area used for the stress calculations.

The material was tested using the Agilent T150 Universal Testing Machine (UTM) shown in Figure 30 along with its specifications. The T150 has the necessary displacement and load resolution required for a sample of this size with this low of an expected modulus.



Agilent T150 UTM Specifications

Maximum load	500 mN (50.8 gm)
Load resolution	50 nN (5.1 μ gm)
Maximum actuating transducer displacement	\pm 1 mm
Displacement resolution	<0.1 nm
Dynamic displacement resolution	<0.001 nm
Maximum crosshead extension	200 mm
Extension resolution	35 nm
Extension rate	0.5 μ m/s to 5 mm/s
Dynamic frequency range (sample dependent)	0.1 Hz to 2.5 kHz

CDA Option

Force amplitude range	0.1 μ N to 4.5 mN
Frequency range characterization of instrument dynamic response (sample dependent)	0.01 Hz to 200 Hz

Figure 30: Agilent T150 UTM and Specifications

In order to attach the samples to the machine, an interface is needed between the grips and the tissue sample. As was done by Calvo, *et al.* [17], the specimen is attached using cyanoacrylate to small pieces of sandpaper which in turn are attached to paper templates. These pieces of sandpaper prevent slippage between the sample and the clamps. The applicability of the sandpaper/glue combination is confirmed in Ng *et al.* study in 2005 [33]. The paper templates allow for the handling of the samples with placing too much stress on them before the testing starts. The templates are connected with tape. Once the sample is clamped into the testing apparatus, the tape is cut, allowing for the machine stress-strain analysis to start. Setup can be seen in Figure 31.

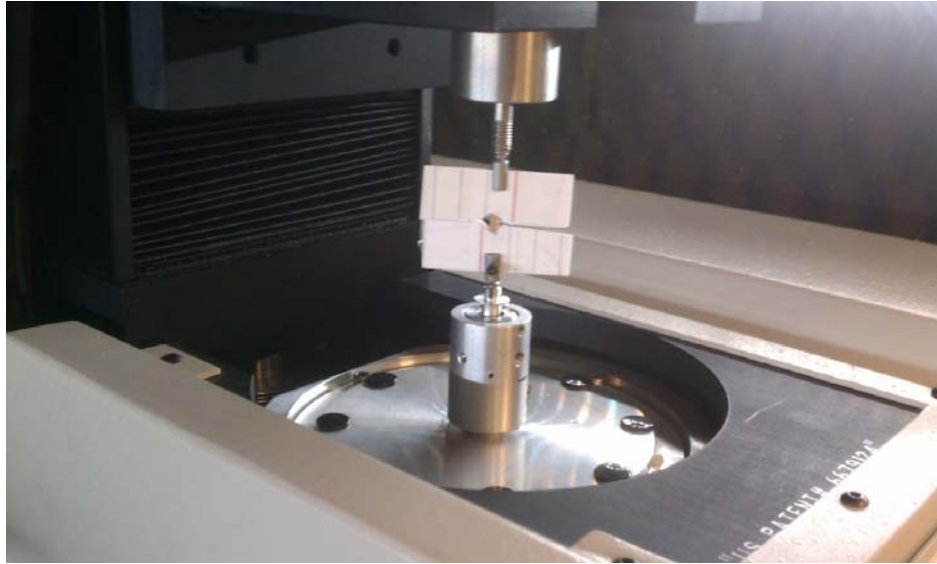


Figure 31: Template card technique showing Sample in Testing Machine. Edges of card have been cut, allowing the sample to be stretched.

Due to the size limitations of the sample and the restrictive nature of the template, each of the gauge lengths for the tests was restricted to approximately 2 mm. Sample hydration was limited to the beginning of each, much in the way that Gras, *et al.* [16], did in their testing of the sternocleidomastoideus muscle. This lack of hydration throughout the test resulted in the inability to perform a preconditioning cycle to the specimen. According to theory in Chapter 2, the elastic properties of the muscle would vary with different strain rates due to the viscoelastic nature of the unconditioned material. To investigate this, three strain rates were to be tested ($3e-4$, $1e-4$, and $1e-3$ mm/mm/s), however, the uniaxial testing was only completed for 4 samples at strain rates of $3e-4$ mm/mm/s. The clamps for the testing machine split and new ones were unable to be procured in time to complete the remainder of the planned tests. Results that were obtained as well as improvements on the testing method are discussed in Chapter 5.

V. Analysis and Results

5.1 Chapter Overview

In this Chapter, the validity and usefulness of the finite element models are analyzed and their results commented on. The nanoindentation experiment was analyzed to determine why the experiment failed and whether the Agilent G200 is useful for materials with similar properties as the muscle. Results from the uniaxial tension tests are reported and the results critiqued to determine better testing methods.

5.3 Results of Finite Element Simulations

In this section, 3 scenarios are analyzed. The first looks at the algorithm developed for elastic-plastic spherical indentations. The second looks at the porcine sclera experiment discussed in the literature review and how boundary effects could come into play for similar future experiments. The third example looks at the effect of friction on the results of Lin, *et al.* in their analysis of mouse cartilage.

5.3.1 Spherical Indenter into Elastic Plastic Medium

In this scenario, the elastic plastic properties of a material are determined by the analysis method developed by Zhao *et al.* [5] described in Chapter 2. The forward analysis fitting functions shown in equations (2.30) - (2.43) are used. Equations (2.30) through (2.32) are repeated here for convenience.

$$(2.30) \quad \frac{C_1}{\sigma_R^1 \langle \varepsilon_R^1 \rangle} \equiv \frac{P_1}{h_1^2 \sigma_R^1 \langle \varepsilon_R^1 \rangle} = f_1\left(\frac{E_R}{\sigma_R^1 \langle \varepsilon_R^1 \rangle}, n\right)$$

$$(2.31) \quad \frac{C_2}{\sigma_R^2 \langle \varepsilon_R^2 \rangle} \equiv \frac{P_2}{h_2^2 \sigma_R^2 \langle \varepsilon_R^2 \rangle} = f_2\left(\frac{E_R}{\sigma_R^2 \langle \varepsilon_R^2 \rangle}, n\right)$$

$$(2.32) \quad \frac{S}{h_2 E_R} = g\left(\frac{E_R}{\sigma_R^2 \langle \varepsilon_R^2 \rangle}, n\right)$$

The reverse analysis requires inputs for P_1 , P_2 , h_1 , h_2 , and S . These inputs can be measured from an experiment. However, in the absence of experimental data finite element analysis may be used to produce these values. Materials with known values for σ_y , E , and n (ν is assumed to be 0.3) can be input into a finite element model. The force-indentation data may be extracted from the results of this analysis and the values for P_1 , P_2 , h_1 , h_2 , and S can be found.

For example, the properties for A533-B steel are approximately $E = 210$ GPa, $\sigma_y = 400$ MPa, and $n = 0.127$ [5]. These values were input into the model outlined in Chapter 3 for the spherical indentation. The radius of the indenter was set to be $788 \mu\text{m}$ and the sample to be 50 times the radius to remove any boundary condition effects.

The first step was to check the mesh refinement against the spherical elastic analytic equations shown in Chapter 2. The depth of indentation is set to the maximum value required for the algorithm, $h=0.3R$, or $h = 236.4 \mu\text{m}$. This indentation can be seen in Figure 32.

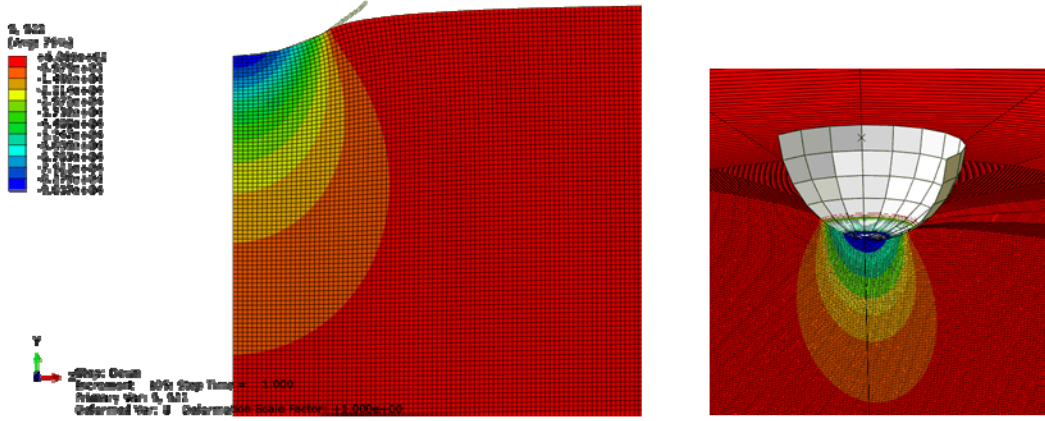


Figure 32: Spherical Elastic Maximum Indentation, 2D (left) and 3D (right). Colors indicate stress in the vertical direction (MPa)

The force indentation curve for 4 mesh sizes are compared in Figure 33. The ‘100x100’ refers to the number of elements in the corner square of the mesh. The larger the number is, the finer the mesh.

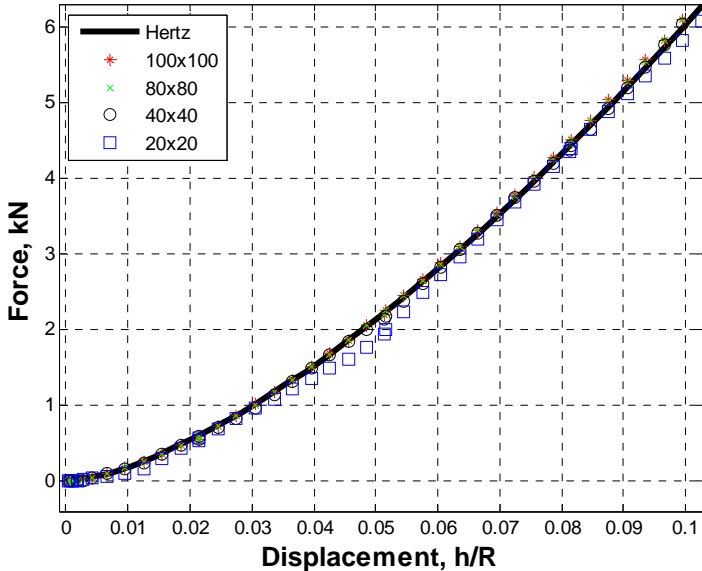


Figure 33: Mesh Resolution Comparison, F-d Elastic Spherical

The stress under the indenter at the maximum depth is compared with the analytic solution in Figure 34. The maximum stress at the middle of the indenter is predicted better using the coarse mesh. Due to there being such a large displacement, the material is out of the linear range. Since the force-displacement diagram is the driver for the analysis, that refinement is the primary mesh.

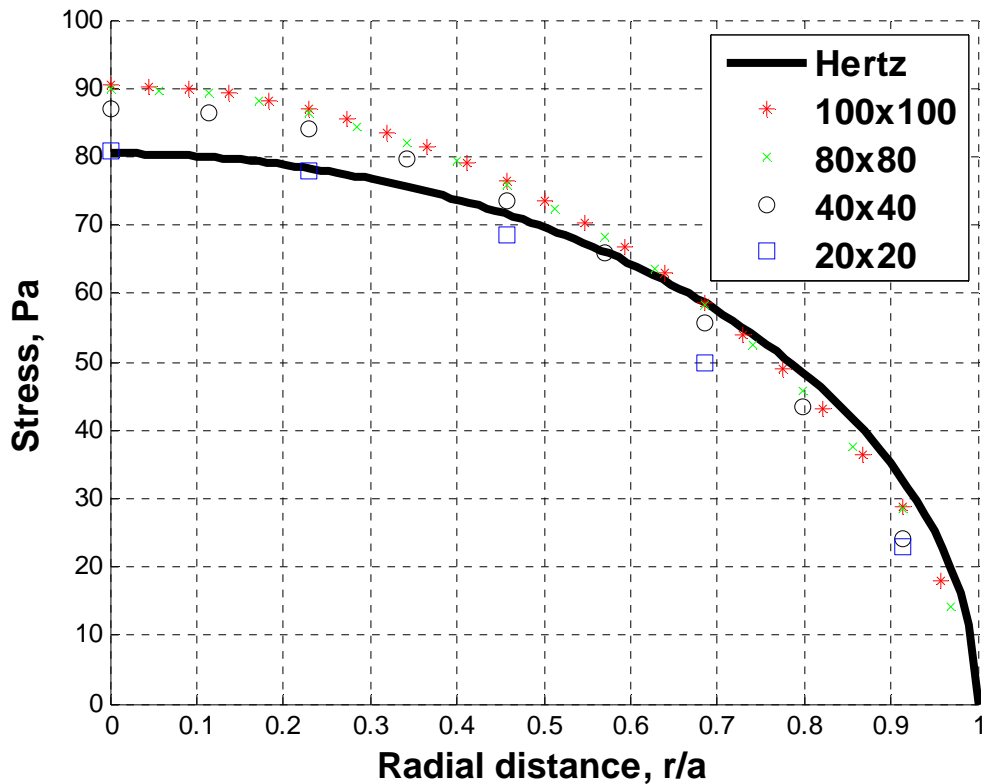


Figure 34: Mesh Resolution Comparison, F-d Elastic Spherical

The finest mesh was considered to have converged; therefore it was used to determine the values required for the analysis. The material properties of the model were changed to include the work hardening strain values ($E=210$ GPa, $\sigma_y=400$ MPa, and $n = 0.127$) and the indentation analysis was run again. The stress field can be seen in at the maximum

indentation depth in Figure 35 and after the indenter has separated from the surface in Figure 36. Residual stresses can be seen in the in the sample. The force indentation curve for this scenario can be seen in Figure 37.

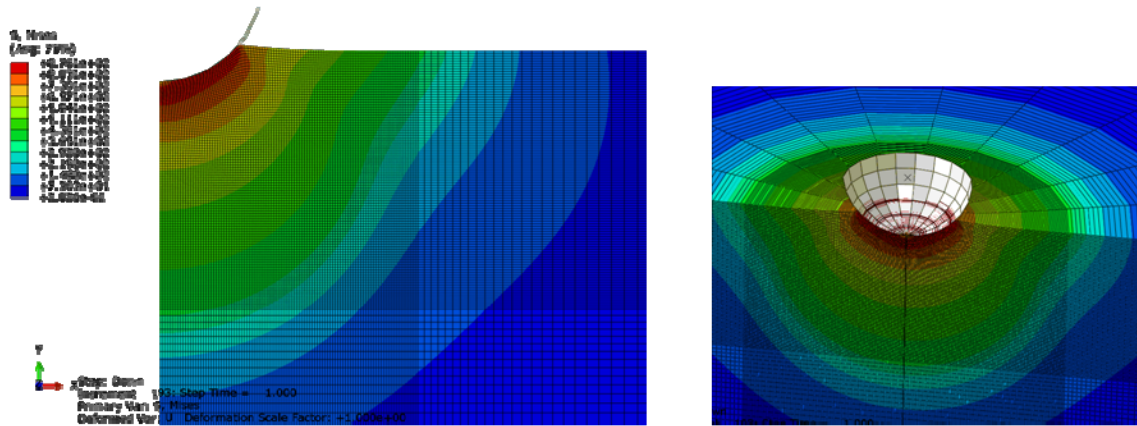


Figure 35: Spherical Plastic Maximum Indentation, 2D (left) and 3D (right)

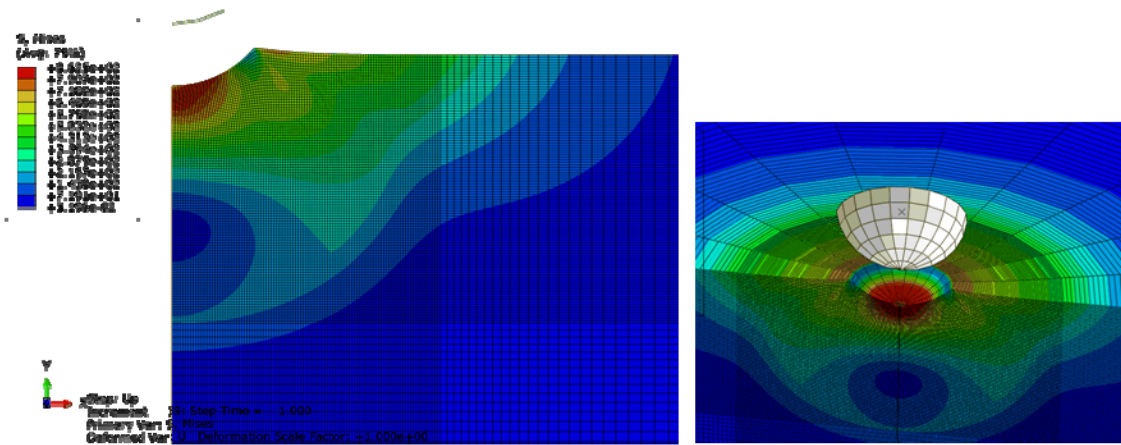


Figure 36: Spherical Plastic Residual Indentation, 2D (left) and 3D (right)

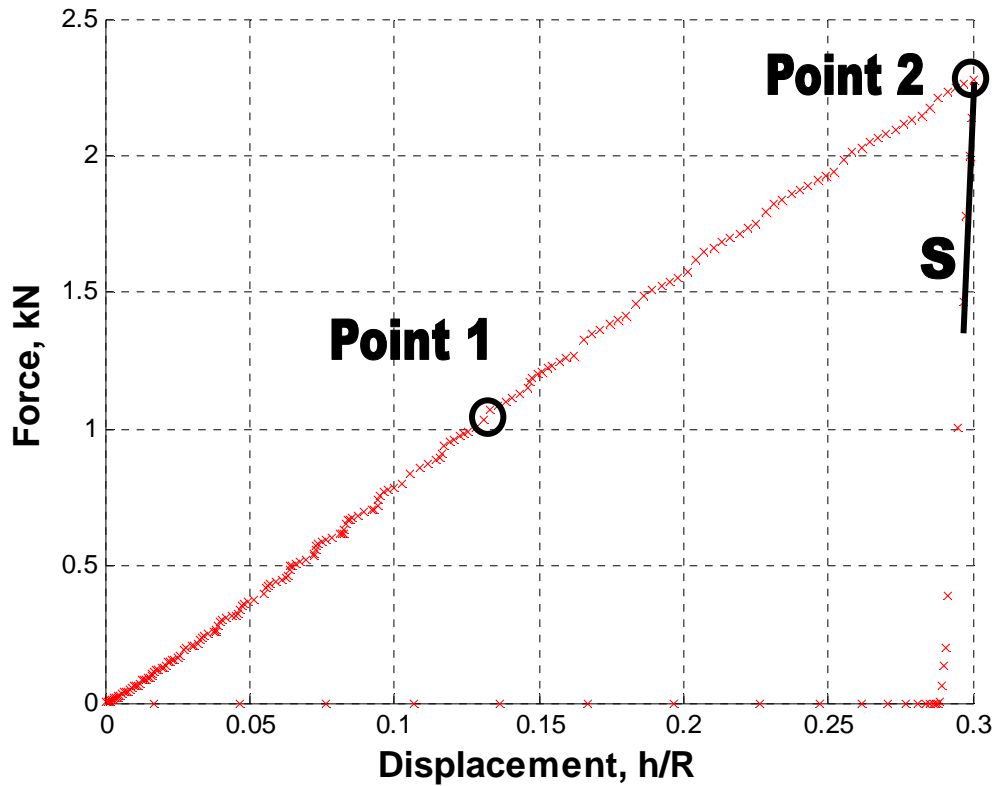


Figure 37: Force Displacement Curve for Forward Analysis ($R=788 \mu\text{m}$)

The values for P_1 , P_2 , h_1 , h_2 , and S are extracted from Figure 37 and are shown in Table 1. These values are used to determine the constants to be input into the algorithm shown in Table 2.

Table 1: Measured Values from Force Indentation Curve

h_1 (μm)	h_2 (μm)	P_1 (N)	P_2 (N)
102.44	236.4	1023.8	2280.4

Table 2: Input Values to Zhao Algorithm

C_1 (GPa)	C_2 (GPa)	S (MPa*m)
97.56	40.81	349.3

From here the flow chart shown in Figure 38 may be followed to determine the material properties. The steps in this flow chart are solved using the code found in Appendix B. The range for E/σ_y was initially set to be 100 to 1000, the range for n was 0 to 0.6, and the σ_y/σ_0 range was set to 0.5 to 1.5. This allowed for a wide range of engineering materials to be in consideration for this analysis.

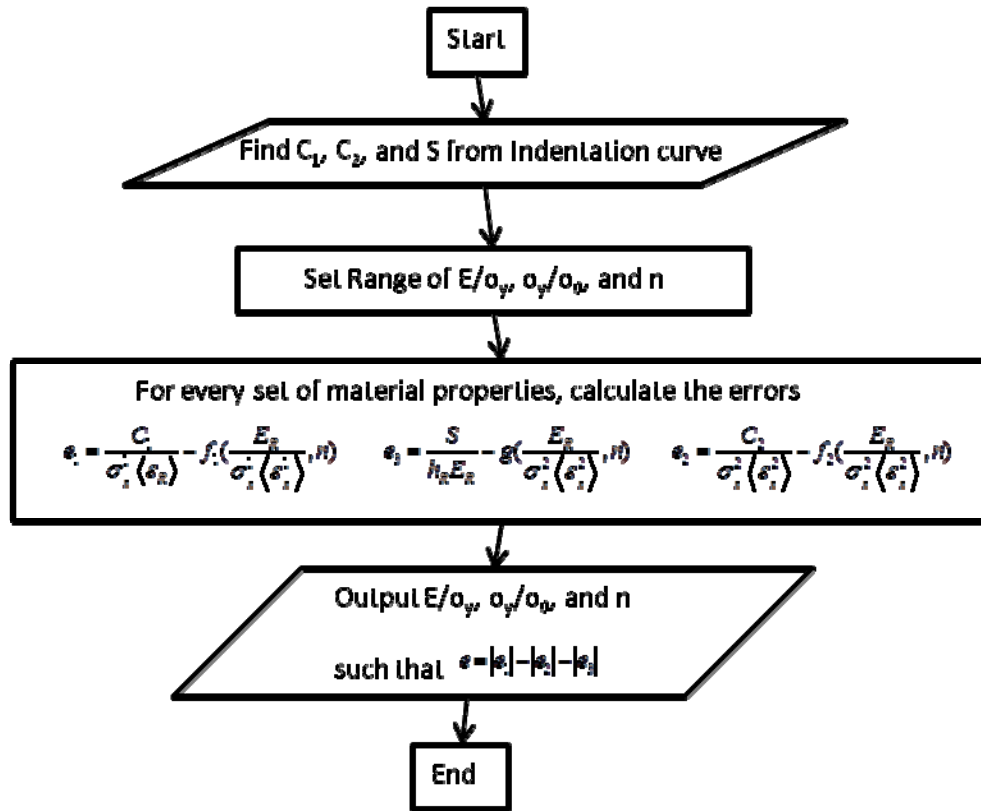


Figure 38: Flow Chart for Determining Material Properties

The output values from the analysis are listed in Figure 39. In Table 3, the results for each of the materials are compared to those found by Zhao, *et al.* in their model.

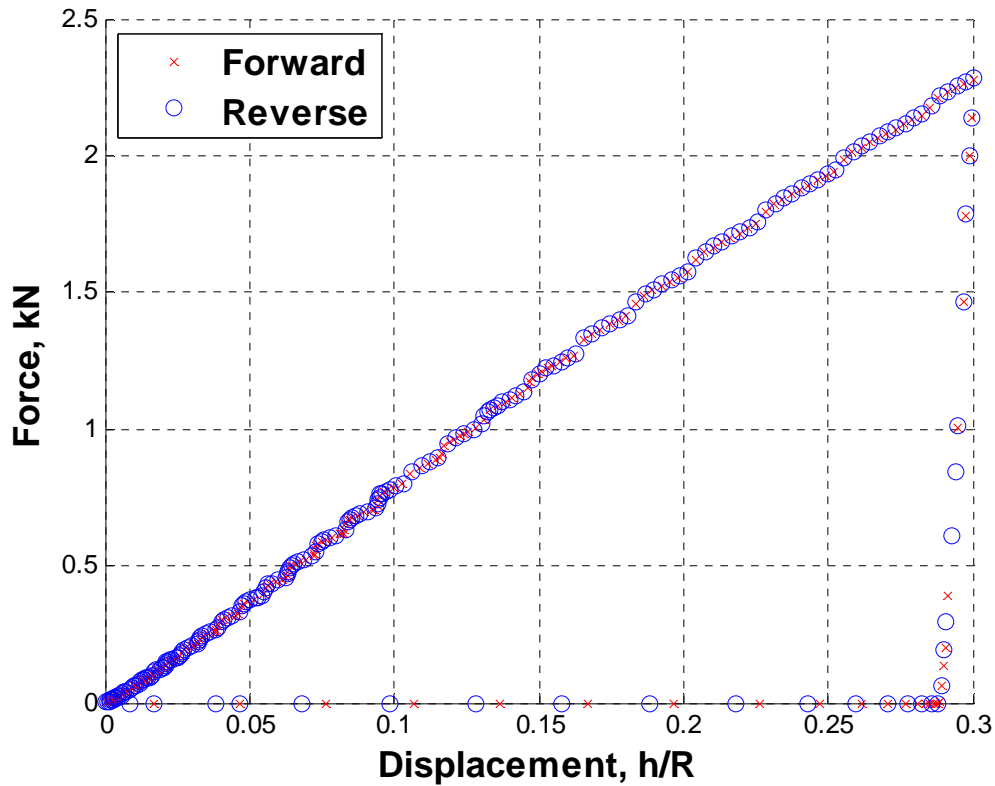


Figure 39: Comparison of Force Indentation for Forward and Reverse Analysis

Table 3: Zhao Algorithm Output Comparison with Symbolic Solver

	E (GPa)	σ_y (MPa)	n
Input Parameter	210	400	0.127
Zhao Output	206	402	0.125
Percent Difference	2%	1%	2%
Dauby Output	247	396	0.125
Percent Difference	18%	1%	2%

Although, he was only off by 2% for this material, Zhao reported values with consistently 10% error of for each value. The first analysis of the present study had slightly higher errors for E, consistently 8 or so % higher than Zhao. One possible reason

for the difference could be the choice of a symbolic solver. During the analysis, in order to find the reference stress a nonlinear, explicit equation must be solved. The analysis was then repeated using a numerical solver to determine the reference stress. These results are shown in Table 4. The E value produced was more in line with input values with slight uptick in the yield stress and n value.

Table 4: Zhao Algorithm Output Comparison with Numerical Solver

	E (GPa)	σ_y (MPa)	n
Input Parameter	210	400	0.127
Zhao Output	206	402	0.125
Percent Difference	2%	1%	2%
Dauby Output	235	380	0.13
Percent Difference	12%	2%	5%

One potential application for this technique to biological tissues is for harder materials such bone. The hawkmoth exoskeleton would seem to be a possible candidate for this analysis. Since the approximate thickness of the exoskeleton is 30 μm [21], there would be limitations to the size of the indenter when setting up this experiment. In order to model a half space approximately 50 times the maximum depth of the indentation ($0.3R$), one would be limited to an indenter with a radius of approximately 2 μm . Any larger and substrate effects would be at risk of influencing results.

5.3.2 Flat Punch to Elastic Medium

In this scenario, how the boundary affects the experiment conducted by Nayar *et al.* [13] was analyzed using the elastic finite element model. As mentioned previously, this experiment involved an 80 micron diameter cylindrical flat punch indenting porcine

sclera. The indentation chosen was only 4 μm deep, therefore, according to (2.11), the strain resulting from this experiment is approximately 0.1 and falls within the accepted region for elasticity. The linearity of this region could be verified by a hyperelastic finite element analysis; however, the only data that could be found for the sclera was elastic.

In their experiment, the sclera samples were cut into 1 cm squares with a thickness of approximately 1 to 1.2 mm. This would appear to be a large enough sample to remove effects of the boundary on the analysis. However, finite element model can help in ensuring that there is no discrepancy. For the purpose of this simulation, the sample was set to 1.2 mm (1200 μm) on each side to match the thickness of the real life sample.

First, the flat punch model was modified to simulate the scenario of the sclera experiment so that the geometry (40 μm radius indenter) and material properties ($E=30\text{kPa}$) are made to match. The mesh is varied and the force displacement curve and the stress field under the indenter are mapped in Figure 40 and Figure 41, respectively.

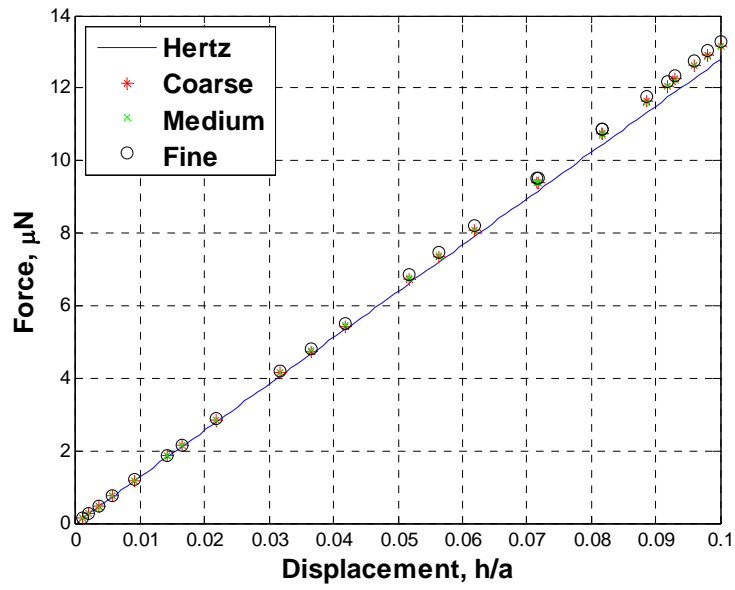


Figure 40: Mesh Refinement for Flat Punch using Force-Displacement Relation

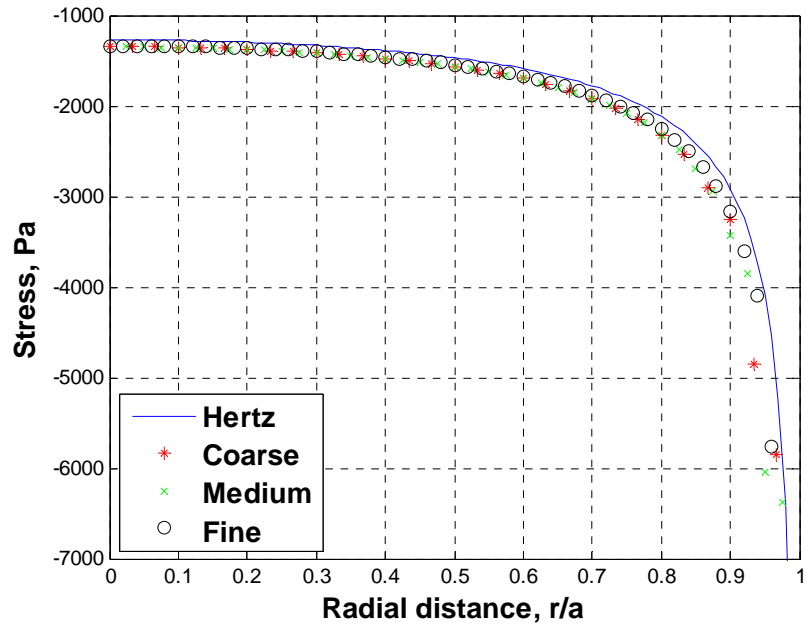


Figure 41: Mesh Refinement for Flat Punch using Stress-Radius Relation

The force-displacement curve produced stiffer results as the mesh became finer, however the stress field under the indenter more closely matched the analytic solution. The stress field is the primary means of measuring the boundary effects so the finer mesh was used as the model.

Next the boundary conditions were modified to have rollers on the left and right side of the sample as in Figure 42. This modification verifies that the 1200 by 1200 μm sample adequately represents an infinite half-space. Additionally, the sample was increased to 4800 by 4800 μm as a second check. These results are used for comparison as the width and depth of the sample are adjusted.

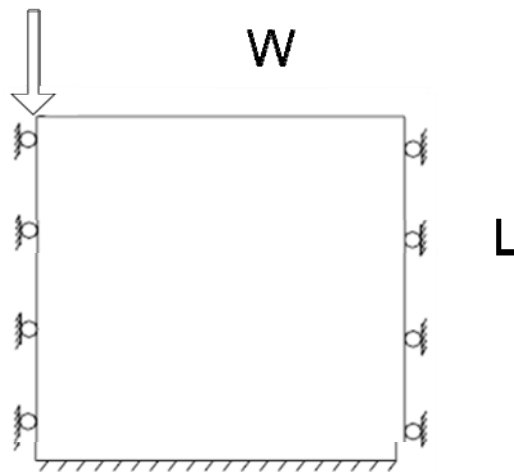


Figure 42: Model Boundary Conditions: Y-axis Symmetry (Left side, Right side) and Fixed (bottom)

As shown in Figure 21, Figure 22, and Figure 42, W represents the horizontal distance from the point of indentation to the vertical boundary and L represents the vertical distance from the surface of the sample to the bottom of the sample. The bottom is fixed, representing a hard surface underneath the sample. Typically the rule of thumb for

thickness of a sample is to maintain an indentation depth that is no more than 10-20% of the thickness of the sample. [34]

To analyze what effect the horizontal boundary distance has on the measurement of the elastic modulus, the simulation was run using W values of $600\ \mu\text{m}$ and $300\ \mu\text{m}$ and again with L values of $600\ \mu\text{m}$ and $300\ \mu\text{m}$. The stress underneath the indenter and the force-displacement relationship were plotted in Figure 43 and Figure 44, respectively, for varying W values. The stress and force-displacement relationship for varying L values are shown in Figure 45 and Figure 46.

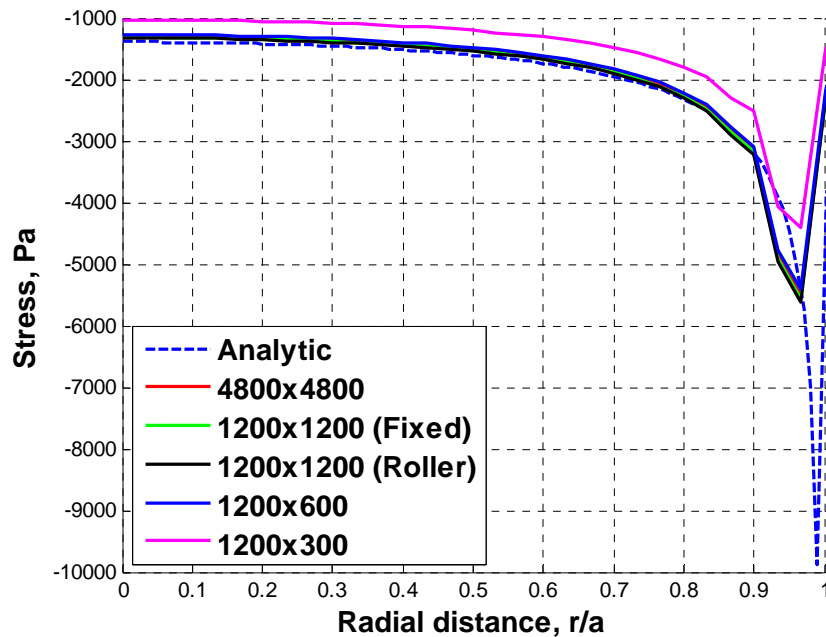


Figure 43: Comparison of the stress along the bottom of a flat punch indenting several sample sizes

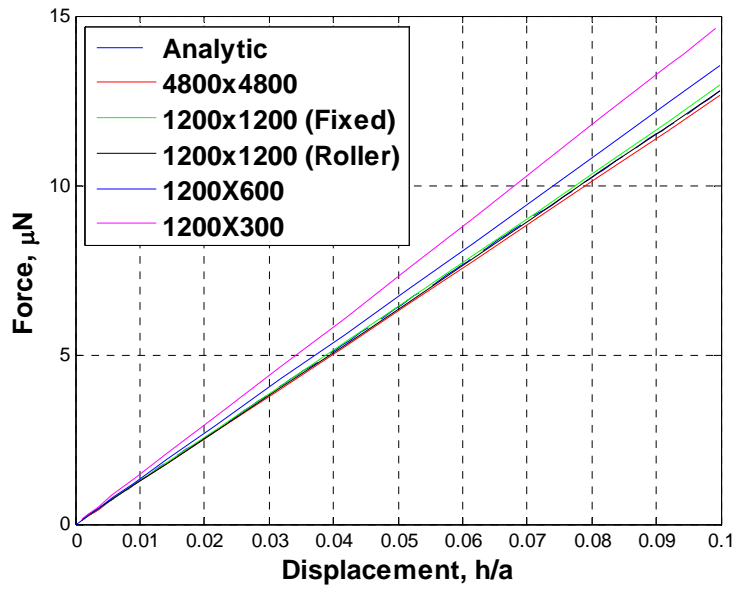


Figure 44: Comparison of the force-displacement relationship for a flat punch indenting several sample sizes with varying horizontal distance (W)

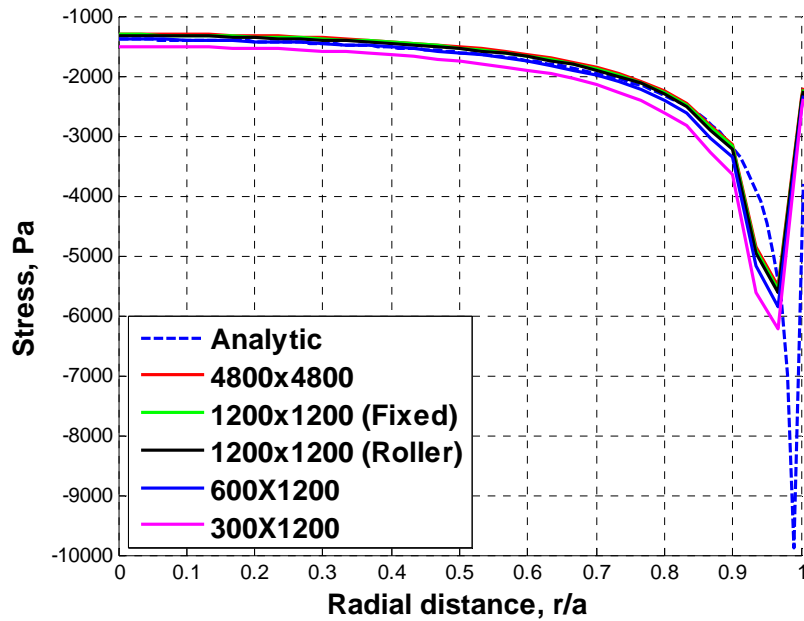


Figure 45: Comparison of the stress along the bottom of a flat punch indenting several sample sizes

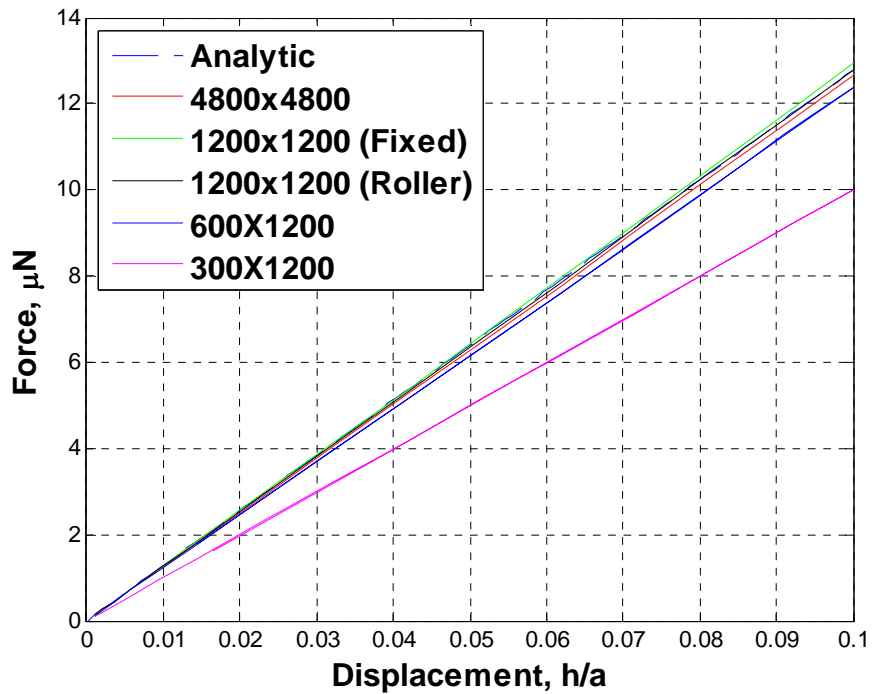


Figure 46: Comparison of the force-displacement relationship for a flat punch indenting several sample sizes with varying vertical distance (L)

In Table 5, the effects of the smallest boundary condition are compared to the large sample and the Hertzian solution. The Hertzian solution is treated as truth for the percent error calculations. As can be seen from Table 5, the smaller boundary can have a large effect on the calculation of the elastic modulus. Errors were most noticeable for the thickness of the sample at 21.9%. This shows that for low modulus materials, the thickness of the sample should be more carefully monitored than for a similarly sized stiffer material.

Table 5: Summary of effects of E from the smallest sample boundary length compared to Hertzian analytic solution and a large sample

	σ (kPa) (Midpoint)	% Error	E (kPa)	% Error
Hertz	-1.3929	0.0%	30.0	0.0%
1200x1200	-1.3144	5.6%	30.1	0.4%
1200x300	-1.5065	8.2%	34.2	14.1%
300x1200	-1.0368	25.6%	23.4	21.9%

5.3.3 Spherical Indenter into Hyperelastic Medium

In this scenario, a rigid spherical indenter is indented into a hyperelastic half-space. Up until now, the coefficient of friction between the sample and the indenter has been assumed to be frictionless. For the vast majority of indentation experiments the effect of friction is assumed to be negligible. According to Shacham S, *et al.*, [35] for muscle tissues in contact with bone the coefficient of friction could be as high as 0.36. This is not a one-to-one relationship with a diamond or sapphire indenter in contact with a tissue, however, the relationship this factor has for a hyperelastic material is worth investigating.

The model begins with the frictionless scenario established previously. The mesh from section 5.3.1 that was verified using the elastic space is used for this analysis as well. The indenter size is adjusted to 5 μm and the sample size was correspondingly decreased to 125 μm square. Per Lin *et al.* experiment, the indentation is 1 μm .

In order to gauge the effects of friction on this model, the coefficient was increased to 0.1, 0.2 and 0.3. The indentation stress field is shown in Figure 47.

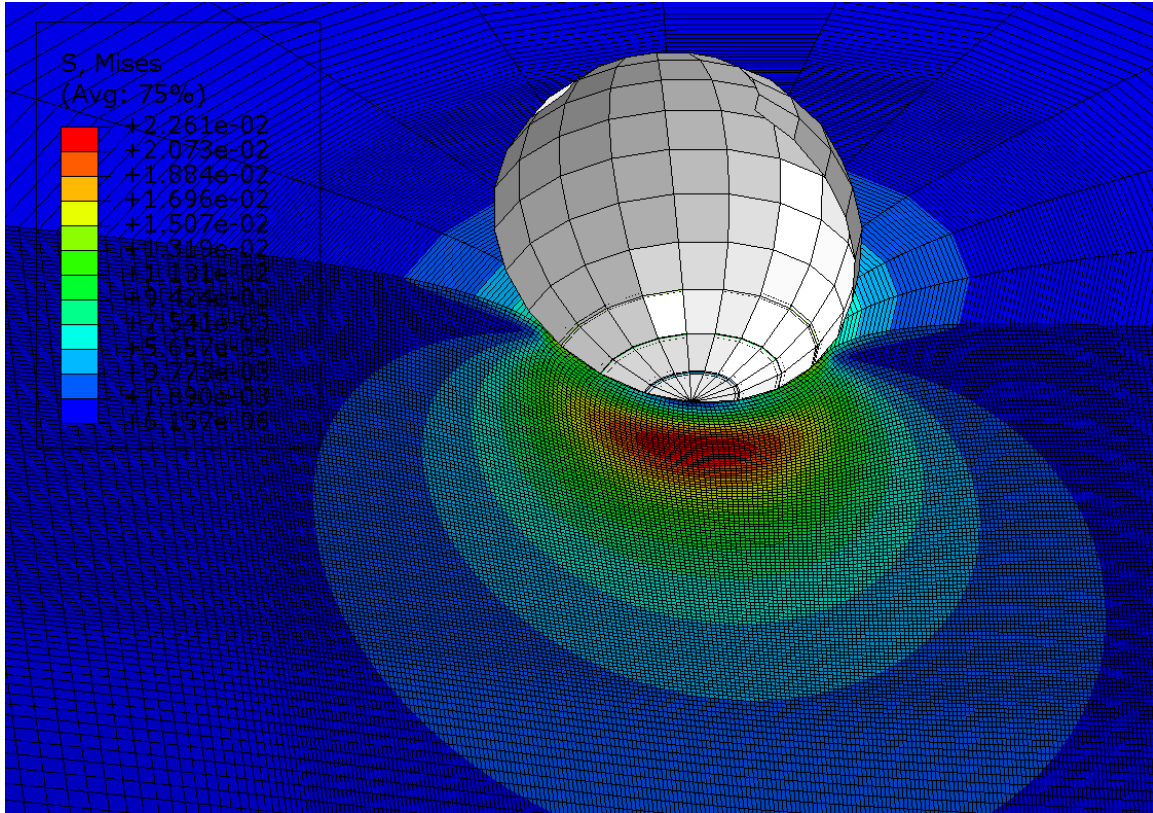


Figure 47: Stress Field for Hyperelastic Material

The effects on the force indentation curve are shown in Figure 48. The elastic force-displacement model and the hertz analytic solution were also plotted for comparison.

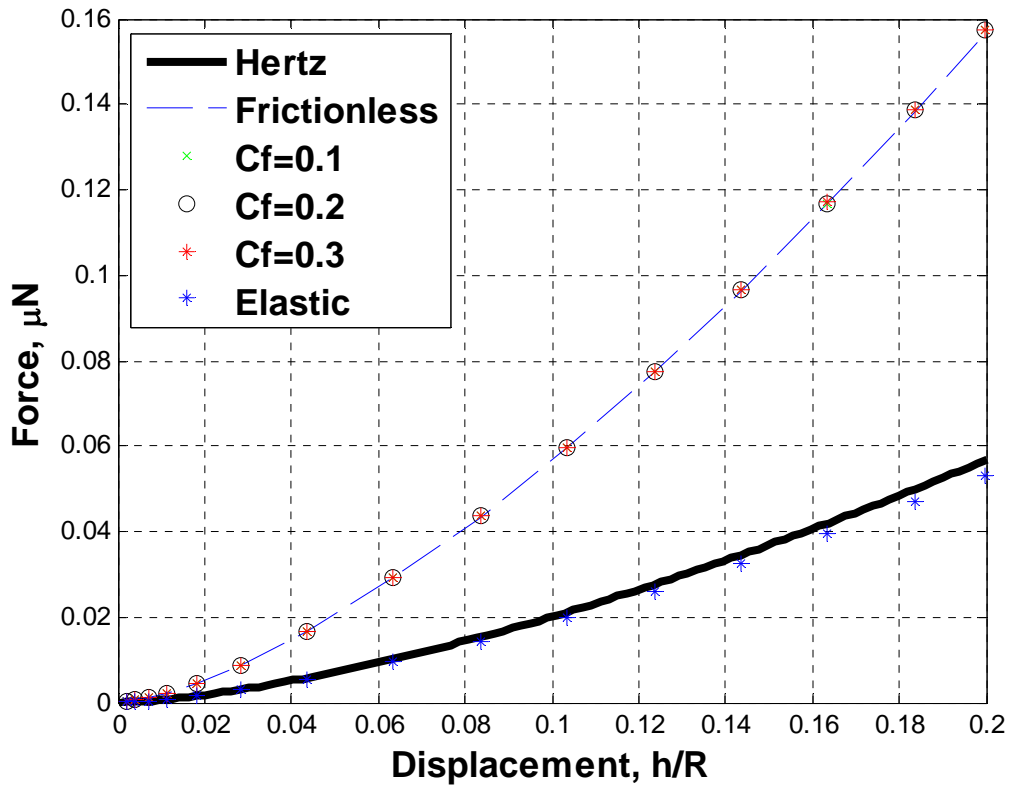


Figure 48: Friction Comparison Force Indentation Curve ($h=1\mu m$)

As can be seen from Figure 48, friction had no effect on the force-displacement relation whatsoever. In Figure 49, the contact area is compared for the differing friction values as well. Again, there is no change. The frictionless assumption is valid for this indentation depth.

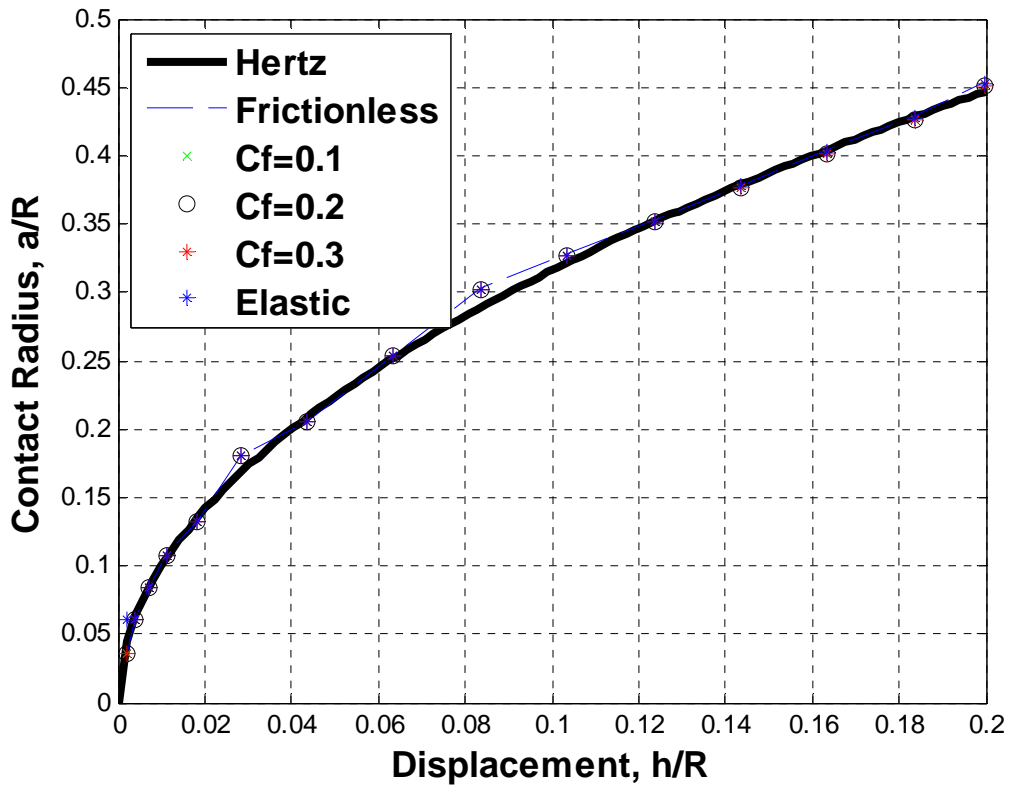


Figure 49: Friction Comparison Contact Radius ($h=1\mu\text{m}$)

In order to see how the material behaves outside of the indentation depth made by Lin, *et al.*, the scenario was conducted again for an indentation of $4\mu\text{m}$. As can be seen in Figure 50 and Figure 51, there is some minor variation in the force indentation and the contact radius from the finite element simulation. It appears that the frictionless assumption becomes marginally less valid as the indentation depth increases.

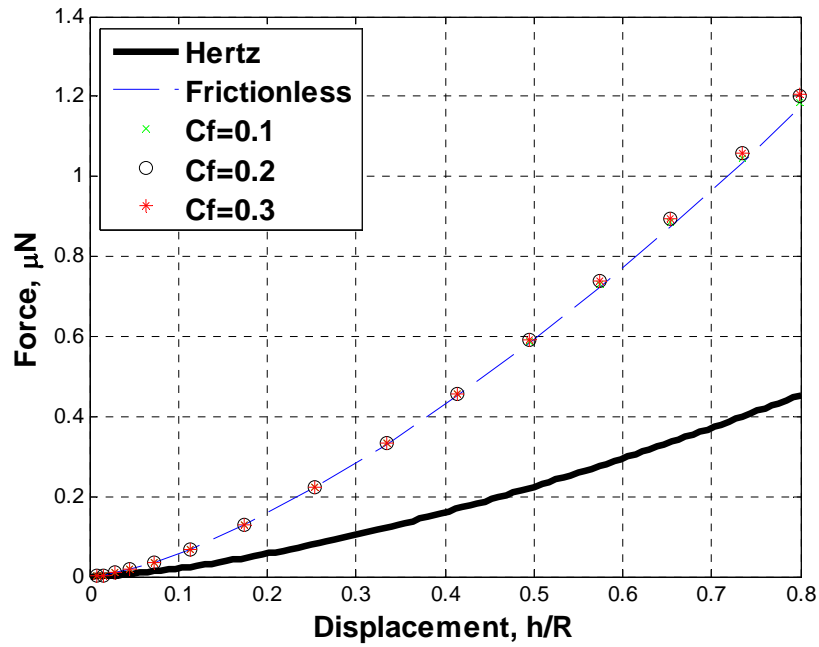


Figure 50: Friction Comparison Force Indentation ($h=4\mu\text{m}$)

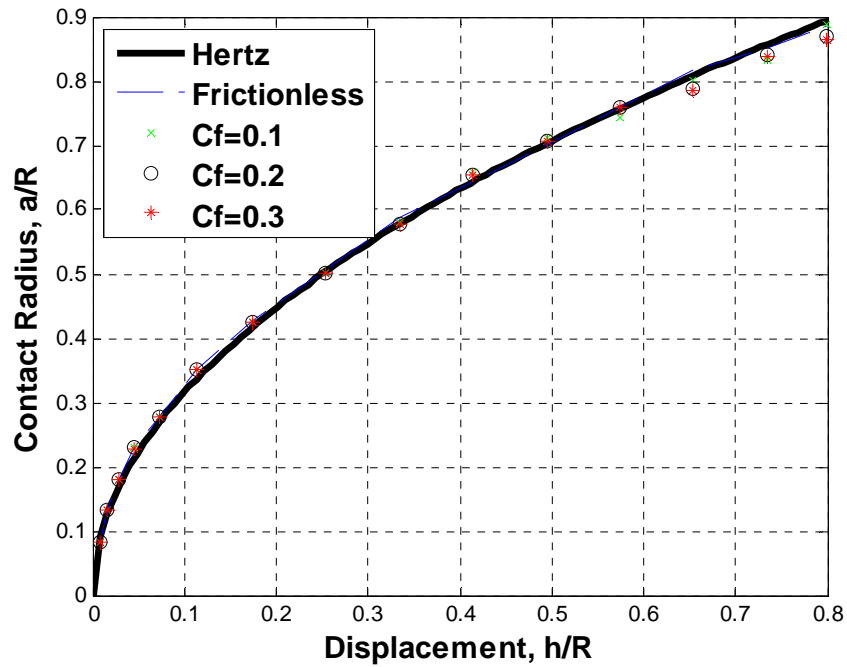


Figure 51: Friction Comparison Contact Radius ($h=4\mu\text{m}$)

5.3.4 Extraction of Ogden Parameters from Force-Indentation Curve

The spherical indentation model described in section 5.3.3 can also be used to extract parameters from experimental data. As in section 5.3.1, experimental data was not available so the finite element model was used to produce simulated data. Initial shear modulus (μ_0) and curvature parameters (α) were input in the ABAQUS model. The parameters chosen were: $\mu_0 = 7.89\text{kPa}$ and $\alpha = 20$. The radius of the spherical indenter was set at $R = 120\ \mu\text{m}$ and size of the sample was set at 50 times the radius. The indentation depth was set at $0.4R$, or $48\ \mu\text{m}$. The resulting stress-strain curve can be seen in Figure 52 and along with the solution for the linear elastic medium shown in blue for comparison. The nonlinearity of the solution is apparent.

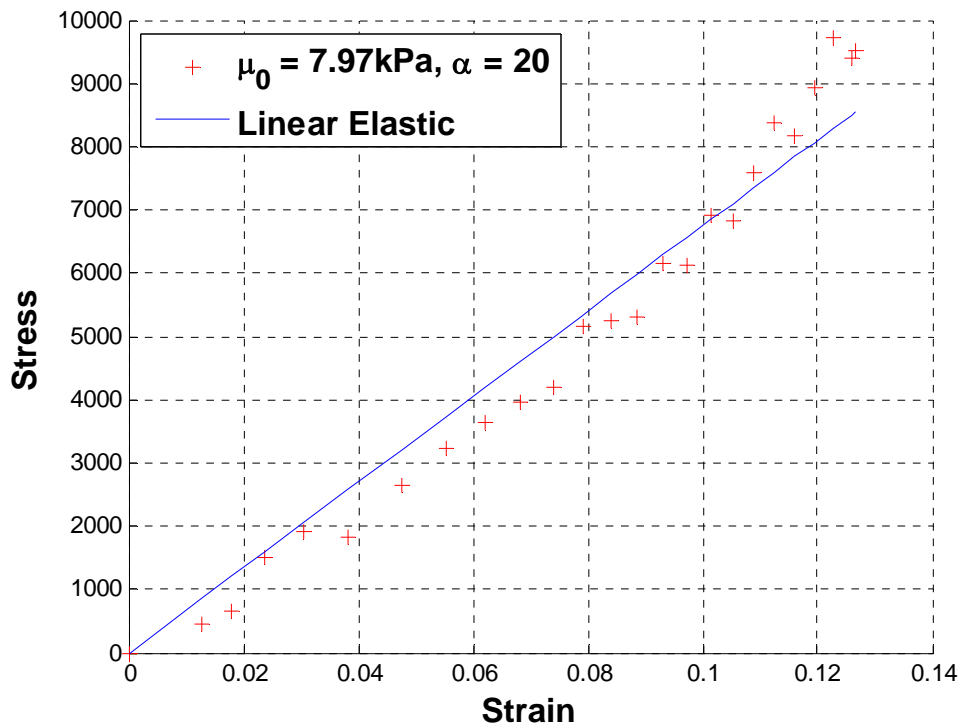


Figure 52: Representative stress and strain from a spherical indenter into a hyperelastic medium simulation compared against an elastic medium

In order to determine the coefficients of this simulated data, the force-displacement relationship in equation (2.20) presented by Lin, *et al.* was fitted to the data using a nonlinear-least squares data fit. The code for this extraction is in Appendix B.

$$(2.20) \quad P = \frac{B\pi a^2}{\alpha} \left[\left(1 - 0.2 \frac{a}{R}\right)^{-\alpha/2-1} - \left(1 - 0.2 \frac{a}{R}\right)^{\alpha-1} \right]$$

Equation (2.20) was rearranged to express the stress-strain relationship using the equations $\sigma^* = P / \pi a^2$ and $\varepsilon^* = 0.2 * a / R$ to the form:

$$(5.1) \quad \sigma^* = \frac{B}{\alpha} \left[(1 - \varepsilon^*)^{-\alpha/2-1} - (1 - \varepsilon^*)^{\alpha-1} \right]$$

The fit to this equation is shown in Figure 53.

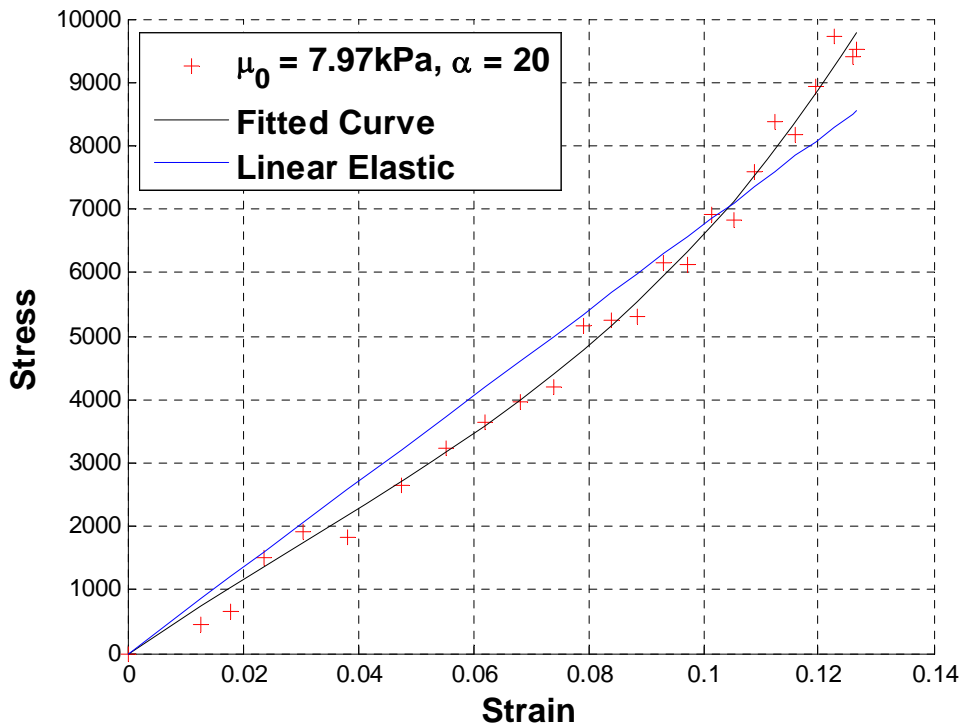


Figure 53: Representative stress and strain from a spherical indenter into a hyperelastic medium simulation with a curve fit to extract Ogden parameters

The parameters as determined by the least squares method are: $\mu_0 = 7.369$ kPa and $\alpha = 23.2$. This represents a 7.55% and 16.10% percent difference from the input μ_0 and α , respectively. The new parameters were input into the finite element model to compare against the initial simulation. The results are shown in Figure 54 and match well.

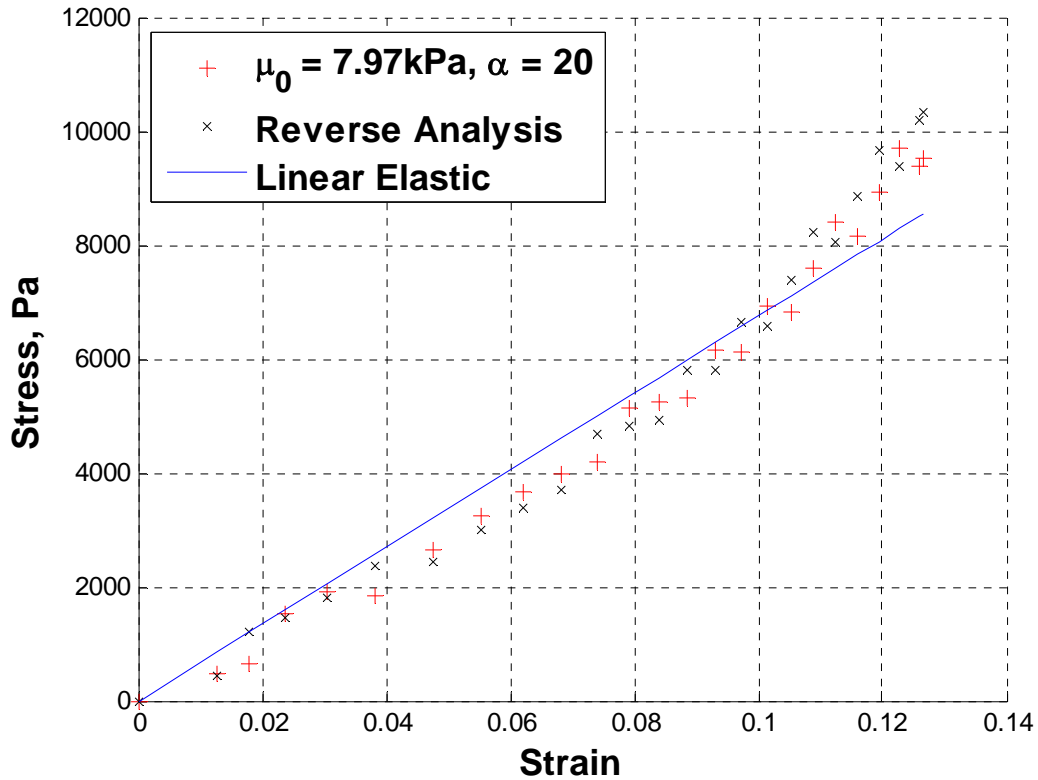


Figure 54; Comparison of the simulation results from initial material parameters and material parameters from a curve fit

5.4 Results of Nanoindenter Experiment

No data were able to be gathered from the nanoindentation experimentation. For each indentation test, the indenter head would approach the surface and push through. However, the indenter instrumentation would be unable to record that the surface had

made contact. It soon became apparent the primary reason was that the load vs. displacement slope for the material was too low. The surface stiffness of the sample was too low to escape the noise of the machine.

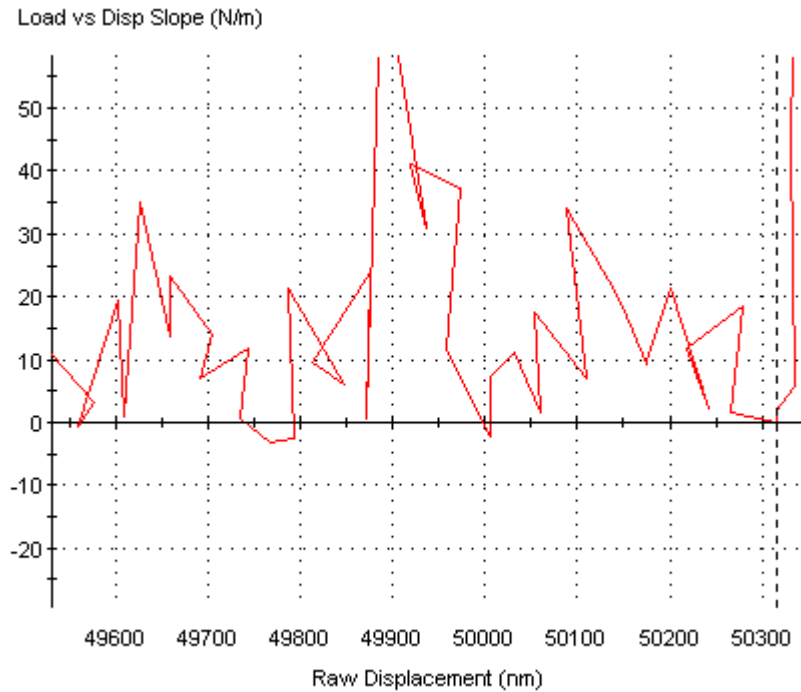


Figure 55: Noise from Load vs Displacement Channel for G200 during Surface Find

To investigate whether this was the cause, the elastic Hertz contact equations were revisited. Since the surface contact involves the initial depth of indentation, the material can be assumed to be elastic without the hyperelastic effects dominating. Considering first the force-displacement equation (reprinted from Chapter 2):

$$(2.5) \quad P = \frac{4}{3} E_R R^{\frac{1}{2}} h^{\frac{3}{2}}$$

And taking the derivative with respect to depth yields

$$(5.2) \quad \frac{\partial P}{\partial h} = 2E_R R^{\frac{1}{2}} h^{\frac{1}{2}}$$

Substituting in the definition of reduced modulus, $E_R = E / (1-\nu^2)$ and $\nu=0.5$

(incompressible assumption) gives;

$$(5.3) \quad \frac{\partial P}{\partial h} = \frac{8}{3} ER^{\frac{1}{2}} h^{\frac{1}{2}}$$

This function was plotted by varying the elastic modulus while holding the indenter radius constant for select values. This can be seen in Figure 56. Additionally, from Figure 55, the approximate noise level for the Agilent G200 was approximately 10 N/m and also was plotted as the thick horizontal line.

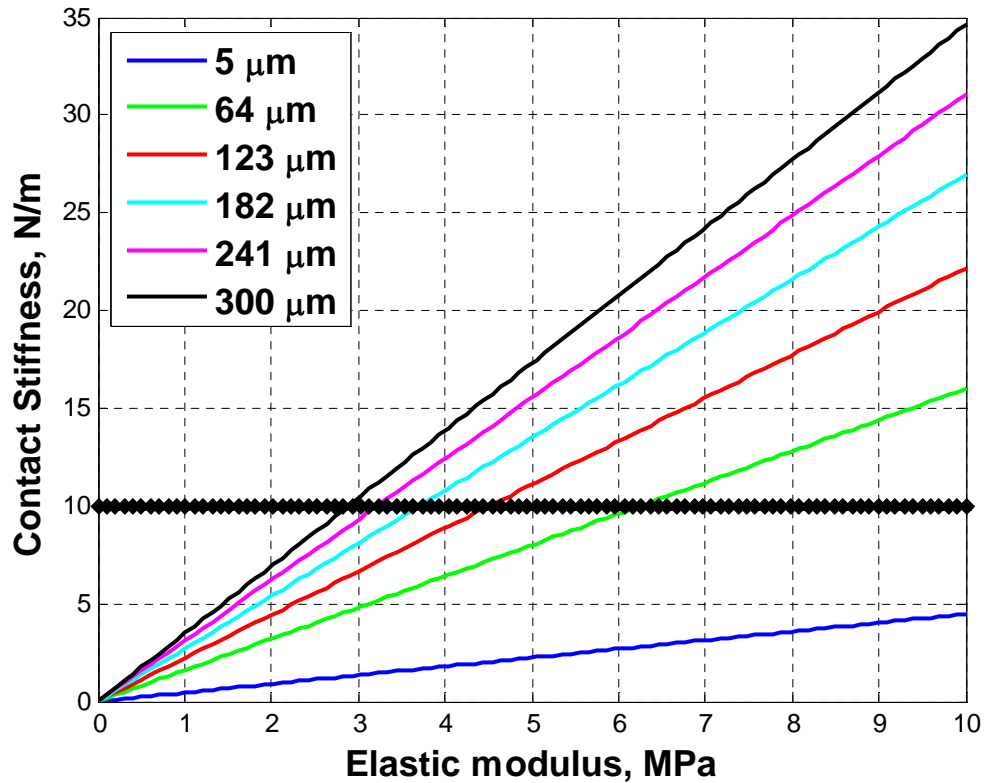


Figure 56: Load/Displacement Slope vs. Elastic Modulus for Varied Indenter Radius with noise level shown as black horizontal line.

From the graph, the smallest modulus that would be able to be measured for this range of indenter sizes would be approximately 3 to 6 MPa. This is approximately 100 times the values for soft tissue found in the literature.

Returning to the hyperelastic spherical indentation model from section 5.3.4, the force indentation relationship can be seen in Figure 57. The initial slope for the first $0.5\mu\text{m}$ of the indentation is approximately 0.3. This shows that the soft material used in the Lin, *et al.* experiment would not be able to be measured with the G200 nanoindenter.

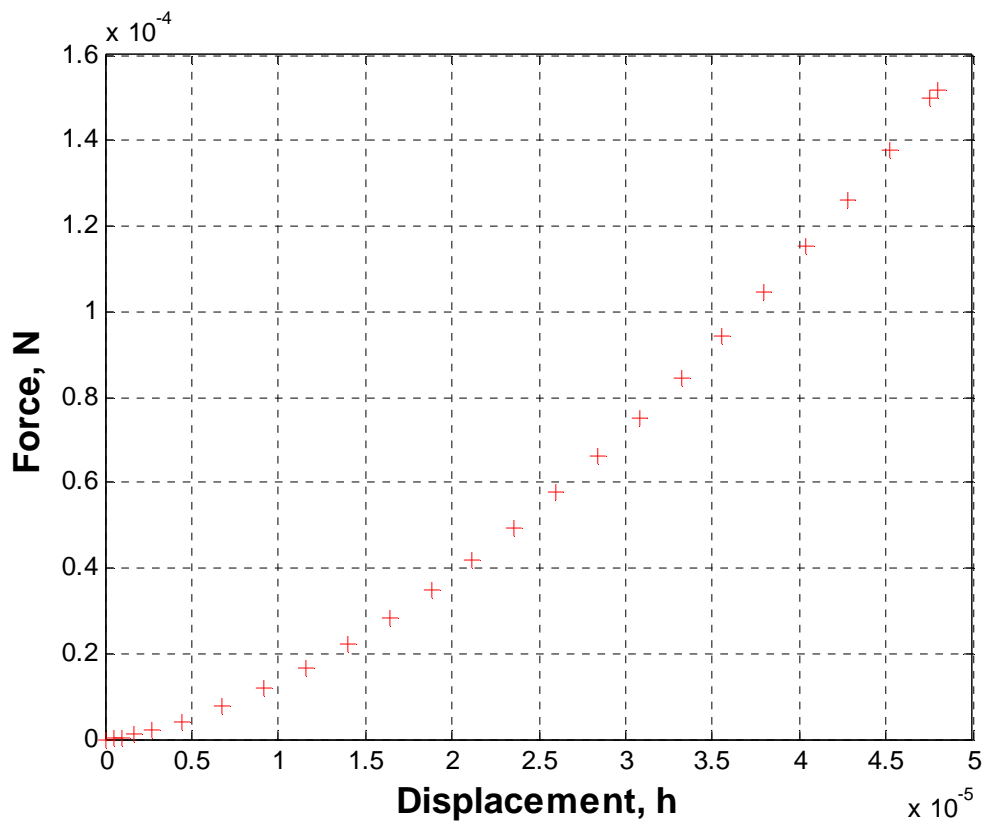


Figure 57: Force-displacement relationship for spherical indenting a hyperelastic medium with 1st order Ogden potential parameters $\mu_0=7.97\text{kPa}$ and $\alpha=20$

Improvements to the equipment for this test are needed. One possibility is to use the DCM II Indentation Head Option for the Agilent G200. This option provides greater resolution for the indentations and sensitivity in the analysis with load resolution of 3 nN. However, this option was not functioning for the test system and future researchers would need to have it replaced.

The more likely solution to this problem is to use AFM instrumentation to conduct the experiment. AFM instruments have a much lower force and displacement resolution. Spherical tips are available for AFM machines as well, so the finite element development for the indentation experiments would still be applicable, only on a smaller scale.

5.5 Results of Tensile Experiment

The results of the tensile experimental investigation are presented in this section. As mentioned at the end of Chapter 4, the clamps for the T150 broke before the completion of the planned tests could be completed. A summary of those tests that were able to be completed is given in Table 6. It should be noted that Test 1 was aborted after a strain of only approximately 0.03 due to a disturbance to the test fixture. The results have also been presented in Figure 58. The elastic modulus was extracted by applying a linear best fit line to the portion of data. The overall modulus was calculated by applying linear regression to the entire data set (only the linear portions of the data were used).

Table 6: Results for 4 Tests of Initial Modulus Elastic for Hawkmoth Muscle

Test	E, kPa	A0,mm ²	l0, mm
Test 1	802.17	1.5394	1.6
Test 2	39.80	1.131	1.6

Test 3	998.32	1.3273	2
Test 4	801.92	1.5394	2

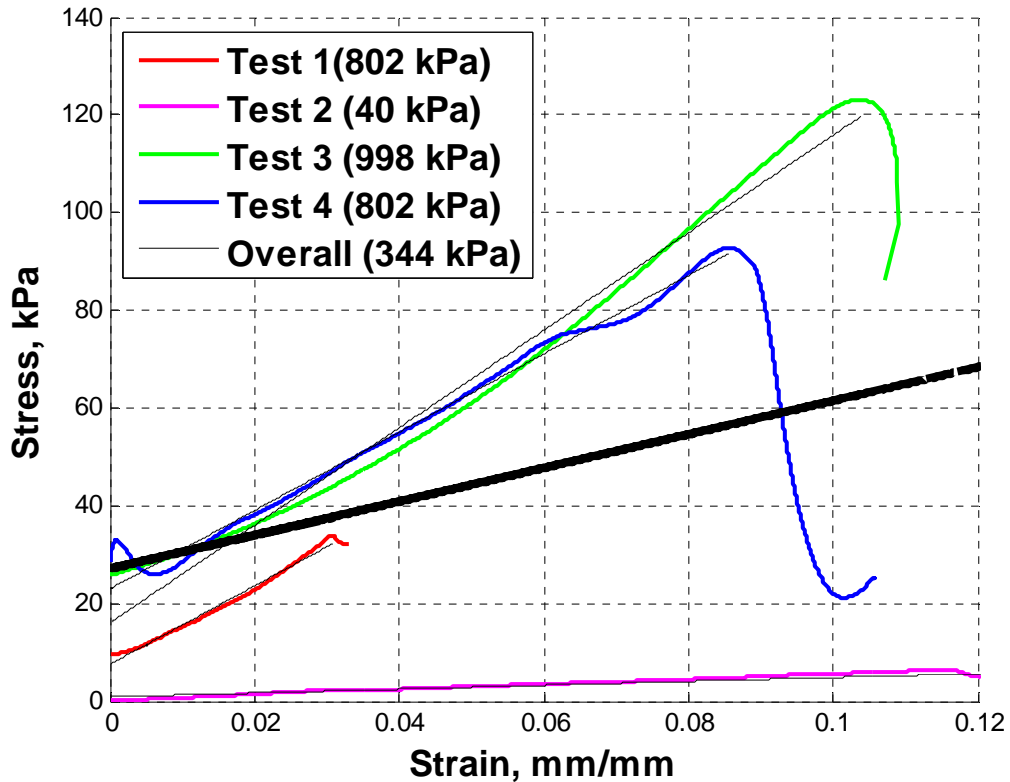


Figure 58: Stress-Strain Diagram for all 4 tests of Hawkmoth DLM motor unit and their individual linear regression fits and the overall regression fit.

As can be seen from the Table 6 and from Figure 58, 3 of the tests (1, 3, and 4) had reasonably agreeable values of elastic modulus in the high 100s of kPa. The other test (2) is approximately 20 times smaller than the other three tests. Looking at Table 7, overall average of the slopes and the standard deviation (SD) of the slopes is reported. The overall regression uses all the points in the sample If Test 2 (T2) is removed because

it falls outside of standard deviation of the remaining tests, the overall elastic modulus becomes 982 kPa. These results are plotted in Figure 59.

Table 7: Summary Statistics of the 4 Uniaxial Tension Tests

Test	E, kPa	A0,mm ²	l0, mm
Overall Average	660.56	1.38	1.80
Overall SD	424.05	0.20	0.23
Overall Regression	343.72		
Average w/o T2	867.47	1.47	1.87
SD without T2	113.32	0.12	0.23
Regression w/o T2	982.3		

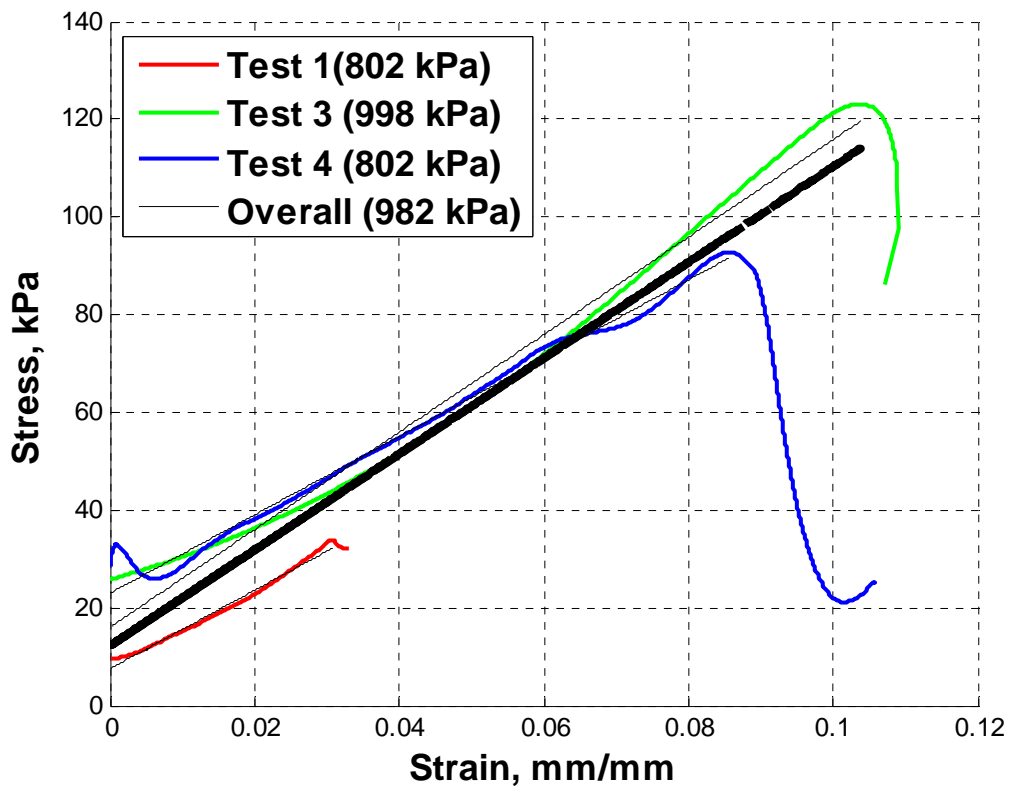


Figure 59: Hawkmoth DLM Stress-strain curve with Outlier Removed

However, the Test 2 outlier may not necessarily have been an invalid test. Most importantly, the small sample size precludes making too many inferences about which test is valid and which is not. Additionally, the level of hydration of the samples can cause variability in their elastic properties. A desiccation test was devised to determine how much weight the muscles lost when exposed to the air. A single muscle unit was extracted as described in Section 4.2. It was patted dry to remove excess moisture and placed on a scale and weighed to the nearest milligram. The sample was reweighed at regular intervals for a period of 16 minutes. The results of this experiment can be seen in Figure 60. The muscle unit lost over half its weight in only a period of 16 minutes. On average the tests lasted approximately 6 minutes there for approximately 12-15% of the muscles water weight could have evaporated during that time.

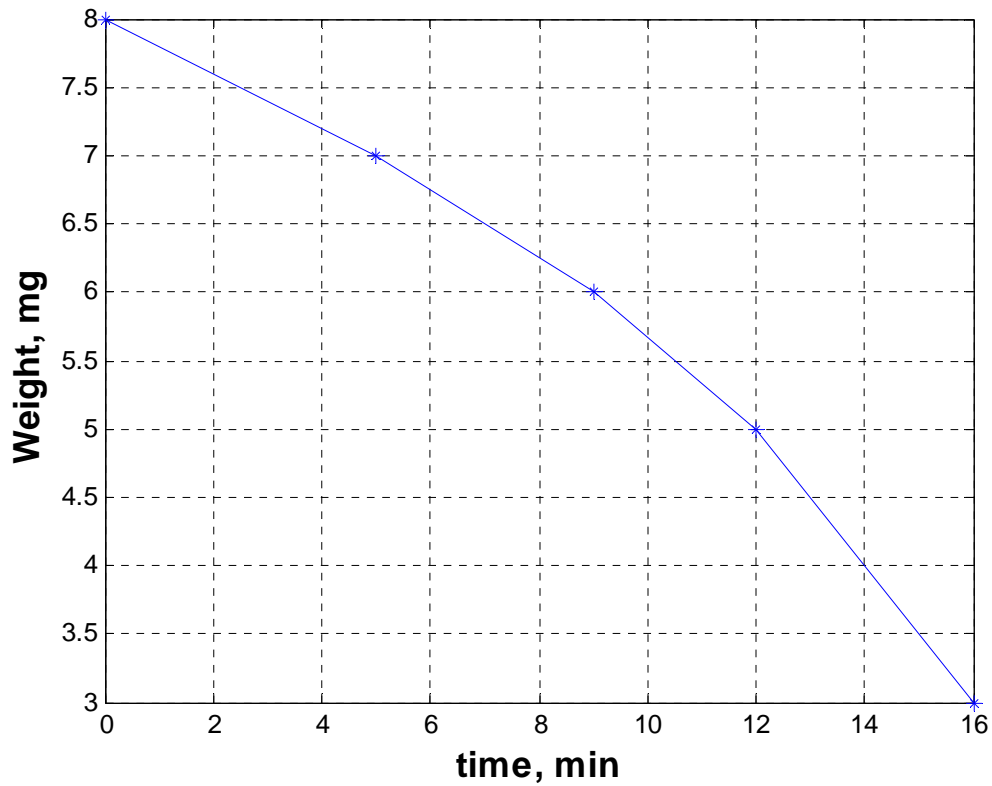


Figure 60: Chart of desiccation of Hawkmoth muscle over time while exposed to air

Qualitatively, as the samples become less hydrated, they become much harder to the touch and would most likely have a higher value for E. It is possible that the other 3 tests lost more moisture than test 2. Additionally, this idea that the other three lost moisture looks like more of a possibility when compared to the results of other tensile tests of muscles as shown in Table 8.

Table 8: Summary Comparison with prior Muscle Tensile Experiments

Study	Modulus (kPa)	Animal
Gras, <i>et al.</i> [16]	111	Human
Dorfman <i>et al.</i> [18]	2.34	Caterpillar
Collinsworth, <i>et al.</i> [37]	45.6	Rabbit
Fung [6]	20-160	Rabbit
Dauby	334	Moth

Better ways of keeping the sample hydrated need to be used for this type of test. The sample dried out prior to the conclusion of the test. As mentioned previously, the hydration method used was similar to that used by Gras, *et al.* Their study was able to hydrate only at certain points in the test because their samples were much larger. The smaller surface area to volume ratio of their samples did not allow for as much desiccation. A better way of testing the samples would be to keep them completely submerged in the saline solution.

The small length of the sample with respect to the diameter can also affect the results. In order to estimate what this effect might be, a new finite element code was developed. This model was again axisymmetric, with element type CA4XR. The first 1.5 mm of the sample was fixed along the edges of one end while the displacement was applied to the edges of the other end. This simulates the glue holding the ends of the sample. The mesh was refined near these boundary points. The mesh and boundary conditions for this model can be seen in Figure 61. The diameter of each sample was fixed at 2mm, which is approximately the diameter of the muscle unit. Four different gauge lengths were analyzed: 2, 4, 7, and 10 mm.

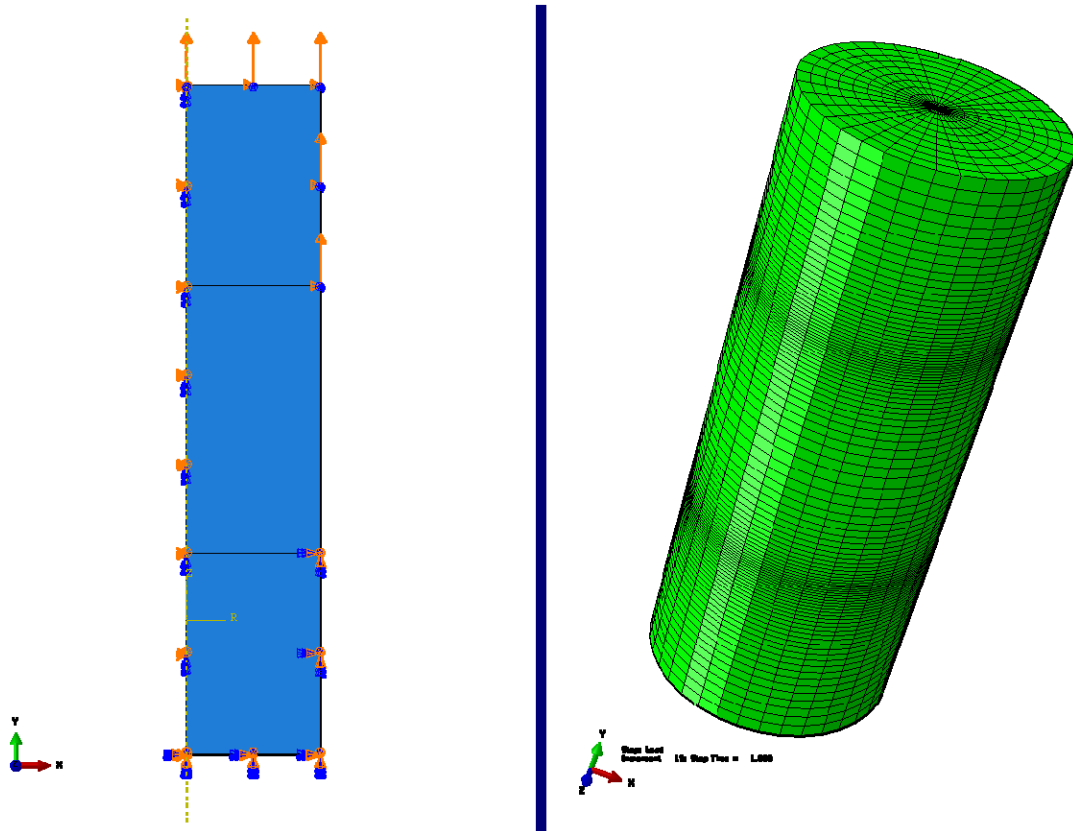


Figure 61: Boundary Conditions (left) and Mesh (right) for Uniaxial Tension Model (2mm gauge length shown)

In the simulations in Figure 62, the bottom right figure has a gauge length of 2mm which is approximately the situation in this experiment. For a large strain of 0.5, there is a much larger stress variation across the midsection of the sample. The gauge length is increased going clockwise. As can be seen, the further away from the boundary conditions, the more uniform the stress field in the sample.

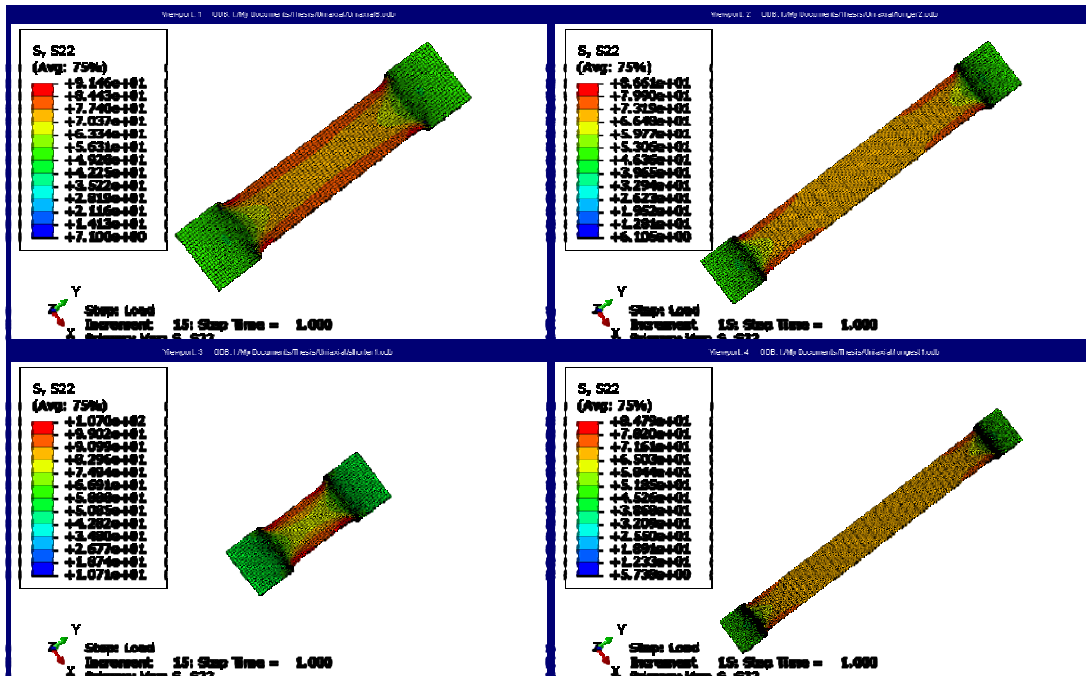


Figure 62: Stress cross sections for all tests to 50% strain. (Clockwise from bottom left: 2mm gauge length, 4 mm gauge length, 7 mm gauge length, and 10 mm gauge length.)

New ways of securing the sample are recommended by this report to be investigated. One possible way is to dissect the moth in a way to keep the attachment points of the exoskeleton intact. This would keep the full 10mm length of the muscle to be used as the gauge length. Also the boundary conditions would remain intact, thereby better simulating the natural environment. Better dissecting skills would be required to accomplish this new method.

5.6 Summary

Three finite element models were developed with possible applications to biological tissue and possible applications to the hawkmoth. One model determined the

elastic-plastic properties of a wide range of materials from one single spherical indentation. The second examined the boundary effects of the experiment with porcine sclera. The third examined the effect of coefficient of friction on a hyperelastic material.

The experimentation portion of the analysis returned a mixed bag of results. The nanoindentation experiment was unable to gather any data, although an upper bound was found on the indentation modulus of a material able to be characterized by the Agilent G200 Nanoindenter with a spherical tip. The tensile testing was able to gather data on the longitudinal modulus of the hawkmoth muscle. Compared to literature, the modulus was high most likely due to desiccation of the sample on the test device.

VI. Conclusions and Recommendations

6.1 Chapter Overview

In this chapter the conclusions that were obtained as a result of this research are outlined. Additionally, recommendations for future research are discussed. A summary of the study concludes the report.

6.2 Conclusions of Research

A finite element model was developed to analyze the elastic, power law-hardening properties of a wide range of material properties. The values reported from the analysis differed from the actual values by approximately 18%. This was slightly higher than the reported values from Zhao, *et al.*

The second finite element model was developed to analyze the boundary effects of an experiment analyzing the flat punch indentation of the material. It showed that the sample Nayer, *et al.* used was more than satisfactory for conducting the experiment.

Additionally it was shown that reducing the horizontal boundary to 300 μm could cause as much as a 23% error in the evaluation of the elastic modulus. The third model looked in the experiment by Lin, *et al.* to see what effects friction may have had on the analysis. For the indentation depth in the Lin study, friction would have had little to no impact on the results. Had the choice of indentation been deeper, a more pronounced effect could have been seen.

The experimental nanoindentation experiment was unable to gather data due to the limitations in the instrument in measuring a material with as low a modulus of elasticity as the hawkmoth. An upper bound on the modulus was established of approximately 3 MPa. This is consistent with literature values of modulus in the range of 1-50 kPa for soft tissues from other experimentation.

The uniaxial tension test was able to map the stress strain curve for strains up to 10%. Reported initial modulus of elasticity values were 343 kPa although only three experiments and one partial experiment were able to be conducted before the test fixture broke. Additional concerns for the testing methodology are centered on the dehydration of the samples during testing. This loss of water most likely had an increase in the stiffness of the samples and larger values for modulus. An additional concern for the test involves the small gauge length with respect to size of the specimen. Finite element models show probable uneven stress values throughout the specimen.

6.3 Recommendations for Future Research

The algorithm developed for the elastic-plastic model could be applied to a variety of materials. However, in relation to the problem of the material properties of the

hawkmoth, it could be used to determine the entire stress strain curve if instrumentation could be found with an indenter of radius small enough to go $0.3R$ into the material while not going into the substrate of the moth exoskeleton.

For future research involving indentation experiments with biological tissues, the Agilent G200 with the Standard XP Indentation Head should not be used. It should not be used because the load-displacement slope of the material is too low to be recorded by the machine. Other options such as an Atomic Force Microscope should be considered. Should the Nanoindentation experimentation data become available, the finite element models should be used to analyze and isolate the material properties.

Future research into the uniaxial tension test should account the hydration of the sample better. Applying saline solution directly prior to the test is not adequate and spraying the samples during test causes the test to be aborted. A horizontal testing apparatus with the sample completely submerged would be a preferable solution to the current testing system. This improved hydration would allow for preconditioning of the sample. Additionally, improved dissection technique could allow for a longer gauge length which would improve both handling of the samples and reduce boundary condition effects.

6.4 Summary

In summary, this study described a software package utilizing the commercial finite element suite ABAQUS to allow hyperelastic materials to be considered with the application towards soft biological tissue.

Two soft tissue models were developed and used to investigate boundary effects and coefficient of friction on two experiments conducted by outside researchers. The third model used a technique by Zhao, *et al.* to determine the elastic-plastic properties of

Another model successfully computed the material properties of an elastic-plastic material using only one spherical indentation. This model could be applied to the hawkmoth exoskeleton.

Two experiments were attempted. The first, a Nanoindentation experiment with the flight muscle of a hawkmoth was unsuccessful. The instrumentation was unable to measure the modulus of the material. The second experiment was a uniaxial tension test on the muscle. This experiment was able to obtain an initial elastic modulus of the material; however the results may skew high due to loss of moisture in the sample during the experiment.

Appendix A: Finite Element ABAQUS Input Files

Sphere (Elastic-Plastic)

```
*Heading
** Job name: zhao788 Model name: zhao-788mm
** Generated by: Abaqus/CAE 6.10-1
**Preprint, echo=NO, model=NO, history=NO, contact=NO
**
** PARTS
**
*Part, name=Sample
*End Part
**
*Part, name=Spherical
*End Part
**
** ASSEMBLY
**
*Assembly, name=Assembly
**
*Instance, name=Sample-1, part=Sample
          0., -40246.7628172297,          0.
*Node
    1,          1970.,          38276.7617
    2,          1970.,          40246.7617
    3,              0.,          40246.7617
    4,              0.,          38276.7617
    5,          39400.,          38276.7617
    6,          39400.,          40246.7617
etc
** INTERACTION PROPERTIES
**
*Surface Interaction, name=IntProp-1
1.,
*Friction, slip tolerance=0.005
0.,
*Surface Behavior, pressure-overclosure=HARD
**
** BOUNDARY CONDITIONS
**
** Name: Axi Type: Symmetry/Antisymmetry/Encastre
*Boundary
_PickedSet33, YASYMM
** Name: Bottom Type: Symmetry/Antisymmetry/Encastre
*Boundary
_PickedSet34, ENCASTRE
**
** INTERACTIONS
```

```

**
** Interaction: Int-1
** Contact Pair, interaction=IntProp-1, type=SURFACE TO
SURFACE
Sample-1."Sample top", Spherical."Sphere Surf"
** -----
-----
**
** STEP: Down
**
** Step, name=Down, nlgeom=YES, inc=10000
** Static
0.001, 1., 1e-06, 0.01
**
** BOUNDARY CONDITIONS
**
** Name: Down Type: Displacement/Rotation
** Boundary
_PickedSet21, 1, 1
_PickedSet21, 2, 2, -236.4
_PickedSet21, 6, 6
**
** OUTPUT REQUESTS
**
** Restart, write, frequency=0
**
** FIELD OUTPUT: F-Output-1
**
** Output, field, variable=PRESELECT
**
** HISTORY OUTPUT: Down
**
** Output, history
** Node Output, nset=Spherical."Sphere RP Set"
RF2, U2
** Node Print, nset=Spherical."Sphere RP Set", SUMMARY=NO
RF2, U2
** End Step
** -----
-----
**
** STEP: Up
**
** Step, name=Up, nlgeom=YES, inc=10000
** Static
0.001, 1., 1e-05, 0.05
**
** BOUNDARY CONDITIONS
**
** Name: Axi Type: Symmetry/Antisymmetry/Encastre

```

```

*Boundary, op=NEW
_PickedSet33, YASYMM
** Name: Bottom Type: Symmetry/Antisymmetry/Encastre
*Boundary, op=NEW
_PickedSet34, ENCASTRE
** Name: Down Type: Displacement/Rotation
*Boundary, op=NEW
** Name: Up Type: Displacement/Rotation
*Boundary, op=NEW
_PickedSet22, 1, 1
_PickedSet22, 2, 2, 236.4
_PickedSet22, 6, 6
**
** OUTPUT REQUESTS
**
*Restart, write, frequency=0
**
** FIELD OUTPUT: F-Output-1
**
*Output, field, variable=PRESELECT
**
** HISTORY OUTPUT: Down, Up
**
*Output, history
*Node Output, nset=Spherical."Sphere RP Set"
RF2, U2
*Node Print, nset=Spherical."Sphere RP Set", SUMMARY=NO
RF2, U2
*End Step

```

Flat Punch (Elastic)

```

*Heading
** Job name: FP4-refine100 Model name: Flat Punch-refine-
Copy
** Generated by: Abaqus/CAE 6.10-2
*Preprint, echo=NO, model=NO, history=NO, contact=NO
**
** PARTS
**
*Part, name=Cone
*End Part
**
*Part, name=Sample
*End Part
**
**
** ASSEMBLY
**
*Assembly, name=Assembly

```

```

**
*Instance, name=Cone-1, part=Cone
      0.,      -1500.,      0.
*Node
      1,      0.,      1500.,      0.
*Nset, nset=Cone-1-RefPt_, internal
1,
*Nset, nset="Cone RP Set"
      1,
*Surface, type=SEGMENTS, name="Cone surf"
START,      40.,      1580.
      LINE,      40.,      1501.
      CIRCL,      39.,      1500.,      39.,
1501.
      LINE,      0.,      1500.
*Rigid Body, ref node=Cone-1-RefPt_, analytical
surface="Cone surf"
*End Instance

```

```

**
*Instance, name=Sample-1, part=Sample
      0., -3846.76281722965,      0.
*Node
      1,      80.,      3766.7627
      2,      80.,      3846.7627
      3,      0.,      3846.7627
      4,      0.,      3766.7627
      5,      800.,      3766.7627
      6,      800.,      3846.7627
      7,      80.,      3046.7627
      8,      0.,      3046.7627
      9,      800.,      3046.7627

```

More nodes, etc

```

203, 204, 205, 206, 207
*Elset, elset=surface_set, instance=Sample-1, generate
      100, 10000,      100
*End Assembly
**
** MATERIALS
**
*Material, name=Sample
*Density
      2.65e-15,70.
*Elastic
      0.03, 0.499
**
** INTERACTION PROPERTIES
**
*Surface Interaction, name=IntProp-1
1.,

```

```

*Friction, slip tolerance=0.005
  0.1,
*Surface Behavior, pressure-overclosure=HARD
**
** BOUNDARY CONDITIONS
**
** Name: Axi Type: Symmetry/Antisymmetry/Encastre
*Boundary
_PickedSet8, YASYMM
** Name: Bottom Type: Symmetry/Antisymmetry/Encastre
*Boundary
_PickedSet7, ENCASTRE
**
** INTERACTIONS
**
** Interaction: Int-1
*Contact Pair, interaction=IntProp-1, type=SURFACE TO
SURFACE
Sample-1."Sample top", Cone-1."Cone surf"
** -----
-----
**
** STEP: Down
**
*Step, name=Down, nlgeom=YES, inc=1000
*Static
0.01, 1., 1e-05, 0.1
**
** BOUNDARY CONDITIONS
**
** Name: Down Type: Displacement/Rotation
*Boundary
_PickedSet39, 1, 1
_PickedSet39, 2, 2, -4.
_PickedSet39, 6, 6
**
** OUTPUT REQUESTS
**
*Restart, write, frequency=0
**
** FIELD OUTPUT: F-Output-1
**
*Output, field, variable=PRESELECT
**
** HISTORY OUTPUT: Contact1
**
*Output, history
*Contact Output
CAREA,
**

```

```

** HISTORY OUTPUT: Down
**
*Node Output, nset=Cone-1."Cone RP Set"
RF2, U2
*Node Print, nset=Cone-1."Cone RP Set", summary=no
RF2, U2
*Contact Print, summary=no
CAREA,
*End Step
** -----
-----
**
** STEP: Up
**
*Step, name=Up, nlgeom=YES, inc=1000
*Static
0.01, 1., 1e-05, 0.1
**
** BOUNDARY CONDITIONS
**
** Name: Axi Type: Symmetry/Antisymmetry/Encastre
*Boundary, op=NEW
_PickedSet8, YASYMM
** Name: Bottom Type: Symmetry/Antisymmetry/Encastre
*Boundary, op=NEW
_PickedSet7, ENCASTRE
** Name: Down Type: Displacement/Rotation
*Boundary, op=NEW
** Name: Up Type: Displacement/Rotation
*Boundary, op=NEW
_PickedSet40, 1, 1
_PickedSet40, 2, 2, 4.
_PickedSet40, 6, 6
**
** OUTPUT REQUESTS
**
*Restart, write, frequency=0
**
** FIELD OUTPUT: F-Output-1
**
*Output, field, variable=PRESELECT
**
** HISTORY OUTPUT: Contact1
**
*Output, history
*Contact Output
CAREA,
**
** HISTORY OUTPUT: Down
**

```

```
*Node Output, nset=Cone-1."Cone RP Set"  
RF2, U2  
*End Step
```

Sphere (Hyperelastic)

```
*Heading  
** Job name: Sphrefinalcf0 Model name: Sphere_new  
** Generated by: Abaqus/CAE 6.10-2  
*Preprint, echo=NO, model=NO, history=NO, contact=NO  
**  
** PARTS  
**  
*Part, name=Cone  
*End Part  
**  
*Part, name=Sample  
*End Part  
**  
**  
** ASSEMBLY  
**  
*Assembly, name=Assembly  
**  
*Instance, name=Cone-1, part=Cone  
0., -1500., 0.  
*Node  
1, -9.18485047e-16, 1500., 0.  
*Nset, nset=Cone-1-RefPt_, internal  
1,  
*Nset, nset="Cone RP Set"  
1,  
*Surface, type=SEGMENTS, name="Cone surf"  
START, 2.63692888321968, 1509.24812971375  
CIRCL, 0., 1500., 0.,  
1505.  
*Rigid Body, ref node=Cone-1-RefPt_, analytical  
surface="Cone surf"  
*End Instance  
**  
*Instance, name=Sample-1, part=Sample  
0., -3846.76281722965, 0.  
*Node  
1, 12., 3834.7627  
2, 12., 3846.7627  
3, 0., 3846.7627  
4, 0., 3834.7627  
5, 125., 3834.7627  
6, 125., 3846.7627
```

7,	12.,	3721.7627
8,	0.,	3721.7627
9,	125.,	3721.7627
10,	12.,	3834.88281
11,	12.,	3835.00293
12,	12.,	3835.1228
13,	12.,	3835.24292
14,	12.,	3835.36279
15,	12.,	3835.48291
16,	12.,	3835.60278
17,	12.,	3835.7229
18,	12.,	3835.84277
19,	12.,	3835.96289

More nodes, etc

```

*Nset, nset=_PickedSet39, internal, instance=Cone-1
1,
*Nset, nset=_PickedSet40, internal, instance=Cone-1
1,
*End Assembly
**
** MATERIALS
**
*Material, name=Sample
*Hyperelastic, ogden
0.0143, 7.3, 0.
**
** INTERACTION PROPERTIES
**
*Surface Interaction, name=IntProp-1
1.,
*Friction, slip tolerance=0.005
0.,
*Surface Behavior, pressure-overclosure=HARD
**
** BOUNDARY CONDITIONS
**
** Name: Axi Type: Symmetry/Antisymmetry/Encastre
*Boundary
_PickedSet8, YASYMM
** Name: Bottom Type: Symmetry/Antisymmetry/Encastre
*Boundary
_PickedSet7, ENCASTRE
**
** INTERACTIONS
**
** Interaction: Int-1
*Contact Pair, interaction=IntProp-1, type=SURFACE TO
SURFACE
Sample-1."Sample top", Cone-1."Cone surf"

```

```

** -----
-----
**
** STEP: Down
**
*Step, name=Down, nlgeom=YES, inc=1000
*Static
0.01, 1., 1e-05, 0.1
**
** BOUNDARY CONDITIONS
**
** Name: Down Type: Displacement/Rotation
*Boundary
_PickedSet39, 1, 1
_PickedSet39, 2, 2, -1.
_PickedSet39, 6, 6
**
** OUTPUT REQUESTS
**
*Restart, write, frequency=0
**
** FIELD OUTPUT: F-Output-1
**
*Output, field, variable=PRESELECT
**
** HISTORY OUTPUT: contact
**
*Output, history
*Contact Output
CAREA,
**
** HISTORY OUTPUT: Down
**
*Node Output, nset=Cone-1."Cone RP Set"
RF2, U2
*Node Print, nset = Cone-1."Cone RP Set", summary=no
RF2, U2
*Contact Print, summary=no
CAREA
*End Step

```

Appendix B: MATLAB Codes

Spherical (Elastic Plastic)

This code will find the values from the force-indentation curve

```
clear
hold on
file3 = 'zhao788elastic40.dat'%['SphereE'
num2str(ctrE),'s',num2str(ctrS),'n', num2str(ctrn),'.dat'];
fid=fopen(file3,'r'); % Opens .dat file for Reading
ctr = 1;
ctr2 = 1;
while ~feof(fid)
    tline=fgetl(fid);
    if isempty(strfind(tline,'N O D E   O U T P U T')) == 0 %Scan till
header
        for i=1:9
            tline=fgetl(fid); % Read 10 lines of junk lines
        end
        dataLine=fgetl(fid);%Grabs the reaction force and displacement
        data = sscanf(dataLine,'%i %f %f');
        P(ctr)=-data(2)/10^6;% extracts force data and converts to N
        del(ctr)=-data(3)/10^6;% extracts disp data and converts to m
        ctr = ctr+1;
    end
    if isempty(strfind(tline,'C O N T A C T   O U T P U T')) == 0 %Scan
till header
        for i=1:11
            tline=fgetl(fid); % Read 10 lines of junk lines
        end
        dataLine=fgetl(fid)%Grabs the contact stress
        if dataLine >0
            % data = sscanf(dataLine,'%i %s %f %f')
            data = sscanf(dataLine,'%f')
            CA(ctr2)=data(1)/(10^6)^2 % extracts contact area data and
converts to m^2
        end
        ctr2 = ctr2+1;
    end
end
fclose(fid);
R = 788;
del = del(find(del>=0))*10^6;
P = P(find(del>=0));
plot(del,P,'s')

max_del = max(del);
max_P = max(P);
ind_max_P = find(P==max_P);
ind_zero_P = find(P==0);
unload_P = P(ind_max_P:ind_zero_P(1));
unload_del = del(ind_max_P:ind_zero_P(1));
```

```

load_P = P(1:ind_max_P);
load_del = del(1:ind_max_P);
% figure
% plot(unload_del-unload_del(end),unload_P,'o')
S = [diff(unload_P)./diff(unload_del)]'
diff_del_13=abs((0.13*R-load_del))'
ind_del_13=find(diff_del_13==min(diff_del_13))
del_13=load_del(ind_del_13)
P_13 = load_P(ind_del_13)

s = fitoptions('Method','NonlinearLeastSquares',...
    'Lower',[0,0],...
    'Upper',[max_del,max_P],...
    'StartPoint',[1.1 31],...
    'TolX', eps)
form = ['B*d^m']
f = fittype(form, 'independent', 'd', 'coefficients', {'m','B'},
    'options',s);
fitobj = fit((unload_del-unload_del(end))', unload_P', f)
cf = coeffvalues(fitobj)
max_P
max_del
S_real = 1e6*cf(1)*cf(2)*(max_del-unload_del(end))^(cf(1)-1)
hold on
% plot(unload_del-unload_del(end),cf(2)*(unload_del-
unload_del(end)).^cf(1),'k')
%101.1,1003 103.1,1034
slope = (1034-1003)/(103.1-101.1);
P_13_int = slope*(102.44-101.1) +1003 % Interpolates between the points
to get at 0.13R

```

This code is for solving the Zhao algorithm

```

%Starting values

% %fine9
E_sigy = linspace(300,800,100);
n = .1:.005:.15
sigy_sig0 = linspace(.5,1.5,100);
sig0 = 400e6;

v = 0.3;

eR1 = 0.0374;
eR2 = 0.0674;

ER_sigy = E_sigy/(1-v^2);
R = 788e-6;
del1 = 0.13*R;
del2 = 0.3*R;
% Outputs from FE analysis or from experiment
P1 = 1.0238e+03 +0 ;

```

```

P2 = 2.2804e+03 +0 ;
S = 3.4932e+08 +0 ;

C1 = P1/del1^2;
C2 = P2/del2^2;

% make 1 if it is the first time running the program
% make it any number greater than 1 after that
run_num = 12

%Builds the reference stress matrix and saves to matrix.mat
if run_num==1
    sigR1 = ones(length(E_sigy),length(sigy_sig0),length(n));
    sigR2 = ones(length(E_sigy),length(sigy_sig0),length(n));
    Ep = ones(length(E_sigy),length(sigy_sig0),length(n));
    Sp = ones(length(E_sigy),length(sigy_sig0),length(n));
    np = ones(length(E_sigy),length(sigy_sig0),length(n));
    count =0;
    for ctrE = 1:length(E_sigy)
        for ctrS = 1:length(sigy_sig0)
            for ctrN = 1:length(n)

                nn =n(ctrN);
                sigy = sigy_sig0(ctrS)*sig0;
                E = E_sigy(ctrE)*sigy_sig0(ctrS)*sig0;
                options = optimset('TolFun',1e-12,'Display','off');
                sigR1(ctrE,ctrS,ctrN) = fsolve(@(x) (sigy*(E/sigy*
(x/E+ eR1) )^nn -x), sig0,options);
                sigR2(ctrE,ctrS,ctrN) = fsolve(@(x) (sigy*(E/sigy*
(x/E+ eR2) )^nn -x), sig0,options);
                Ep(ctrE,ctrS,ctrN) = ER_sigy(ctrE);
                Sp(ctrE,ctrS,ctrN) = sigy_sig0(ctrS);
                np(ctrE,ctrS,ctrN) = n(ctrN);
                count= count+1
            end
        end
    end
    save 'matrix_redo2'

else
    % loads the resfence stress matrix and continues the program
    % load 'matrix_fine4'
    % load 'matrix_coarse'
    load 'matrix_redo2'
end

check1 = sigR1(4,6,2) / (sigR1(4,6,2) +
E_sigy(4)*sigy_sig0(6)*sig0*eR1)^n(2)...
- sigR2(4,6,2) / (sigR2(4,6,2) +
E_sigy(4)*sigy_sig0(6)*sig0*eR2)^n(2)

```

```

% [Ep,Sp,np] = meshgrid(sigy_sig0,ER_sigy,n);

m1 = Ep.*Sp.*sig0./sigR1;
m2 = Ep.*Sp.*sig0./sigR2;

%Evaluate the fitting functions
A1 = 3.66556 + 0.0244179*np;
A2 = 6.06122-2.15891*np;
q = 29.0856 - 24.3547*np;
p = 1.31861-0.154675*np;
k1 = 1.001 +0.2610*np - 0.5217*np.^2 + 0.1547*np.^3;
k2 = 1.002 +0.7637*np - 1.9200*np.^2 + 1.255*np.^3;

j1 = 32.77 - 52.59*log(m1) + 33.46*(log(m1)).^2 -4.8*(log(m1)).^3 ...
    +0.2147*(log(m1)).^4;

j2 = 8.817 - 12.73*log(m1) + 11.99*(log(m1)).^2 -2.032*(log(m1)).^3 ...
    +0.1049*(log(m1)).^4;

g = A2 + (A1-A2)./(1+(m2./q).^p);
fp1 = k1.*j1;

fp2 = k2.*j2;

% Calculate Errors
e1 = C1./sigR1 - fp1;
e2 = C2./sigR2 - fp2;
e3 = S./(Ep.*Sp.*sig0.*del2) - g;
e = abs(e1) +abs(e2) + abs(e3);

%Find location of values
[r,c,u] = ind2sub(size(e),find(e == min(min(min(e))) ) );

%Output new values of E, sig_y, and n
new_E = Ep(r,c,u)*Sp(r,c,u)*sig0*(1-v^2)
new_n = np(r,c,u)
new_sigy = Sp(r,c,u)*sig0

min_e1 = min(abs(e1(:)))
min_e2 = min(abs(e2(:)))
min_e3 = min(abs(e3(:)))
min_e = min(abs(e(:)))
Pd = abs(round([(new_E-210e9)/210e9,(new_n-.127)/.127,(new_sigy-
400e6)/400e6]*100))

```

Spherical (Hyperlastic)

```
file = {'mu8sphere3.dat'; 'mu8sphere3-reverse.dat'}

for ctr_1 = 1:length(file)
    fid=fopen(file{ctr_1}, 'r'); % Opens .dat file for Reading

    ctr = 1;
    ctr2 = 1;
    ctr3 = 1;
    while ~feof(fid)
        tline=fgetl(fid);

        if isempty(strfind(tline, 'N O D E   O U T P U T')) == 0 %Scan
till header
            for i=1:9
                tline=fgetl(fid); % Read 10 lines of junk lines
            end
            dataLine=fgetl(fid); %Grabs the reaction force and
displacement
            data = sscanf(dataLine, '%i %f %f');
            F(ctr)=-data(2)/10^6; % extracts force data and converts to
N
            d(ctr)=-data(3)/10^6; % extracts disp data and converts to m
            ctr = ctr+1;
        end

        if isempty(strfind(tline, 'C O N T A C T   O U T P U T')) == 0
%Scan till header
            for i=1:11
                tline=fgetl(fid); % Read 10 lines of junk lines
            end
            dataLine=fgetl(fid); %Grabs the contact stress
            if dataLine >0
                % data = sscanf(dataLine, '%i %s %f %f')
                data = sscanf(dataLine, '%f');
                CA(ctr2)=data(1)/(10^6)^2; % extracts contact area data
and converts to m^2
            end
            ctr2 = ctr2+1;
        end

        if isempty(strfind(tline, 'E N E R G Y   O U T P U T')) == 0
%Scan till header
            for i=1:22
                tline=fgetl(fid); % Read 10 lines of junk lines
            end
            dataLine=fgetl(fid); %Grabs the contact stress
            if dataLine >0
                % data = sscanf(dataLine, '%i %s %f %f')
                data = sscanf(dataLine, '%s %s %s %s %s %f');
                E(ctr3)=data(end)/(10^6)^2; % extracts strain energy
data and converts to m^2
            end
        end
    end
end
```

```

        ctr3 = ctr3+1;
    end
end

matrix.F{ctr_1,:} = [0, F(find(d>=0))]; %N
matrix.d{ctr_1,:} = [0, d(find(d>=0))]; %m
matrix.CA{ctr_1,:} = [0, CA(find(d>=0))]; %m^2
matrix.E{ctr_1,:} = [0, E(find(d>=0))]; %
end
%%
% Force Displacement plot and analysis
R =120e-6;
h = linspace(0,0.4*R,100);
E = 3*7.97e3;
v = 0.499;
ER = E/(1-v^2);

alpha = 20;

ac = sqrt(R*h);
P = 4/3*ER*R^.5*h.^1.5;

plot(h,P,'--')
hold on
gr_str = ['r+';'kx'; 'ko';'bs';'mo'];
for ctr = 1:length(file)
    plot(matrix.d{ctr,:},matrix.F{ctr,:},gr_str(ctr,:))
end
grid on
xlabel('Displacement, h')
ylabel('Force, N')
grid on
legend('Analytic',file{1},'Location','Northwest')
% legend('\alpha = 97.1100 ', '\alpha = 61.9200 ', '\alpha = 59.2200
', 'Location','Northwest')
figurehandle =(gcf);
set(findall(figurehandle,'type','text'),'fontsize',14,'fontweight','bold')

% Fitting and plotting the stress strain curve

figure
hold on
for ctr = 1:length(file)
    Fs = matrix.F{ctr}
    CAs = matrix.CA{ctr}
    ds = matrix.d{ctr}

    matrix.strain{ctr,:} = [0, 0.2*sqrt(ds(2:end)./R) ];
    matrix.stress{ctr,:} = [0, Fs(2:end) ./ CAs(2:end)]

    plot(matrix.strain{ctr,:},matrix.stress{ctr,:},gr_str(ctr,:))

```

```

init = diff(matrix.stress{ctr,:}) ./ diff(matrix.strain{ctr,:})
initE = init(1)

s = fitoptions('Method','NonlinearLeastSquares',...
    'Robust','Bisquare',...
    'Lower',[0,0],...
    'Upper',[],...
    'StartPoint',[initE*40/3/pi/0.75,5],...
    'DiffMinChange',1e-8,...
    'DiffMaxChange',.1,...
    'MaxIter',1000,...
    'TolFun',eps,...
    'TolX',eps);

form = ['B/a*( -(1-x).^(a-1) + (1-x).^ (-a/2-1))'];

f = fittype(form, 'independent', 'x', 'coefficients', {'B','a'},
    'options',s);
[fitobj,gof] = fit(matrix.strain{ctr,:}', matrix.stress{ctr,:}',
f)
cf(ctr,:) = coeffvalues(fitobj);
plot(matrix.strain{ctr,:}, cf(ctr,1)/cf(ctr,2)*...
    ( - (1-matrix.strain{ctr,:}).^(cf(ctr,2)-1)...
    + (1-matrix.strain{ctr,:}).^(-cf(ctr,2)/2-1)), 'k' );
end
mu0_out_sig = cf(:,1)*3/40*pi*(1-v^2)
alpha_out_sig = cf(:,2)
hold on

plot(matrix.strain{1,:},matrix.strain{1,:}*ER*20/3/pi) %plots the
%linear elastic solution
grid on
xlabel('Strain')
ylabel('Stress, Pa')
grid on
legend('\mu_0 = 7.97kPa, \alpha = 20', 'Reverse Analysis', 'Linear
Elastic', 'Location', 'Northwest')
% legend('\alpha = 97.1100 ', '\alpha = 61.9200 ', '\alpha = 59.2200
', 'Location', 'Northwest')
figurehandle = gcf;
set(findall(figurehandle, 'type', 'text'), 'fontsize', 14, 'fontweight', 'bold')

```

Appendix C: Hawkmoth Rearing [21]

The AFIT Flapping wing MAV research group receives hawkmoth pupae on a regular basis from Dr. Mark Willis at Case Western University. Dr. Willis' lab contains a thriving colony of *Manduca Sexta*, which produces scores of moths each week. The most challenging part of raising the hawkmoths, hatching the eggs and feeding the caterpillars, is already complete when we receive the pupae in the mail. All they need are a proper light cycle and the right temperature in order to eclose (hatch into adulthood). Figure 63 shows a hawkmoth pupa. The specimen is on its back with the head pointed toward the left. The right forewing can be seen wrapped around midsection of the body. The abdomen with its many segments and spiracles, points to the right. The “handle” object protruding from the head is the proboscis, folded several times. When extended, the proboscis of the adult *M.sexata* can be as long as it's body, and is used for feeding on flower nectar while hovering.

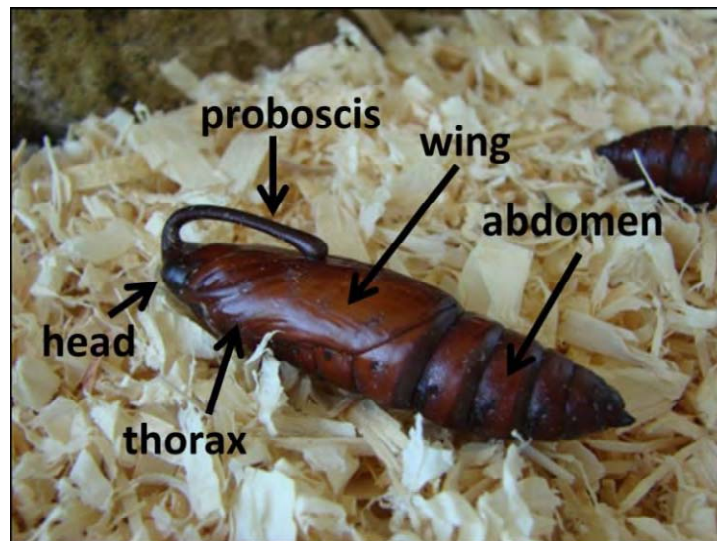


Figure 63: Typical *M. sexta* pupa and diagram of individual parts

A 1x1x1 foot cubic terrarium holds the pupae prior to eclosion. The bottom of the terrarium is lined with approximately 1 inch of wood shavings beneath a layer of paper towels. This, along with frequent cleaning, is necessary because with each moth's eclosion comes a release of large quantities of waste (*meconium*) which is the by-product of the transformation from caterpillar to moth (Reinecke, Buckner and Grugel 1980). The front of the terrarium has doors which can swing open for access from the front and the entire top glass pane can be removed for access from the top. The most important feature is the back wall made of textured foam. This wall gives the freshly eclosed moth a surface to climb up, which is an absolute necessity. The moth must climb off of the ground in order to pump fluids through the veins in its wings to stretch them out before they harden. Typically, the moth finds a position on the wall in about 10 minutes and has fully inflated its wings 20 minutes later. Figure 64 shows two young adult hawkmoths which hatched only a few minutes apart.

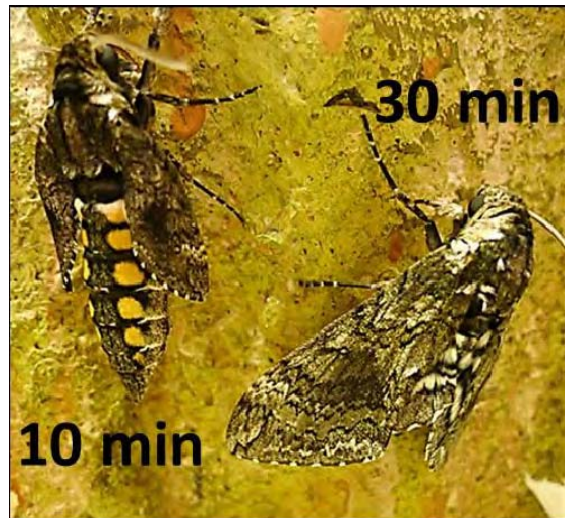


Figure 64: Two freshly-enclosed *M. Sexta* specimens. One is only 10 minutes old and has not inflated its wings.

M. sexta thrives in the warm temperatures of the southern North American summer. The pupae prefer a summertime light cycle of long days and short nights, as well as warm summertime temperatures. The light cycle for the AFIT moths has been set to 14 hours of light and 10 hours of darkness (Willis 2011). The light cycle is accomplished using a standard outlet timer wired to a string of LED lights secured around the inner walls of a cardboard box (Figure 65). The terrarium with the pupae is placed within this box and the lid is then closed, allowing no light from the outside. The temperature of the vivarium is set to 80 degrees Fahrenheit and the humidity is kept at 40 percent in order to replicate summertime conditions.



Figure 65: Enclosure for the pupae: (Left) Closed box creates day/night conditions with a timer controlling the LED lights, shown in part (Right)

The terrarium is checked daily for newly emerged adult moths. They tend to eclose at “dusk,” or shortly after their light cycle switches from light to dark. Since the cardboard box enclosure around the terrarium allows this light cycle to be set for any

time of day, the light-to-dark transition has been set to occur mid-afternoon. That way, the moths will eclose in the afternoon and the terrarium can be checked for adults when heading home for the day. When an adult moth is found in the pupa terrarium during daily inspections, it is transferred to a mesh cage which is constantly open to the light of the vivarium. *M.sexata* is a nocturnal species, and as such is inactive during daylight. The adults are therefore docile and essentially dormant as long as the lights are kept on. If the lights are switched off, however, the adults will fly for hours against the walls of the enclosure and damage their wings. This is to be avoided because much of the research that goes on among the AFIT FWMAV research group requires intact forewings.

Bibliography

1. Petricca, L. P. Ohlckers, and C. Grinde. "Micro- and Nano-Air Vehicles: State of the Art," *International Journal of Aerospace Engineering*, vol. 2011: 1-17, (2011).
2. Demasi, L., A. N. Palazotto, A. Hollenbeck, and R. Cavallaro. "Exploratory Structural Investigation of a Hawkmoth-Inspired MAV's Thorax," *International Journal of Micro Air Vehicles*, 4(4): 291-304 (December 2012).
3. Oliver, V. C. and G.M. Phar. "An Improved Technique for Determining Hardness and Elastic Modulus Using Load and Displacement Sensing Indentation", *Journal of Materials Research*, 7: 1564-1583 (1992).
4. Chen, X. "Computational Modeling of Indentation," in *Handbook of Nanoindentation with Biological Applications*. Ed. Michelle L. Oyen. Pan Stanford Publishing Pte. Ltd., Singapore, 2011.
5. Zhao, M., N. Ogasawara, N. Chiba, and X. Chen, "A new approach to measure the elastic-plastic properties of bulk materials using spherical indentation," *Acta Materialia*, Volume 54, Issue 1, Pages 23-32 (January 2006)
6. Fung, Y.C. *Biomechanics: Mechanical Properties of Living Tissues (2nd ed.)*. Springer-Verlag, New York, NY, 1993.
7. Moss, R.L. and W. Halpern. "Elastic and Viscous properties of Resting Frog Skeletal Muscle," *Biophysical Journal*, 17(3): 213-228 (March 1977).
8. Van Loocke, M. C.G. Lyons, and C.K. Simms. "A Validated Model of Passive Muscle in Compression," *Journal of Biomechanics*, 39(16): 2999-3009 (2006).
9. Lally, C., A.J. Reid, and P.J. Prendergast. "Elastic Behavior of Porcine Coronary Artery Tissue Under Uniaxial and Equibiaxial Tension," *Annals of Biomedical Engineering*, 32(10): 1355-1364 (October 2004).
10. Shean, T.A.V., M.L. Oyen, and M.F. Ashby. "Introduction," in *Handbook of Nanoindentation with Biological Applications*. Ed. Michelle L. Oyen. Pan Stanford Publishing Pte. Ltd., Singapore, 2011.
11. Ebenstein, D. M. "Nanoindentation of Soft Materials and Bio Materials," in *Handbook of Nanoindentation with Biological Applications*. Ed. Michelle L. Oyen. Pan Stanford Publishing Pte. Ltd., Singapore, 2011.

12. Lin, D.C., D.I. Shreiber, E.K. Dimitriadis, and F. Horkay. "Spherical Indentation of Soft Matter Beyond the Hertzian Regime: Numerical and Experimental Validation of Hyperelastic Models," *Biomechanics and Modeling in Mechanobiology*, 8(5): 345-358 (November 2008).
13. Nayer, V.T. , J.D. Weiland, and A.M. Hodge, "Characterization of porcine sclera using instrumented Nanoindentation," *Materials Science and Engineering C*, 796-800 (February 2011)
14. Zhu, J., T. Sabharwal, A. Kalyanasundaram, L. Guo, and G. Wang, "Topographic Mapping and Compression Elasticity Analysis of Skinned Cardiac Muscle Fibers in Vitro with Atomic Force Microscopy and Nanoindentation," *J Biomech.* 42(13): 2143–2150 (2009 September)
15. Erdemir, A., M.L. Viveiros, and P.R. Cavanagh. "Numerical-experimental Approach for Characterizing Subject Specific Hyperelastic Properties of the Heel Pad." *Proceedings of the American Society of Mechanical Engineers Summer Bioengineering Conference. Key Biscayne, FL.* 2003.
16. Gras, L., D. Mitton, P. Viot, and S. Laporte. "Hyper-elastic properties of the human sternocleidomastoideus muscle in tension," *Journal of the Mechanical Behavior of Biomedical Materials*, 15: 131-140 (June 2012)
17. Calvo, B., A. Ramirez, A. Alonso, J. Grasa, F. Soteras, R. Osta, and M.J. Muñoz. "Passive Nonlinear Elastic Behaviour of Skeletal Muscle: Experimental Results and Model Formulation," *Journal of Biomechanics*, 43(2): 318-325 (October 25, 2009).
18. Dorfmann, A., Trimmer, B.A, and Woods Jr, W.A. "A constitutive model for muscle properties in a soft-bodied arthropod," *J. R. Soc. Interface*: 257–269 (April 2007)
19. Eaton, J. L. *Lepidopteran anatomy*. Wiley-Interscience, New York, NY, 1988.
20. O'Hara, R. P. *The characterization of material properties and structural dynamics of the Manduca Sexta forewing for application to flapping wing micro air vehicle design*. Ph.D. Dissertation, AFIT/DS/ENY/12-06, Graduate School of Engineering and Management, Air Force Institute of Technology, September 2012.
21. Hollenbeck, A.C. *Evaluation of the thorax of Manduca Sexta for flapping wing micro air vehicle applications*. M.S. Thesis, AFIT/GAE/ENY/12-M22,

- Department of the Aeronautics and Astronautics, Air Force Institute of Technology, March 2012.
22. Cranston, B.C. *Evaluation of the thorax of the Manduca Sexta for flapping wing micro air vehicle applications* M.S. Thesis, AFIT/GAE/ENY/12-D03, Department of the Aeronautics and Astronautics, Air Force Institute of Technology, December 2012 thesis
 23. Tubbs, T.B. *Biological investigation of the stimulated flapping motions of the moth, Manduca Sexta*. M.S. Thesis, AFIT/GSS/ENY/11-M04, Department of Aeronautics and Astronautics, Air Force Institute of Technology, March 2011.
 24. Chou, C. and B. Hannaford. "Measurement and Modeling of McKibben Pneumatic Artificial Muscles," *IEEE Transactions on Robotics and Automation*, 12(1): 90-102 (February 1996).
 25. Bar-Cohen, Y. "Biologically Inspired Intelligent Robots Using Artificial Muscles," *Strain*, 41(1): 19-24 (February 2005).
 26. Bar-Cohen, Y. and C. L. Breazeal. *Biologically Inspired Intelligent Robots*. SPIE Press, Bellingham, WA, 2003.
 27. Lima, M. D., N. Li, M.J. DeAndrade, S. Fang, J. Oh, G.M. Spinks, M.E. Kozlov, C.S. Haines, D. Suh, J. Foroughi, S.J. Kim, Y., Chen, T. Ware, M.K. Shin, L.D. Machado, A.F. Fonseca, J.D.W. Madden, W.E. Voit, D.S. Galvao, and R.H. Baughman. "Electrically, Chemically, and Photonically Powered Torsional and Tensile Actuation of Hybrid Carbon Nanotube Yarn Muscles," *Science magazine*, 338(6109): 928-932 (16 November 2012).
 28. Du, G., E. Moulin, N. Jouault, E. Buhler, and N. Giuseppone. "Muscle-like Supramolecular Polymers: Integrated Motion from Thousands of Molecular Machines," *Angewandte Chemie International Ed.*, 51: 12504–12508 (2012).
 29. Fischer-Cripps, A.C. *Introduction to Contact Mechanics*. Springer-Verlag, New York, NY, 2000.
 30. Cao, Y., X. Qian, and N. Huber, "Spherical indentation into elastoplastic materials: Indentation-response based definitions of the representative strain," *Materials Science and Engineering A*, 454–455 (April 2007)
 31. Ramesh, K.T. *Nanomaterials Mechanics and Mechanisms*. Springer, New York, NY, 2009.
 32. ABAQUS Analysis User's Manual v6.10 user handbook

33. Ng, B.H., S.M. Chou, and V. Krishna. "The Influence of Gripping Techniques on the Tensile Properties of Tendons," *Proceeding of the Institution of Mechanical Engineers. Part H, Journal of Engineering in Medicine*, 219(5), 349-354 (September 2005).
34. Aditad Vasinonta, Jack L. Beuth, 'Measurement of interfacial toughness in thermal barrier coating systems by indentation', *Engineering Fracture Mechanics*, 68, 843-860 (2001)
35. Shacham, S., D. Castel, and A. Gefen. "Measurements of the Static Friction Coefficient between Bone and Muscle Tissues," *Journal of Biomechanical Engineering*, 132(8): 084502 (August 2010).
36. Cox, M.A.J., N.J.B. Driessen, R.A. Boerboom, C.V.C. Bouten, and F.P.T. Baaijens. "Mechanical Characterization of Anisotropic Planar Biological Soft Tissues Using Finite Indentation: Experimental Feasibility," *Journal of Biomechanical Engineering*, 41(2): 422-429 (2008).
37. Collinsworth, A.M., S. Zhang, W.E. Kraus, and G.A. Truskey. "Apparent Elastic Modulus and Hysteresis of Skeletal Muscle Cells throughout Differentiation," *American Journal of Physiology. Cell Physiology*, 283(4): 1219-1227.

REPORT DOCUMENTATION PAGE				<i>Form Approved OMB No. 074-0188</i>	
<p>The public reporting burden for this collection of information is estimated to average 1 hour per response, including the time for reviewing instructions, searching existing data sources, gathering and maintaining the data needed, and completing and reviewing the collection of information. Send comments regarding this burden estimate or any other aspect of the collection of information, including suggestions for reducing this burden to Department of Defense, Washington Headquarters Services, Directorate for Information Operations and Reports (0704-0188), 1215 Jefferson Davis Highway, Suite 1204, Arlington, VA 22202-4302. Respondents should be aware that notwithstanding any other provision of law, no person shall be subject to a penalty for failing to comply with a collection of information if it does not display a currently valid OMB control number.</p> <p>PLEASE DO NOT RETURN YOUR FORM TO THE ABOVE ADDRESS.</p>					
1. REPORT DATE (DD-MM-YYYY) 21-03-2013		2. REPORT TYPE Master's Thesis		3. DATES COVERED (From - To) August 2011 - March 2013	
TITLE AND SUBTITLE Application Of Finite Element To Evaluate Material With Small Modulus Of Elasticity				5a. CONTRACT NUMBER	
				5b. GRANT NUMBER	
				5c. PROGRAM ELEMENT NUMBER	
6. AUTHOR(S) Dauby, Boyce H., Captain, USAF				5d. PROJECT NUMBER	
				5e. TASK NUMBER	
				5f. WORK UNIT NUMBER	
7. PERFORMING ORGANIZATION NAMES(S) AND ADDRESS(S) Air Force Institute of Technology Graduate School of Engineering and Management (AFIT/ENY) 2950 Hobson Way, Building 640 WPAFB OH 45433-8865				8. PERFORMING ORGANIZATION REPORT NUMBER AFIT-ENY-13-M-08	
9. SPONSORING/MONITORING AGENCY NAME(S) AND ADDRESS(ES) Attn: Dr. Douglas Smith AFOSR/RSA (703) 696-6219 DSN (426-6219 Fax (503) 696-7320 E-mail: douglas.smith@aforsr.af.mil Air Force Office of Scientific Research 875 North Randolph Street Arlington, VA., 22203-1768				10. SPONSOR/MONITOR'S ACRONYM(S) AFOSR	
				11. SPONSOR/MONITOR'S REPORT NUMBER(S)	
12. DISTRIBUTION/AVAILABILITY STATEMENT APPROVED FOR PUBLIC RELEASE; DISTRIBUTION UNLIMITED.					
13. SUPPLEMENTARY NOTES This material is declared a work of the U.S. Government and is not subject to copyright protection in the United States.					
14. ABSTRACT This thesis describes the development of a series of models utilizing the commercial finite element suite ABAQUS specifically to apply towards the study of biological tissue. The end goal is to be able to obtain the material properties of the Manduca Sexta, a biological inspiration for flapping wing micro-air vehicles. Two finite element models were used to analyze the results of two prior studies of other researchers. A flat punch elastic model examined boundary effects and confirmed that the point of indentation was far enough removed from the boundary. The hyperelastic spherical indentation experiment examined the effects of coefficient of friction on the indentation. Another algorithm was reproduced to analyze the elastic, power law-hardening properties of a wide range of material properties. A nanoindentation system was used to investigate the modulus of the M. Sexta. Due to instrument limitations, useful data was not able to be collected. An upper bound on the modulus was established on the order of 1 MPa. A uniaxial tension test of the M.Sexta was used to obtain a reported initial modulus of elasticity values of 343 kPa.					
15. SUBJECT TERMS Manduca sexta, M.sexta, Nanoindentation, tension test, muscle properties					
16. SECURITY CLASSIFICATION OF:			17. LIMITATION OF ABSTRACT UU	18. NUMBER OF PAGES 127	19a. NAME OF RESPONSIBLE PERSON Dr. Anthony Palazotto, Professor, AFIT, (ENY)
a. REPORT U	b. ABSTRACT U	c. THIS PAGE U			19b. TELEPHONE NUMBER (Include area code) (937) 255-6565, ext 4599 anthony.palazotto@afit.edu